論文 / 著書情報
Article / Book Information

題目(和文)	有機材料中における三重項励起子拡散のナノスケール特性評価
Title(English)	Nanoscale study of triplet exciton diffusion in organic molecular materials
著者(和文)	成島魁至
Author(English)	Kaishi Narushima
出典(和文)	学位:博士(工学), 学位授与機関:東京工業大学, 報告番号:甲第11145号, 授与年月日:2019年3月26日, 学位の種別:課程博士, 審査員:VACHA　MARTIN,森 健彦,大内 幸雄,松本 英俊,早水 裕平
Citation(English)	Degree:Doctor (Engineering), Conferring organization: Tokyo Institute of Technology, Report number:甲第11145号, Conferred date:2019/3/26, Degree Type:Course doctor, Examiner:,,,,
学位種別(和文)	博士論文
Type(English)	Doctoral Thesis

Nanoscale study of triplet exciton diffusion in organic molecular materials

有機材料中における三重項励起子拡散のナノスケール特性評価

Kaishi Narushima

School of Materials and Chemical Technology

Tokyo Institute of Technology

Contents

Chapter 1: General Introduction 1
1-1 Introduction 1
1-1-1 Singlet excited state and triplet excited state 1
1-1-2 Energy transfer 4
1-2 Triplet exciton diffusion 7
1-2-1 The role of triplet exciton diffusion in organic materials 8
1-2-2 Methods for measuring triplet exciton diffusion length 10
1-3 Aim and outline 18
Chapter 2: Triplet Exciton Diffusion in Up-conversion Materials 24
2-1 Introduction 24
2-1-1 Up-conversion materials 24
2-1-2 Principle of triplet-triplet annihilation based UC materials 25
2-1-2 Solid-state UC materials 27
2-1-3 Current issues in organic solid-state UC materials and purpose of this study 28
2-2 Experimental 29
2-2-1 Concept of the method for estimating Lt using an optical microscope 29
2-2-2 Experimental method 31
2-3 Result and discussion 34
2-3-1 Photophysical characterization of the prepared samples 34
2-3-2 Triplet exciton diffusion in polycrystalline AC film 36
2-3-3 Triplet exciton diffusion in polycrystalline DPA film 40
2-3-3 Comparing the value of L_t measured by proposed method with that measured by a conventional indirect method 44
2-4 Summary 49
Chapter 2 Appendix 51
Chapter 2 References 55
Chapter 3: Triplet Exciton Diffusion in Conjugated Polymer Nanofibers 57
3-1 Introduction 57
3-1-1 Exciton diffusion in conjugated polymers 57
3-1-2 Fabrication of conjugated polymer nanofibers 59
3-1-3 Purpose 61
3-2 Experimental 61
3-2-1 Method for measurement L_t and sample selection 61
3-2-2 Sample preparation 62

3-3 Result and discussion.....64
3-4 Summary.....73
Chapter 3 References.....74
Chapter 4: Suppressed Triplet Exciton Diffusion as a Possible Factor for the Appearance of Persistent Room Temperature Phosphorescence.....76
4-1 Introduction.....76
4-1-1 Persistent room temperature phosphorescence.....76
4-1-2 Current issues.....77
4-1-3 Purpose.....79
4-2 Experimental.....79
4-2-1 Sample preparation.....79
4-2-2 Measurement methods.....80
4-3 Result and discussion.....81
4-3-1 Estimation of the value of k_{nr} and k_q.....82
4-3-2 Measurement of triplet exciton diffusion.....84
4-4 Summary.....98
Chapter 4 Appendix.....100
Chapter 4 References.....110
Chapter 5: Conclusion and Outlook.....**113**
5-1 General conclusion.....113
5-2 Outlook.....115
List of Publications.....117
Public appearances.....118
Achievements.....119
Acknowledgements.....120

Chapter 1: General Introduction

1-1 Introduction

The study of organic photochemistry has brought us a lot of benefits for several decades. Comparing with inorganic materials, there are a lot of advantages of organic materials such as flexibility, low-cost and harmlessness. Therefore, the study and development of organic photochemistry can lead discovery of novel phenomena and to creation of next-generation devices. For example, organic light-emitting diodes (OLEDs) are one of the results of the development of organic photochemistry, and OLEDs are being commercialized as displays now. In order to develop such organic material devices, deep photochemical and photophysical understanding is crucial. Generally, organic photochemistry can be considered as the study of excited states in organic materials since the interaction between photons and organic molecules results in generation of excited state. In the following sections, the basis of organic photochemistry is explained.

1-1-1 Singlet excited state and triplet excited state

When photophysical or photochemical properties of organic molecular materials are discussed, two kinds of excited states have to be considered.[1] Both singlet and triplet excited state play important roles in the organic molecular materials and their function.

Before considering the excited states, the concept of spin which is important for understanding the singlet or triplet excited states is explained as follows. Spin is an intrinsic angular momentum of electrons (or protons and other nuclei) and is determined by two kinds of spin quantum numbers, s and m_s. In the case of electrons, the value of s is 1/2 and its projection along a prescribed axis (z axis) m_s is +1/2 or -1/2. This leads to

the value of momentum along the prescribed z axis of $+\hbar/2$ or $-\hbar/2$. However, the angular momenta along the orthogonal directions (x axis or y axis) are no longer determined in this situation. Therefore, a schematic illustration of an angular momentum vector of an electron is sometimes expressed using a cone whose angle between z axis is θ, as shown in Fig. 1-1a. Generally, the wavefunction of an electron with $m_s = +1/2$ can be described as α while the other one with $m_s = -1/2$ is expressed as β. When the interaction of two electrons is considered, the total spin (S) can be 1 (the wavefunctions of the spins are both α or both β), or 0 (each wavefunction is different, namely one is α and the other is β). In the case of $S = 0$, the component of S along z axis (M_s) is also 0. On the other hand, if S is 1, the component of S along z axis M_s can be -1, 0 or +1. In general, the electronic state whose total spin $S = 0$ is called singlet state while the electronic state whose total spin $S = 1$ is called triplet state. Now, the vectorial representations of singlet state and triplet state are described in Fig. 1-1a. The magnitudes of S and M_s can be visualized using the two cones. As shown in Fig. 1-1a, two vectors are antiparallel in singlet state while they are parallel in triplet state.

In the ground state of organic molecules, the two electrons are in the highest occupied molecular orbital (HOMO) and their two spins are antiparallel due to Pauli exclusion principle, which means that the ground state is singlet state. However, in the case of excited state, the two electrons are in different molecular orbitals. Therefore, the two electrons can be either antiparallel (singlet excited state), or parallel (triplet excited state). When optical transition from HOMO to lowest unoccupied molecular orbital (LUMO) is considered, the simplest schematic illustration of singlet or triplet excited states is used as shown in Fig. 1-1b.

Singlet excited state is an optically allowed transition since the total spin number of the

ground state is also 0 (ground state is also singlet state). On the other hand, triplet excited state is optically forbidden transition due to the difference in the spin multiplicity between ground state (singlet state) and triplet excited state. Although direct optical transition to triplet excited state is forbidden, mixing of the wavefunctions of the singlet excited state and triplet excited state can lead to the population of triplet excited state after photoexcitation into a singlet excited state. Such a nonradiative path from singlet excited state to triplet excited state is called intersystem crossing (ISC). In order to obtain efficient ISC, heavy-atom effect,[2,3] EL-Sayed rule[4] and symmetry rules[5] are used. After population of the triplet state, generally, triplet lifetime (τ_t) is much longer than singlet lifetime due to the forbidden nature of the transition.

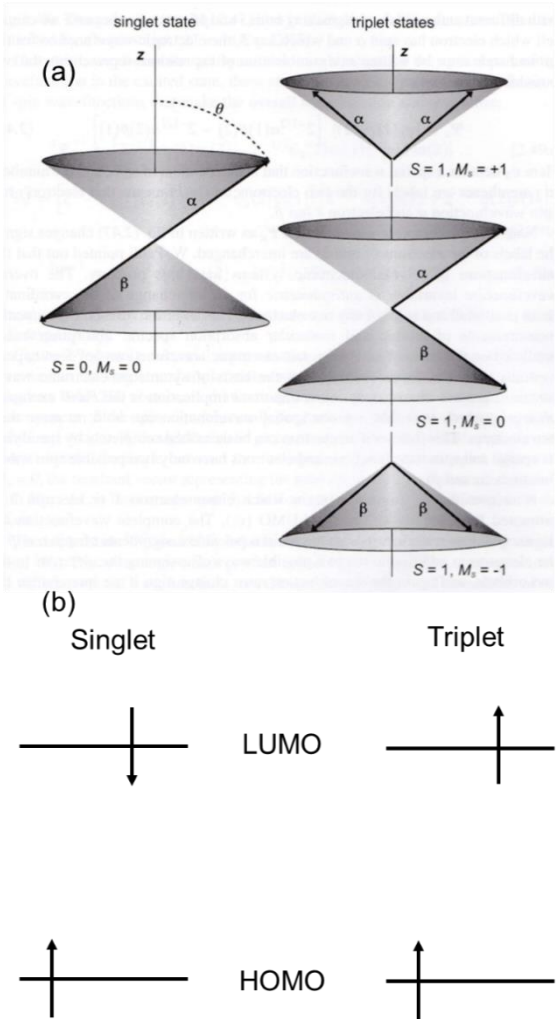

Figure 1-1. (a) Vectorial representation of electron spins. Reprinted from ref. [6]. (b) Illustration of singlet excited state (left) and triplet excited state (right).

1-1-2 Energy transfer

Excited molecules can interact with other molecules during their lifetime by the process of energy transfer. In organic photochemistry, two kinds of interactions, dipole-dipole interaction and exchange coupling, are important as driving forces of energy transfer.[6-9]

In the case of energy transfer via dipole-dipole interaction, transition dipole of acceptor molecules interacts with that of donor molecules resulting in excitation of acceptor molecules and deactivation of a donor molecules (Fig. 1-2a).[1] On the other hand, energy

transfer via exchange coupling can be consider as double charge transfer (simultaneous electron transfer and hole transfer) (Fig. 1-2b).[1,10]

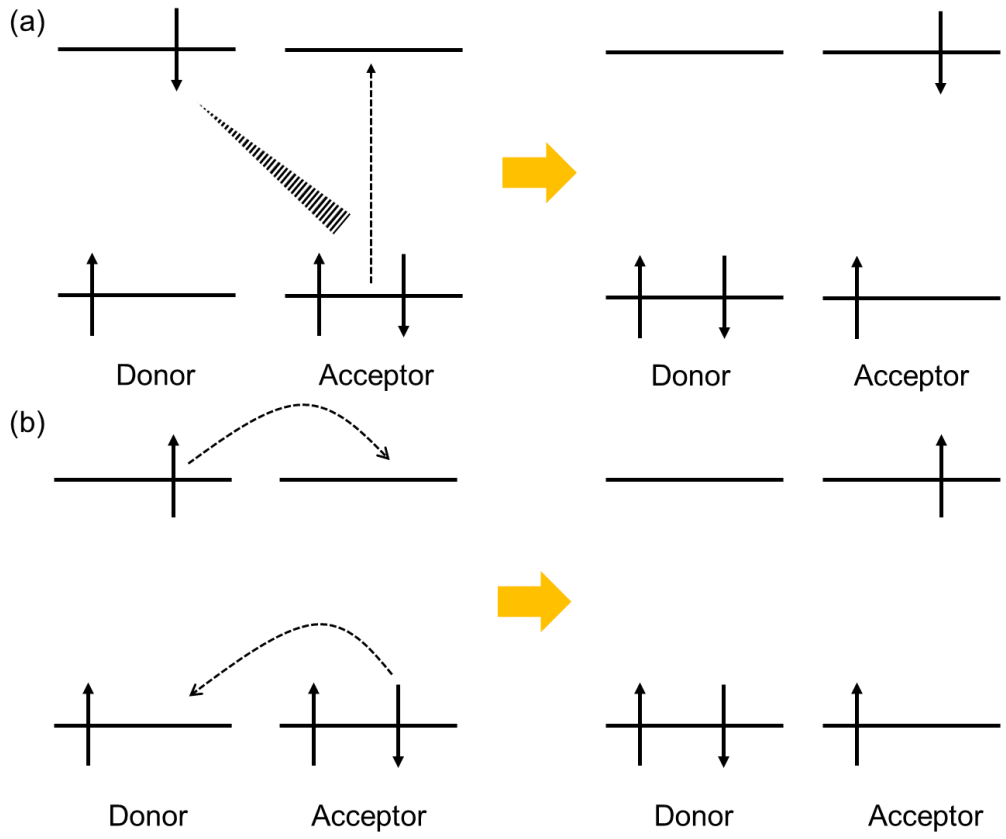

Figure 1-2. (a) Schematic illustration of energy transfer based on (a) dipole-dipole interaction and (b) exchange coupling.

For energy transfer based on dipole-dipole interaction, energy transfer rate (k_{fret}) is expressed as

$$k_{\mathrm{fret}} = \frac{\kappa^2}{r^6}\int_0^\infty |\mu_{\mathrm{d}}|^2\delta(\omega_{\mathrm{d}}-\omega)\,|\mu_{\mathrm{a}}|^2\delta(\omega_{\mathrm{a}}-\omega)\mathrm{d}\omega$$

$$= \frac{\kappa^2\Phi_{\mathrm{d}}}{r^6\tau_{\mathrm{d}}}\int_0^\infty \varepsilon_{\mathrm{a}}(\omega)\overline{F_{\mathrm{d}}}(\omega)\,\mathrm{d}\omega \qquad (1\text{-}1)$$

where r is the distance between donor molecule and acceptor molecule, κ is the

orientation factor, ω is the frequency, ω_{d} and ω_{a} are the transition frequencies of donor molecules and acceptor molecules, respectively and μ_{d} and μ_{a} are the transition dipole moments of donor molecules and acceptor molecules, respectively, Φ_{d} is the quantum efficiency of donor molecules, τ_{d} is the lifetime of donor molecules, $\varepsilon_{\mathrm{a}}(\omega)$ is the molar extinction coefficient of acceptor molecules and $\overline{F_{\mathrm{d}}}(\omega)$ is the normalized emission spectrum of donor molecules.[7] As shown in equation (1-1), k_{fret} becomes large when Φ_{d} and $\varepsilon_{\mathrm{a}}(\omega)$ are very large values. This means singlet-singlet energy transfer is likely to occur via dipole-dipole interaction because singlet excited state has potentially large Φ_{d} and $\varepsilon_{\mathrm{a}}(\omega)$ (large μ_{d} and μ_{a}) due to the allowed nature of optical transition. On the other hand, triplet-triplet energy transfer seldom occurs via this mechanism since triplet excited state is optically forbidden transition resulting in very small Φ_{d} and $\varepsilon_{\mathrm{a}}(\omega)$ (very small μ_{d} and μ_{a}). Energy transfer based on dipole-dipole interaction is called Förster resonant energy transfer (Fret).

Another mechanism of energy transfer that should be consider is exchange coupling. In the case of exchange coupling, energy transfer rate constant k_{dexter} can be expressed as

$$k_{\mathrm{dexter}} = \frac{2\pi}{\hbar}\exp\left(\frac{-2r}{R}\right)\int_0^{\infty}\overline{\varepsilon_{\mathrm{a}}}(\omega)\overline{F_{\mathrm{d}}}(\omega)\mathrm{d}\omega \qquad (1\text{-}2)$$

where $\hbar$ is Planck's constant, R is the average Bohr radius for the excited state of donor molecules and the ground state of acceptor molecules and $\overline{\varepsilon_{\mathrm{a}}}(\omega)$ is normalized absorption spectrum of acceptor molecules.[7] As shown in equation (1-2), exchange coupling is independent on transition dipole moment, which means triplet-triplet energy transfer can occur via this mechanism. It is notable that triplet excited state of aromatic molecules (acceptor molecules) that show insufficient ISC can be generated by using triplet sensitizer (donor molecules).[11] Since the transfer rate k_{dexter} can be approximated as exponential function of the distance between the two molecules as shown in equation

(1-2), the exchange coupling has much stronger dependence on the distance between donor and acceptor molecules compared with dipole-dipole interaction. When the distance between donor and acceptor molecules is longer than 1 nm, the value of k_{dexter} is generally very small and energy transfer based on exchange coupling hardly occurs.[1] Therefore, compared with Fret, the contribution of exchange coupling to singlet-singlet energy transfer is smaller due to its effectivity at short distances only, even though singlet-singlet energy transfer can in principle occur via exchange coupling. Energy transfer based on exchange coupling is called Dexter-type energy transfer.

1-2 Triplet exciton diffusion

Now considering energy transfer between donor and acceptor molecules in solution, the molecules diffuse via Brownian motion and encounter each other. The encounter is followed by the energy transfer interaction between the donor and acceptor molecules (Fig. 1-3). Consequently, this process is considered diffusion limited.[12] Hence, energy transfer in solution is dependent on viscosity of the solution, concentration of donor and acceptor molecules and concentration of oxygen that causes quenching of the excited molecules.

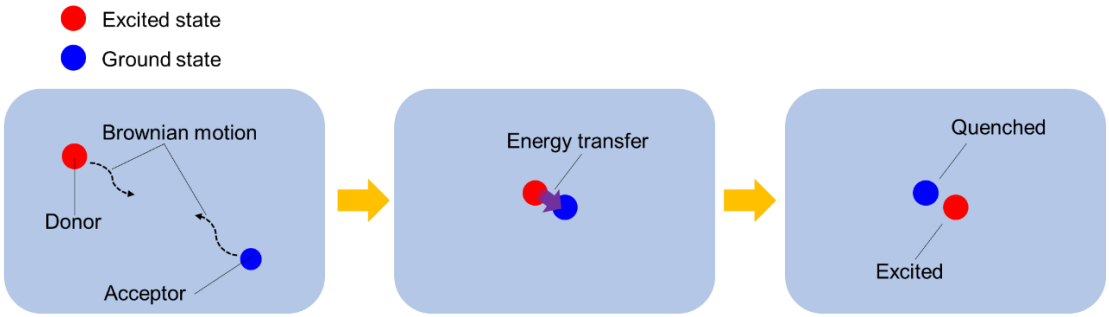

Figure 1-3. Energy transfer in solution. Excited energy of donor molecule is transferred after diffusion via Brownian motion.

On the other hand, in solid state such as host-guest materials or crystalline materials, a molecule itself no longer diffuses via Brownian motion due to the induced rigidity of solid state. However, excited energy can be transported to a neighboring site via energy transfer when energies of the acceptor and of the donor are close enough (Fig. 1-4).[11,13] Therefore, excited energy can be diffusing in solid state although molecules itself cannot diffuse. In addition, in solid state the excited energy can be delocalized over several molecules leading to the generation of Frenkel excitons.[6,7] Hence, excited energy transport in solid state is often called exciton diffusion. Singlet exciton diffusion and triplet exciton diffusion play important roles in solid state organic materials.[13]

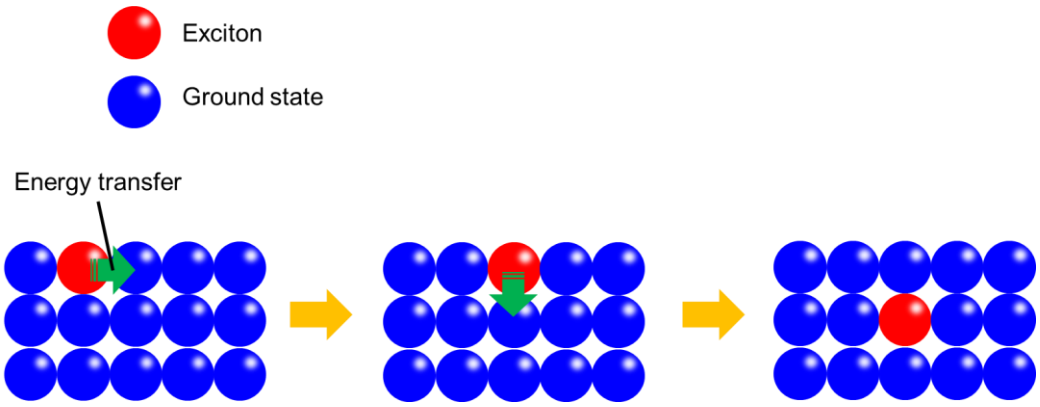

Figure 1-4. Energy transfer in solid-state materials. Excited energy is transferred via exciton diffusion.

1-2-1 The role of triplet exciton diffusion in organic materials

Exciton diffusion length (L) is one of the important factors that determine the characteristics of devices. L is can be expressed as follow

$$L = \sqrt{D\tau} \qquad (1\text{-}3)$$

where D is diffusion coefficient and τ is lifetime.[13]

In the case of singlet exciton, the exciton diffuses via energy transfer based on dipole-dipole interaction (Fret), which means singlet exciton diffusion coefficient (and k_{fret}) is

directly related to the transition dipole moment. On the other hand, singlet exciton lifetime is inversely proportional to transition dipole moment, and large transition dipole moment leads to large radiative rate (small singlet lifetime). Considering that the diffusion length is a product of the singlet exciton diffusion coefficient and singlet lifetime as shown in equation (1-3), the value of singlet exciton diffusion length is inherently limited. Yost *et al*. reported theoretically a maximum value of singlet exciton diffusion length in tetracene of about 100 nm.[14] Hence, singlet exciton diffusion length exceeding hundreds of nanometers is often considered difficult to achieve.[13,15-17]

On the other hand, in the case of triplet exciton, the exciton diffuses based on exchange coupling (Dexter type energy transfer). This means triplet exciton diffusion coefficient (D_t) is independent of transition dipole moment while τ_t still depends on the transition dipole moment. In general, transition dipole moment related to a transition from triplet excited state to ground state is very small due to the forbidden nature of the transition, leading to longer τ_t compared with singlet exciton. Therefore, unlike singlet exciton diffusion, triplet exciton diffusion length (L_t) is not limited by the opposing trends of diffusion coefficient and lifetime, which means both long or short L_t can be tuned by optimizing design parameters in organic materials.

Controlling triplet exciton diffusion is often necessary to extract the maximum performance in organic materials. For example, long L_t is preferred for organic solar cells[15,17,18] or triplet-triplet annihilation (TTA) based up-conversion (UC) materials[12,19] while short L_t is preferred for the appearance of ultralong-lived (persistent) room temperature phosphorescence (RTP) in aromatic crystals or thermally activated delayed fluorescence (TADF)-based electroluminescence materials.

1-2-2 Methods for measuring triplet exciton diffusion length

There is abundance of literature reporting triplet diffusion length L_t in various organic molecular materials.[18-33] These works were summarized in a review by Mikhnenko *et al.* In Table 1-1 (taken from the review), the values of L_t are presented.[13]

Material[a]	1D L_D (nm)	D (cm^2 s^{-1})
$(C_{12}OCH_8)_8PcZn$	23	9×10^{-8}
$(C_{18}OCH_2)PcH_2$	64	1.6×10^{-5}
1,4-Dibromonaphtalane	8400	3.5×10^{-4}
4P-NPD	11–54	
Alq3	14–140	$(0.8–7.2) \times 10^{-7}$
Anthracene	610 and 7000–20000	$(0.5–2) \times 10^{-4}$
C_{60}	28–35	
CBP	8.3–300	$(1.4–770) \times 10^{-8}$
F8-F6	50	7.9×10^{-6}
F8-PDA	41	4.7×10^{-6}
$Ir(ppy)_3$-cored dendrimers	2–10	$(8–400) \times 10^{-9}$
mCP	16	
Naphthalene	35 000	3.3×10^{-5}
NPD	6–87	
P(CM-Ru_x)	36	$(1–200) \times 10^{-7}$
PCBM	21	4.2×10^{-6}
PdTPPC	30	8×10^{-7}
Pentacene	40–800	$(1–4) \times 10^{-3}$
PF		3×10^{-4}
$Ph_{95}BTD_5$	22	4.7×10^{-6}
PhLPPP	1700–3900	$(0.5–14) \times 10^{-6}$
Pt acetylide oligomers		1.8×10^{-4}
PtOEP	13–30	
Pyrene	1200	1.3×10^{-4}
Rubrene	1000–4000	
Stilbene	11000	9×10^{-5}
Super Yellow PPV	10	
Tetracene	100–400	$(0.1–1.6) \times 10^{-4}$

Table 1-1. List of triplet exciton diffusion lengths reported in ref. [13] (reprinted from ref. [13] with permission). L_D is the triplet exciton diffusion length and D is diffusion coefficient of triplet excitons.

As seen from the table, there is a wide range of L_t from a few nanometers to a few tens

of micrometers for various organic solids, such as host-gust materials or crystalline materials (Table 1-1).

In order to measure L_t, a several methods have been developed over the years. Each method has advantages and disadvantages, and we need to choose a method that is suitable for each specific organic molecular material. Some representative methods to measure L_t are explained below.

1. Measuring the dependence of phosphorescence quenching efficiency on the thickness of layer

In this method, bilayer film is fabricated for the measurement. Organic molecular layer (layer A) is prepared on a triplet quencher layer (layer B). Generated triplet excitons in layer A diffuse into layer B (Fig. 1-5). When the thickness of layer A is comparable with L_t in the organic molecular material, triplet excitons can reach the interface of the two layers, leading to quenching of triplet excitons (Fig. 1-5). The dependence of phosphorescence intensity on the thickness is analyzed resulting in estimation of the L_t as a fitting parameter[33]. The organic molecular materials used in this method should be efficient phosphorescence molecules for measuring phosphorescence intensity.

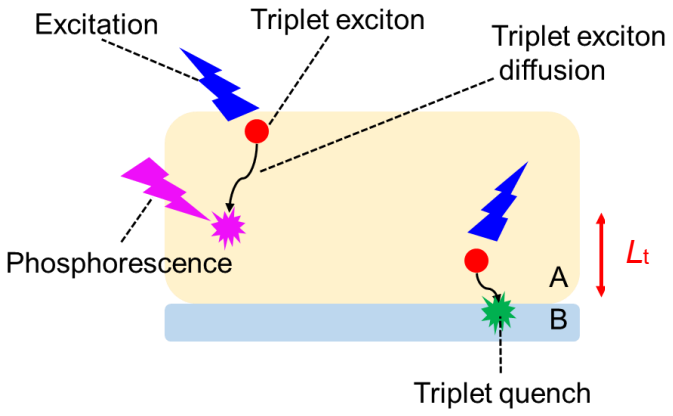

Figure 1-5. Schematic illustration of method 1.

2. Measuring the phosphorescence (triplet) characteristics of a dopant

In contrast to method 1 that requires triplet quencher for measuring L_t, this method uses a phosphorescent dopant for estimation of L_t. For the measurement, a bilayer structure is fabricated. Thin layer of organic molecular material (layer a) is prepared on another layer composed of phosphorescent dopant (layer b) (Fig. 1-6). Triplet excitons generated in the layer a by photoexcitation diffuse into the layer b and transfer its energy to phosphorescent dopant. This is followed by emission from the phosphorescent dopant in layer b (Fig. 1-6). Organic molecular materials which do not show phosphorescence can be used in this method since the objective is emission from phosphorescent molecules in layer b (not emission from layer a). The phosphorescence characteristics such as triplet decay of the dopant are measured and analyzed for estimating L_t which can be obtained as a fitting parameter.[30]

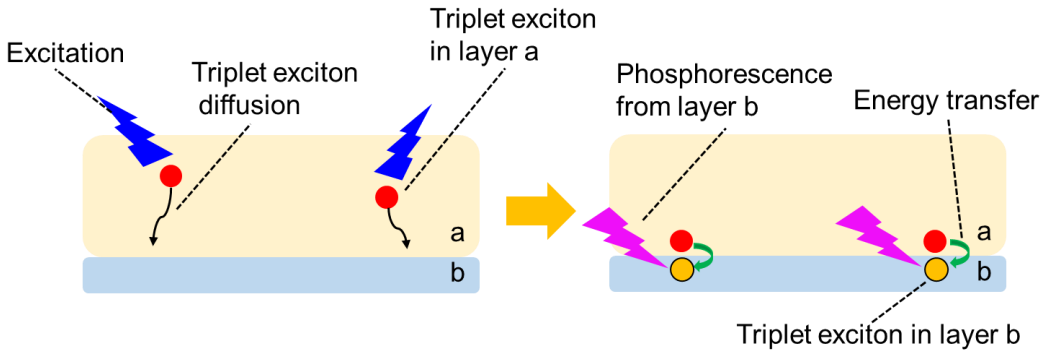

Figure 1-6. Schematic illustration of method 2.

3. Tracking triplet dynamics via transient absorption

In this method, transient absorption of triplet excitons is measured instead of phosphorescence. Therefore, the strong advantage in this method is that it can be applied to materials that rarely show phosphorescence. After photoexcitation, the generated triplet

exciton diffuses in the organic molecular materials (Fig. 1-7). When two triplet excitons encounter and interact with each other, triplet-triplet annihilation (TTA) can occur (Fig. 1-7). After TTA, one triplet exciton is excited into singlet excited state or upper triplet excited state while the other one is deactivated into ground state. Therefore, time-evolution of transient absorption profile is affected by TTA process since the population of triplet excitons is largely dependent on TTA process. As TTA is caused after triplet exciton diffusion, the time-evolution of transient absorption via TTA includes the information of triplet exciton diffusion. The measurement of time-evolution of transient absorption leads to estimation of L_t as a fitting parameter.[25]

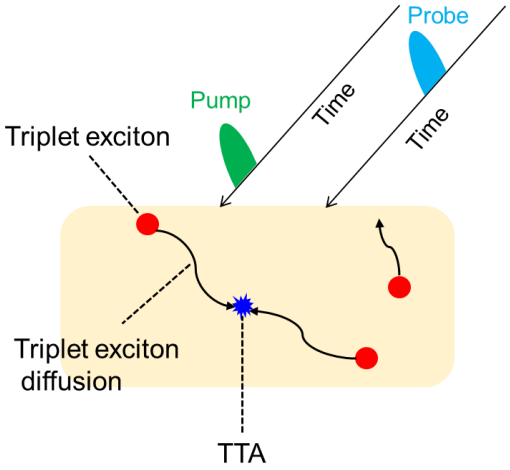

Figure 1-7. Schematic illustration of method 3.

4. Measurement of photocurrent in devices

In this method, a device, such as organic solar cell, is prepared and photocurrent is measured for the evaluation of L_t.[18] Triplet excitons generated in heterojunction-type organic solar cells diffuse into the interface between a donor and acceptor layer, and then the charges are separated (Fig. 1-8). Therefore, the measured external quantum efficiency of photocurrent is dependent on triplet exciton diffusion. Triplet sensitizer is sometimes

used for generating triplet excitons in metal-free conjugated molecules with inefficient ISC rate. L_t can be extracted from the fitting to measured external quantum efficiency of photocurrent.

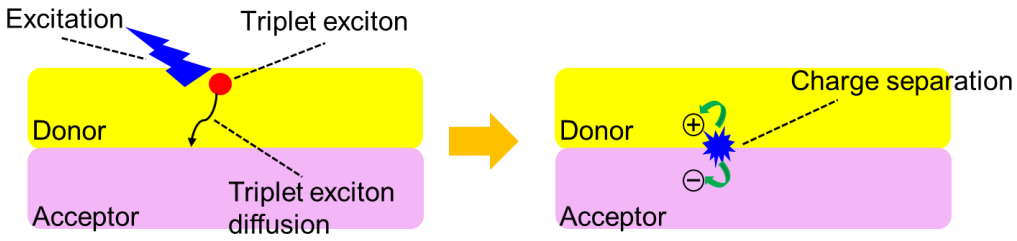

Figure 1-8. Schematic illustration of method 4.

5. Measurement of delayed electroluminescence

In this method, the configuration of an OLED is used to measure L_t, as shown in Fig. 1-9.[29] Very thin layer of an emissive dopant is fabricated in the hole transfer or electron transfer layer at a distance *d* from the exciton generation region (interface between the two charge transfer layers). Consequently, the generated triplet excitons diffuse into the dopant layer and transfer their energy to the dopant molecules, followed by delayed electroluminescence. The intensity of the delayed electroluminescence from the dopant is dependent on triplet exciton diffusion in the hole or electron transfer layers.

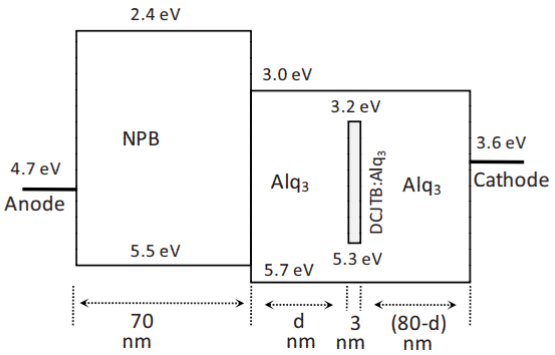

Figure 1-9. Configuration of OLED for the measurement of L_t. Reprinted from ref. [29] with permission.

6. Measurement of time-evolution of delayed fluorescence using a ruling

This is one of the oldest methods to measure L_t. Triplet excitons are often able to diffuse microscale distance in organic molecular materials such as aromatic crystals. In such materials, time evolution of delayed fluorescence is easily modulated by excitation geometries. In this method, this time evolution is measured and analyzed with a ruling for forming excitation patterns.[28] The rate equation of triplet excitons is used for fitting to profile of time-evolution of delayed fluorescence. Thus, the L_t is obtained as a fitting parameter.

7. Direct visualization of triplet exciton diffusion

Recently, an outstanding method that estimates L_t is attracting attention. In this method, triplet exciton diffusion in organic molecular materials such as aromatic crystals is visualized in an optical microscopic image.[20-22] The concept of this method is shown in Fig. 1-10a. Excitation light is irradiated on the crystalline surface with focused diffraction-limited size spot, leading to generation triplet excitons at the irradiation spot.

These triplet excitons diffuse in the crystal and then emit photons in the vicinity of excitation spot. The size of the microscopic image of emission that originates from triplet excitons, such as phosphorescence or TTA-based delayed fluorescence, should be enlarged compared with that of excitation (Fig. 1-10b). By analyzing these two images, L_{t} can be extracted. This method does not require any assumed parameters since triplet exciton diffusion can be visualized in the images directly. Therefore, this method is considered as most reliable method. Very recently, still more sophisticated measurements were reported. Akselrod *et al.* measured and visualized time-evolution of triplet exciton diffusion via TTA-based delayed fluorescence using pump-probe spectroscopy (Fig. 1-10c).[21] Wan *et al.* measured time-evolution of transient absorption using optical microscope (Fig. 1-10d).[22]

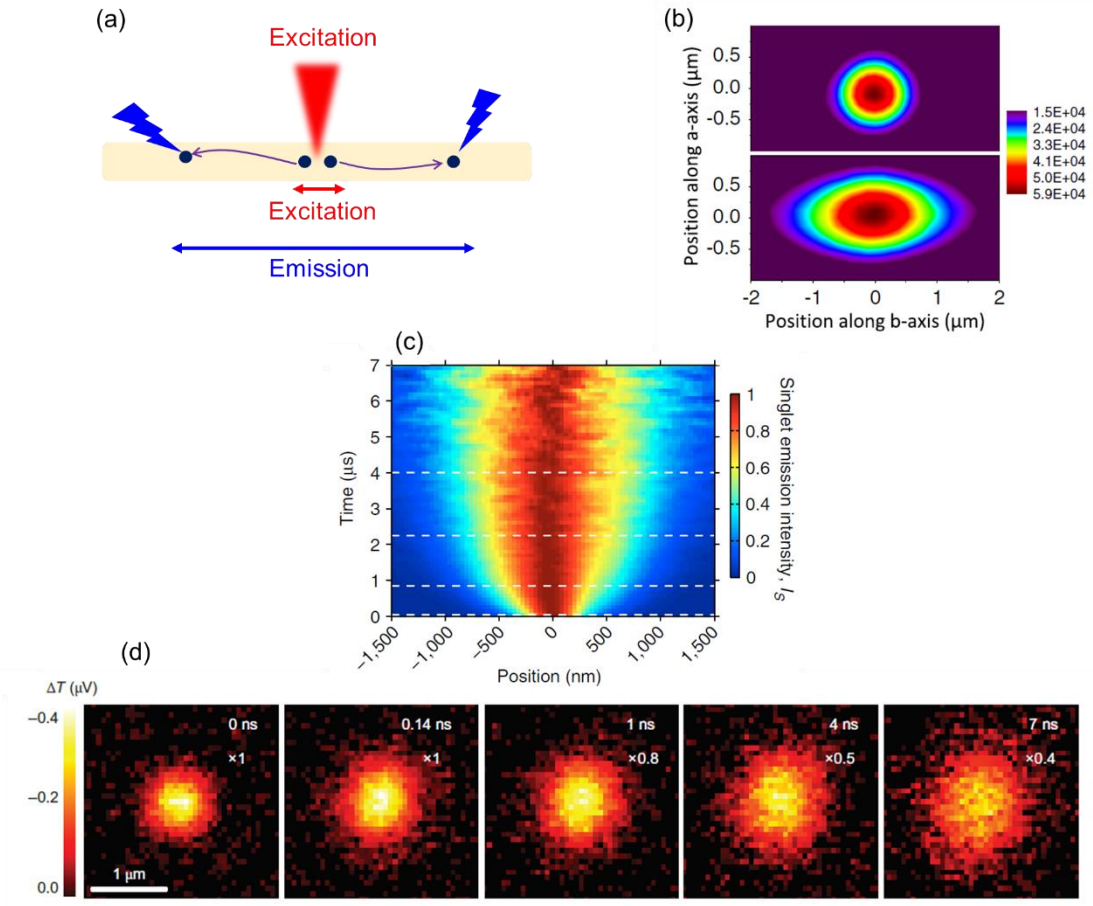

Figure 1-10. (a) Schematic illustration of method 7. (b) Top: The image of excitation focused on rubrene single crystal. Bottom: The image of delayed fluorescence from rubrene single crystal. The image of delayed fluorescence is larger than that of excitation due to triplet exciton diffusion. Reprinted from ref. [20] with permission. (c) Visualized time-evolution of triplet exciton diffusion via delayed fluorescence from tetracene single crystal. The emission profile broadens with time due to triplet exciton diffusion. Reprinted from ref. [21] with permission. (d) The image of transient absorption with focused laser beam excitation on tetracene single crystal. The image of transient absorption broadens with time due to triplet exciton diffusion. Reprinted from ref. [22] with permission.

Transient absorption of singlet excitons and triplet excitons can be distinguished by selecting detection wavelength, which means time-evolution of not only triplet excitons but also singlet excitons can be visualized in this method. Using these sophisticated

methods, triplet exciton diffusion is traced in real time, leading to deeper understanding of triplet exciton diffusion.

8. Measurement of the dependence of UC emission intensity on excitation intensity

In the case of solid-state TTA-based UC materials composed of donor molecules and acceptor molecules, UC emission occurs via triplet exciton diffusion (described later in Chapter 2). In this method, L_t can be calculated using the measured emission decay, the dependence of UC emission on excitation intensity and other parameters.[19] The theory of this method is based on samples in which donor molecules are dispersed homogeneously in the acceptor molecule matric. In such homogeneous UC materials, the value of L_t can be estimated reliably using this method. The details are explained in Chapter 2.

1-3 Aim and outline

As mentioned in the previous section, many kinds of methods for measuring L_t have been developed in order to understand basic characteristics of organic molecular solids or to improve device characteristics. Consequently, triplet exciton diffusion in various materials has been measured, leading to deeper understanding of the characteristics of organic molecules or device, such as organic solar cells or OLEDs. On the other hand, with the recent rapid development of new organic molecular materials, the information of triplet exciton diffusion in these materials is lacking. Thus, there is plenty of room for improvement of methods and characterization of triplet exciton diffusion in these new organic molecular materials is crucial for deeper understanding and further development of this field.

In this thesis, triplet exciton diffusion in next-generation organic molecular materials such as TTA-based UC materials, conjugated polymer nanofibers and metal-free aromatic crystals with ultralong triplet lifetime was studied. In these materials, triplet exciton diffusion has not been measured yet although it plays considerably important roles in the potential device function.

In chapter 2, triplet exciton diffusion in TTA-based binary UC crystals is reported. Triplet exciton diffusion in UC materials is related to UC intensity threshold and to the quantum efficiency of UC emission. However, use of conventional methods to measure L_t is considered difficult in the case of binary UC crystals. Here, we developed a method to measure L_t in binary UC crystals and showed that the method is more accurate and reliable compared with existing conventional methods.

In chapter 3, triplet exciton diffusion in conjugated polymer nanofibers is reported. Conjugated polymers have strong potential for applications in opto-electronic devices such as organic solar cells or OLEDs. In order to improve the efficiency of the photovoltaic devices, long L_t is required. Conjugated polymer nanofibers are expected to be one of the solutions to obtain long L_t in conjugated polymers. Triplet exciton diffusion in nanofibers has been measured and it is shown that L_t in the nanofibers is longer than that in films of the same conjugated polymers, due to good orientation of the polymer chains in the nanofibers. This result shows the potential of nanofiber structures for use in opto-electronic devices.

In chapter 4, triplet exciton diffusion in heavy atom-free aromatic crystals with persistent RTP was measured. In these crystals, triplet exciton diffusion is potentially related to the appearance of persistent RTP. Estimated L_t in such crystal was very short in spite of ultralong-lived triplet excitons. We revealed that short L_t is responsible for

the appearance of persistent RTP since short L_t prevents triplet excitons from reaching quenching sites. Quantum calculations revealed that small molecular orbital overlaps between HOMOs lead to small D_t (because of short L_t). Therefore, small molecular orbital overlaps are one of the crucial factors for obtaining persistent RTP from aromatic crystals.

Chapter 1 References

1. N. J. Turro, V. Ramamurthy, J. C. Scaiano, *Principles of Molecular Photochemistry*, **2009**, University Science Books, The United States of America.
2. M. A. Baldo, D. O'brien, Y. You, A. Shoustikov, S. Sibley, M. E. Thompson, S. R. Forrest, *Nature* **1998**, *395*, 151.
3. M. A. Baldo, S. Lamansky, P. E. Burrows, M. E. Thompson, S. R. Forrest, *Appl. Phys. Lett.* **1999**, *75*, 4.
4. M. A. El-Sayed, *J. Chem. Phys.* **1963**, *38*, 2834.
5. S. Hirata, M. Vacha, *J. Phys. Chem. Lett.* **2017**, *8*, 3683.
6. W. W. Parson, *Modern Optical Spectroscopy*, **2015**, Springer, Heidelberg.
7. T. Tsurumi, H. Hirayama, M. Vacha, T. Taniyama, *Nanoscale Physics for Material Science*, **2010**, CRC Press, The United States of America.
8. T. Förster, *Disc. Faraday Soc.* **1959**, 7.
9. D. L. Dexter, *J. Chem. Phys.* **1953**, *21*, 836.
10. G. L. Closs, M. D. Johnson, J. R. Miller, P. Piotrowiak, *J. Am. Chem. Soc.* **1989**, *111*, 3751.
11. N. Yanai, N. Kimizuka, *Chem. Commun.* **2016**, *52*, 5354.
12. A. Monguzzi, J. Mezyk, F. Scotognella, R. Tubino, F. Meinardi, *Phys. Rev. B: Condens. Matter*, **2008**, *78*,195112.
13. O. V. Mikhnenko, P. W. M. Blom, T.-Q. Nguyen, *Energy Environ. Sci.* **2015**, *8*, 1867.
14. S. R. Yost, E. Hontz, S. Yeganeh, T. Van Voorhis, *J. Phys. Chem.* C, **2012**, *116*, 17369.
15. X.-H. Jin, M. B. Price, J. R. Finnegan, C. E. Boott, J. M. Richter, A. Rao, S. M.

Menke, R. H. Friend, G. R. Whittell, I. Manners, *Science* **2018**, *360*, 897.

16. J. Vogelsang, T. Adachi, J. Brazard, D. A. V. Bout, P. F. Barbara, *Nat. Mater.* **2011**, *10*, 942.
17. Y. Tamai, H. Ohkita, H. Benten, S. Ito, *J. Phys, Chem. Lett.* **2015**, *6*, 3147.
18. B. P. Rand, S. Schols, D. Cheyns, H. Gommans, C. Girotto, J. Genoe, P. Heremans, J. Poortmans, *Org. Electron.* **2009**, *10*, 1015.
19. K. Kamada, Y. Sakagami, T. Mizokuro, Y. Fujiwara, K. Kobayashi, K. Narushima, S. Hirata, M. Vacha, *Mater. Horiz.* **2017**, *4*, 83.
20. P. Irkhin, I. Biaggio, *Phys. Rev. Lett.* **2011**, *107*, 017402.
21. G. M. Akselrod, P. B. Deotare, N. J. Thompson, J. Lee, W. A. Tisdale, M. A. Baldo, V. M. Menon, V. Bulović, *Nat. Commun.* **2014**, *5*, 3646.
22. Y. Wan, Z. Guo, T. Zhu, S. Yan, J. Johnson, L. Huang, *Nat. Chem.* **2015**, *7*, 785.
23. M. Samiullah, D. Moghe, U. Scherf, S. Guha, *Phys. Rev. B* **2010**, *82*, 205211.
24. B. H. Wallikewitz, D. Kabra, S. Gélinas, R. H. Friend, *Phys. Rev. B: Condens. Matter Mater. Phys.* **2012**, *85*, 045209.
25. Y. Tamai, H. Ohkita, H. Benten, S. Ito, *Chem. Mater.* **2014**, *26*, 2733.
26. V. Ern, *J. Chem. Phys.* **1972**, *56*, 6259.
27. P. Avakian, R. E. Merrifield, *Phys. Rev. Lett.* **1964**, *13*, 541.
28. P. Avakian, R. E. Merrifield, *Phys. Rev.* **1966**, *148*, 862.
29. Y. Luo, H. Aziz, *J. Appl. Phys.* **2010**, *107*, 094510.
30. M. A. Baldo, D. F. O'Brien, M. E. Thompson, S. R. Forrest, *Phys. Rev. B* **1999**, *60*, 14422.
31. H. Najafov, B. Lee, Q. Zhou, L. C. Feldman, V. Podzorov, *Nat. Mater.* **2010**, *9*, 938.
32. S. Raišys, K. Kazlauskas, S. Juršėnas, Y. C. Simon, *ACS Appl. Mater.*

Interfaces **2016**, *8*, 15732.

33. T. Fushimi, A. Oda, H. Ohkita, S. Ito, *J. Phys. Chem. B*, **2004**, *108*, 18897.

34. X. Li, M. L. Tang, *Chem. Commun*. **2017**, *53*, 4429.

Chapter 2: Triplet Exciton Diffusion in Up-conversion Materials

2-1 Introduction

2-1-1 Up-conversion materials

UC materials can convert lower energy photons into higher energy ones (Fig. 2-1).[1-10] Recently, UC materials have been attracting attention due to a strong potential for applications in solar cells[11] and photocatalysis.[12] For instance, in general, solar cell materials do not absorb infrared light beyond 1150 nm (Fig. 2-2). However, UC materials can potentially convert low-energy infrared light into visible light that can be absorbed by solar cells, leading to improved utilization of the solar spectrum and to an increase of the efficiency of solar cells (Fig. 2-2).

Two kinds of UC materials have been widely studied so far, based on inorganic molecules such as rare earth complexes (inorganic UC materials)[4] or based on organic molecules (organic molecular UC materials).[1] Inorganic UC materials have already found practical application in bio imaging.[13] However, molar extinction coefficient of rare earth complexes is generally very low to enable absorption of weak incoherent light such as sunlight. Thus, it is difficult to use inorganic UC materials for applications in solar cells. On the other hand, molar extinction coefficient of organic molecules can be very large. Thus, organic molecular UC materials have been studied intensively recently because they show promise for sufficient efficiency of UC emission even under sunlight, making them strong candidate materials for solar cell applications.

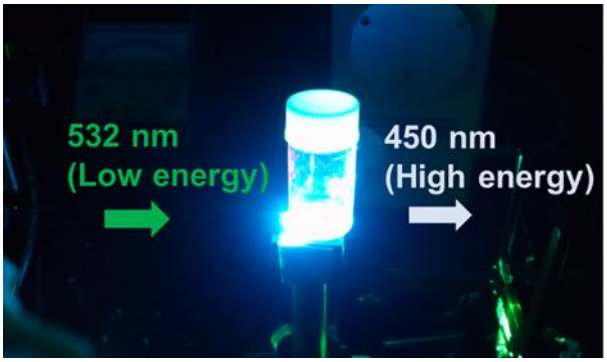

Figure 2-1. TTA-based UC emission excited at 532 nm.

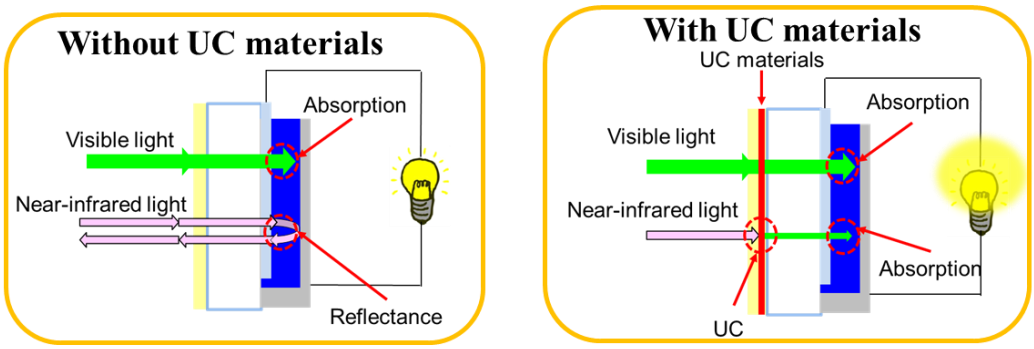

Figure 2-2. Schematic illustration of solar cells with or without UC materials. UC materials can convert near-infrared light into visible light leading to the absorption by solar cells and increase of the efficiency.

2-1-2 Principle of triplet-triplet annihilation based UC materials

In this section, the mechanism of solution-based organic molecular UC materials is explained, as shown schematically in Fig. 2-3. In general, organic molecular UC materials are composed of donor molecules and acceptor molecules. Donor molecules are triplet sensitizers such as heavy-metal complexes. After photoexcitation, singlet excited state of a donor molecule is generated (Fig. 2-3 ①). The generated singlet excited state is converted into triplet excited state via efficient ISC (Fig. 2-3 ②). The

donor triplet energy is transferred to an acceptor molecule resulting in generation of triplet excited state of an acceptor molecule (Fig. 2-3 ③). Such triplet-excited acceptor molecules diffuse in the material. When two such triplet-excited acceptor molecules interact with one another, a possible outcome is that one molecule relaxes to the ground state and the other molecule is excited into a singlet excited state (Fig. 2-3 ④), followed by delayed fluorescence from such singlet. This photophysical process is called triplet-triplet annihilation (TTA). The energy of the singlet excited state of the acceptor molecules is higher than that of the donor, thus energy up-converted photons are emitted from the acceptor molecules (Fig. 2-3 ⑤).

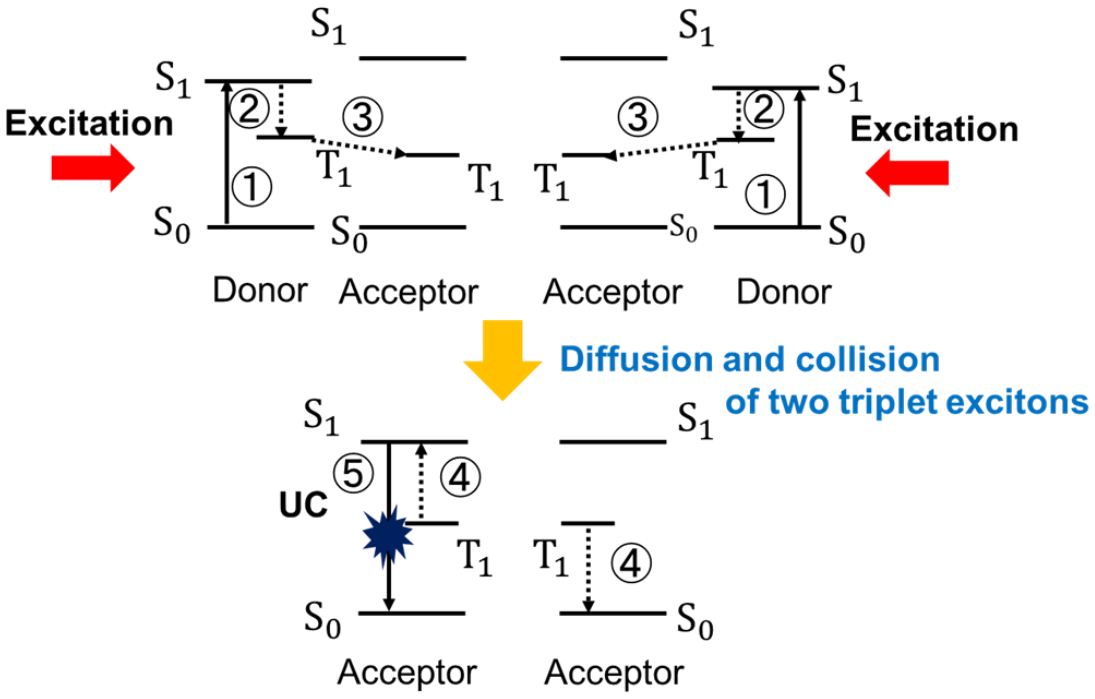

Figure 2-3. Mechanism of TTA-based UC materials.

2-1-2 Solid-state UC materials

One of the obstacles to apply UC materials to solar cells is a large excitation intensity threshold I_{th} for generation of the UC emission. Under the present circumstances, sufficient UC emission is not generated under weak continuous irradiation such as sunlight. Therefore, the greatest interest in the field of UC materials is in decreasing the value of I_{th}. Under weak irradiation intensity, the number of triplet-excited molecules is small, thus triplet-excited molecules have to diffuse long distances for encountering another triplet-excited molecule. In the presence of quenchers which shorten the diffusion length, the triplet-excited molecules can be quenched without encountering other molecules, preventing the subsequent TTA. In order to obtain UC emission from molecules with short diffusion lengths, strong irradiation intensity is required to decrease the distance between two triplet-excited molecules (to increase the density of triplet-excited molecules), resulting in the large value of I_{th}. On the other hand, in the case of long diffusion length, the probability of a triplet-excited molecule to encounter another molecule is higher, resulting in lower I_{th}.

In liquid-state UC materials, both the triplet energy transfer from donor to acceptor as well as the TTA process occur via physical diffusion of the molecules. The diffusion is limited by Brownian motion, which places severe restrictions on the achievable values of diffusion length.[14] In solid-state UC materials, on the other hand, the molecules themselves are immobile but the triplet energy is efficiently transported by Dexter-type energy transfer mechanism between different molecular sites within the solid-state material.[15] Such process is called triplet exciton diffusion, and its diffusion coefficient can be potentially much larger than that based on Brownian motion. Solid-state UC materials have been studied widely in various systems such as host-guest materials,[6,9]

ionic gels[8] or molecular crystalline materials.[16] Considering molecular ordering, triplet exciton diffusion in crystalline UC materials is generally considered larger. Therefore, crystalline UC materials are considered as having strong potential for obtaining longer diffusion lengths L_t, which ultimately lead to lower values of the threshold I_{th}.

2-1-3 Current issues in organic solid-state UC materials and purpose of this study

As mentioned in section 1, in homogeneous soft samples such as liquid-state UC materials and UC gels, triplet exciton diffusion length L_t is extracted from the dependence of UC emission intensity on excitation intensity using parameters such as absorption coefficient of donor molecules a and the efficiency of triplet-triplet energy transfer from the donor molecules to acceptor molecules Φ_{et}.[14,16-17] However, accurate measurements of these parameters are sometimes considered difficult in solid-state UC materials due to possible inhomogeneous dispersion of donor molecules. Thus, new methods are required for accurate and reliable estimation of L_t in crystalline UC materials. A powerful method for estimating L_t in crystalline materials is visualizing triplet exciton diffusion by optical microscope because this method does not require any assumed parameters.[18-20] However, although conventional visualization of triplet exciton diffusion using confocal excitation is effective for large single crystals, polycrystalline binary materials such as crystalline UC materials composed of donor molecules and acceptor molecules are strongly affected by scattering of the confocal excitation, leading to difficulty in estimating L_t. Therefore, alternative and more sophisticated methods are required for measurement of L_t in binary UC crystals. In this chapter, an improved microscopic method for detection of triplet exciton L_t in binary UC crystals is proposed

and demonstrated.

2-2 Experimental

2-2-1 Concept of the method for estimating L_t using an optical microscope

Schematic illustration of the proposed method to measure L_t in binary UC crystals is shown in Fig. 2-4. In this method, a key feature is the use of functionalized inorganic nanoparticles and fluorescence dyes in addition to the UC materials. Hybrid donor nanoparticles (HDPs) are prepared by chemically attaching donor molecules as well as fluorescence dyes to inorganic nanoparticles. The HDPs are dispersed into an UC material composed of polycrystalline acceptor film. By limiting the optical excitation to the HDPs, the generated triplet excited states of the donor molecules can be confined in a nanoscale space around the nanoparticle. Consequently, after triplet energy transfer to acceptor molecules, the population of triplet excitons of acceptor molecules is also confined on the order of the size of an HDP. Thus, excitation scattering that is the inevitable problem in conventional direct methods can be efficiently suppressed in this method.

After photoexcitation of an HDP (Fig. 2-4 (i)), singlet excited states of donor molecules adsorbed on an HDP transform to triplet states via ISC. Further, their triplet energy is transferred to acceptor molecules by Dexter-type energy transfer resulting in generation of triplet excitons of acceptor molecules (Fig. 2-4 (ii)). Triplet excitons of acceptor molecules can diffuse in the polycrystalline acceptor film by the Dexter type energy transfer (Fig. 2-4 (iii)). When two triplet excitons encounter and interact with each other, TTA occurs resulting in generation of a singlet exciton of an acceptor molecule. Fluorescence from the singlet state causes emission of an upconverted photon in the

vicinity of the HDP. On the other hand, fluorescence dyes adsorbed on an HDP emit fluorescence photons at the position of an HDP because these dyes do not transfer their energy to the acceptors. Therefore, the microscopic image size of fluorescence from the fluorescence dyes attached to an HDP is determined only by the diffraction limit of light (point spread function, PSF). The microscopic image size of UC emission from acceptor molecules attached to an HDP, on the other hand, can be larger than the diffraction limited size (or the fluorescence image from the fluorescence dyes) due to the triplet exciton diffusion, enabling determination of the diffusion length L_{t} from these two images (see the appendix for the details).

It should be further noted that one of the advantages of this method is the large number (high local density) of populated triplet excitons. In UC systems composed of molecularly dispersed donors, in general, delayed fluorescence such as UC emission is a slow process because it involves the long-lived triplet excited states. In such photophysical process, the number of upconverted photons emitted per unit time is much smaller compared with prompt fluorescence, which means that upconverted emission generated in the vicinity of a single donor molecule cannot be directly visualized because it is too weak. However, the method proposed here enables emission of sufficient number of upconverted photons in the vicinity of the HDP to detect with a microscope. As such, the method is expected to be suitable for direct measurements of triplet exciton diffusion length in binary UC crystals.

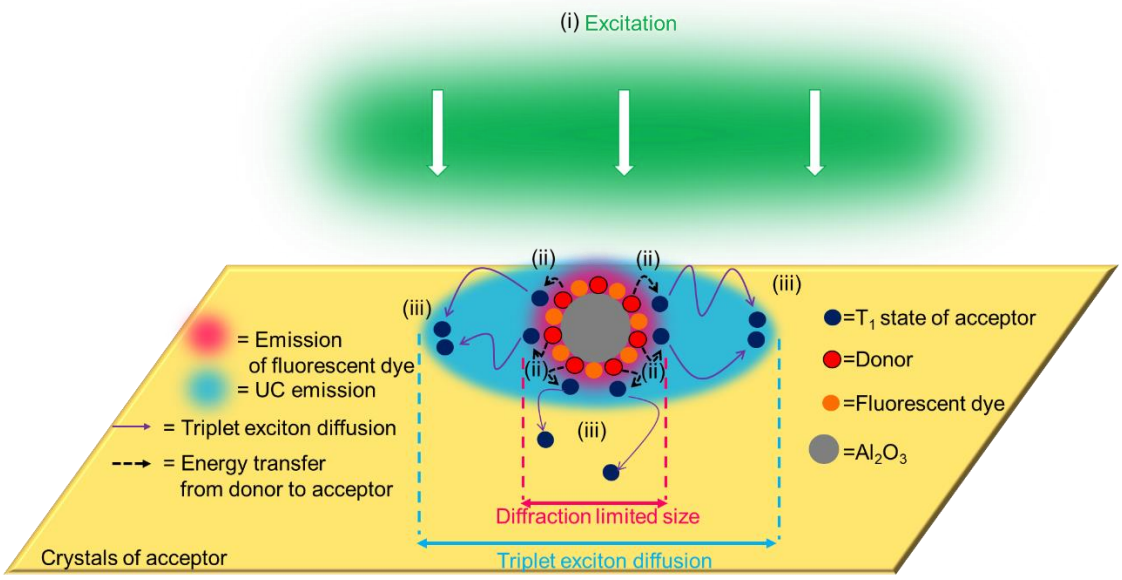

Figure 2-4. Schematic illustration of proposed method for visualizing triplet exciton diffusion. Reprinted from ref. [28].

2-2-2 Experimental method

Pt(II) mesoporphyrin IX (D1, Frontier Scientific) and mesoporphyrin IX-dihydrochloride (FD1, Frontier Scientific) were used as the donor molecules and the fluorescence dyes, respectively. Anthracene (AC, Tokyo Chemical Industry) or 9,10 diphenylanthracene (DPA, Tokyo Chemical Industry) were used as the acceptors. The chemical structures are shown in Fig. 2-5.

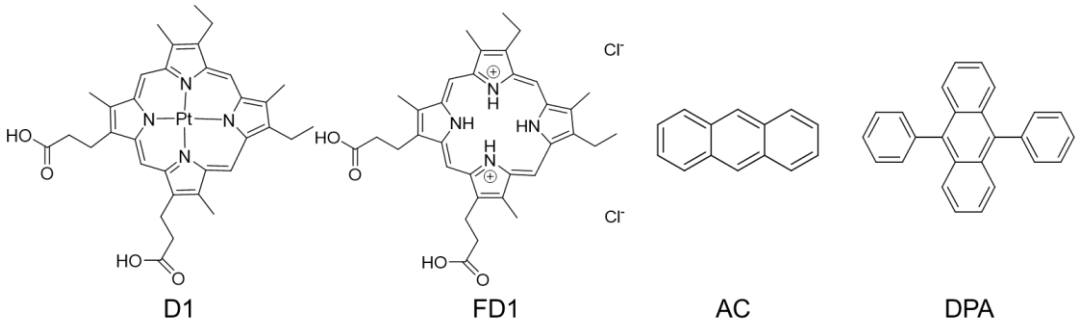

Figure 2-5. Chemical structures of D1, FD1, AC and DPA.

The D1 and FD1 contain carbonyl groups for chemical attachment to the hydroxyl-functionalized alumina nanoparticles to form the HDP.

The HDPs were prepared as follows. D1 and FD1 were dissolved in THF and ethanol, respectively at the concentration of 10^{-4} M. The THF solution of D1, ethanol solution of FD1 and ethanol solution of alumina nanoparticles (30 nm, C.I. KASEI) were mixed in 3:1:1 volume ratio and stirred for 12 hours. The mixed solution was centrifuged (1 ml, 120 rpm, 10 minutes) for separation of HDPs from the solution. After that, the HDPs were re-dispersed with 1 ml of THF. To prepare the binary UC films, the solution containing completely re-dispersed HDPs was diluted 1000 times with a 10^{-1} M THF solution of the acceptor molecules. This solution was spin-coated on the clean glass substrate (3000 rpm, 30 s).

In this experiment, L_{t} measured by the direct microscopic method was compared with a reference value measured by a conventional indirect method. The reference samples for the indirect method were binary UC crystalline films consisting of D1 and acceptor molecules. They were fabricated by dispersing D1 and acceptor molecules in THF solution at 1:1000 molar concentration ratio and drop-casting the solution on a glass substrate.

Bulk absorption spectra and emission spectra in THF solution were measured using a standard UV-visible/NIR spectrophotometer (V-760, Jasco) and a real-time multichannel spectrometer (PMA-12 C10027-01, Hamamatsu Photonics), respectively. UC emission decays were measured by a fluorescence lifetime analysis system (Quantaurus-Tau C11367-24, Hamamatsu Photonics), using a flash lamp as the excitation light (C11567-02, Hamamatsu Photonics) with a bandwidth of about 30 nm. The detection bandwidth was 5 nm.

Optical setup for visualization of triplet exciton diffusion is shown in Fig. 2-6. In this experiment, two kinds of emission from the binary UC crystals were detected simultaneously, namely, UC emission from the acceptor molecules and standard fluorescence (‘down-converted’ emission) from the FD1 chemically attached to HDPs. For that purpose, the emission from the sample was divided spectrally by using an image splitter. Microscopic measurements were carried out with an inverted fluorescence microscope (IX 71, Olympus). The excitation light was a continuous wave laser (TDG532-500, Changchun New Industries Optoelectronics Tech.) at 532 nm that can be absorbed by both D1 and FD1. The emission from the sample was collected by an oil immersion objective lens (×100 UPLSAPO, N.A. 1.3, Olympus) using a dichroic mirror (FF552-Di01-25-25×36, Semrock) and a Notch filter (NF01-532U-25, Semrock). The emission was divided spectrally into a short wavelength part (UC emission) and a long wavelength part (down-conversion emission) by using image splitter (Optosplit II, Cairn) equipped with a dichroic mirror (FF532-Di02-25×36, Semrock). The UC emission passed a short-pass filter (FF01-492/SP-25, Semrock) while the down-conversion emission passed a long-pass filter (LP590 nm, Nikon). The UC emission and down conversion emission were detected and imaged side-by-side on an electron-multiplying (EM) CCD camera (iXon, Andor Technology).

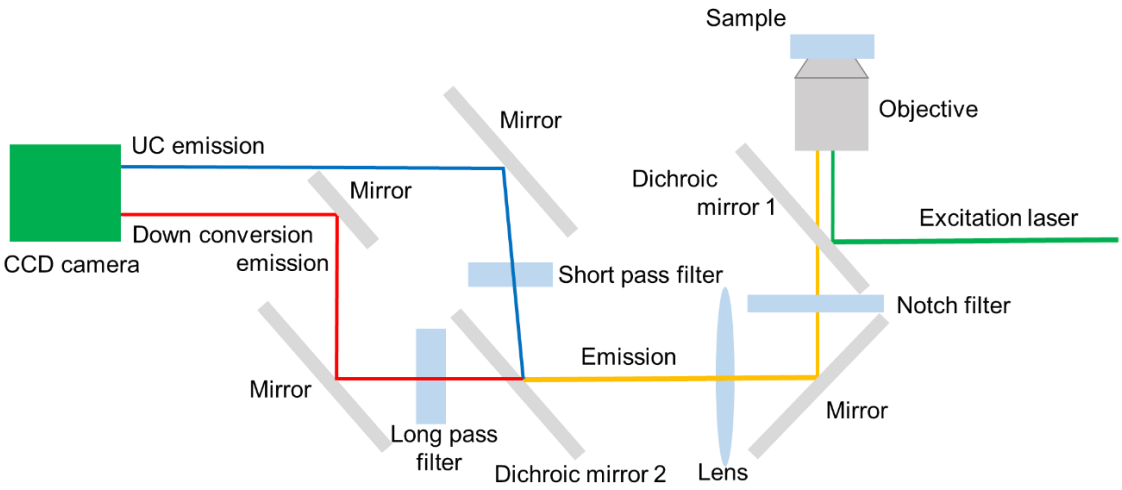

Figure 2-6. Optical setup for visualization of triplet exciton diffusion. Reprinted from ref. [28].

2-3 Result and discussion

2-3-1 Photophysical characterization of the prepared samples

Fig. 2-7a and b shows absorption and emission spectra of the compounds used in this experiment in tetrahydrofuran (THF) solution. As shown in Fig. 2-7a, the D1 and FD1 can absorb photons at 532 nm, enabling simultaneous excitation of both D1 and FD1 chemically attached to an HDP with the 532 nm laser. After photoexcitation, the excited D1 converts to triplet state via efficient ISC due to a heavy-atom effect of the Pt central atom.[21] Triplet energy of DPA and AC is lower than that of D1. Thus, efficient triplet energy transfer from the D1 (attached to the HDP) to DPA or AC occurs, leading to generation of triplet excitons of acceptor molecules (Fig. 2-7c). Diffusion of these triplet excitons and the consequent TTA leads to the generation of singlet excitons of acceptor molecules and UC emission, characterized by the spectra in Fig. 2-7b. On the other hand, the FD1 does not contain heavy-atoms (Fig. 2-5). This means that ISC of FD1 is inefficient[22] and its excited energy is not transferred to the acceptor molecules (Fig. 2-7c)

but emitted as fluorescence, characterized by the spectra in Fig. 2-7a. This fluorescence from FD1 is used to localize the HDPs in the microscopic images and to measure the reference size of the emission spot in the absence of triplet exciton diffusion.

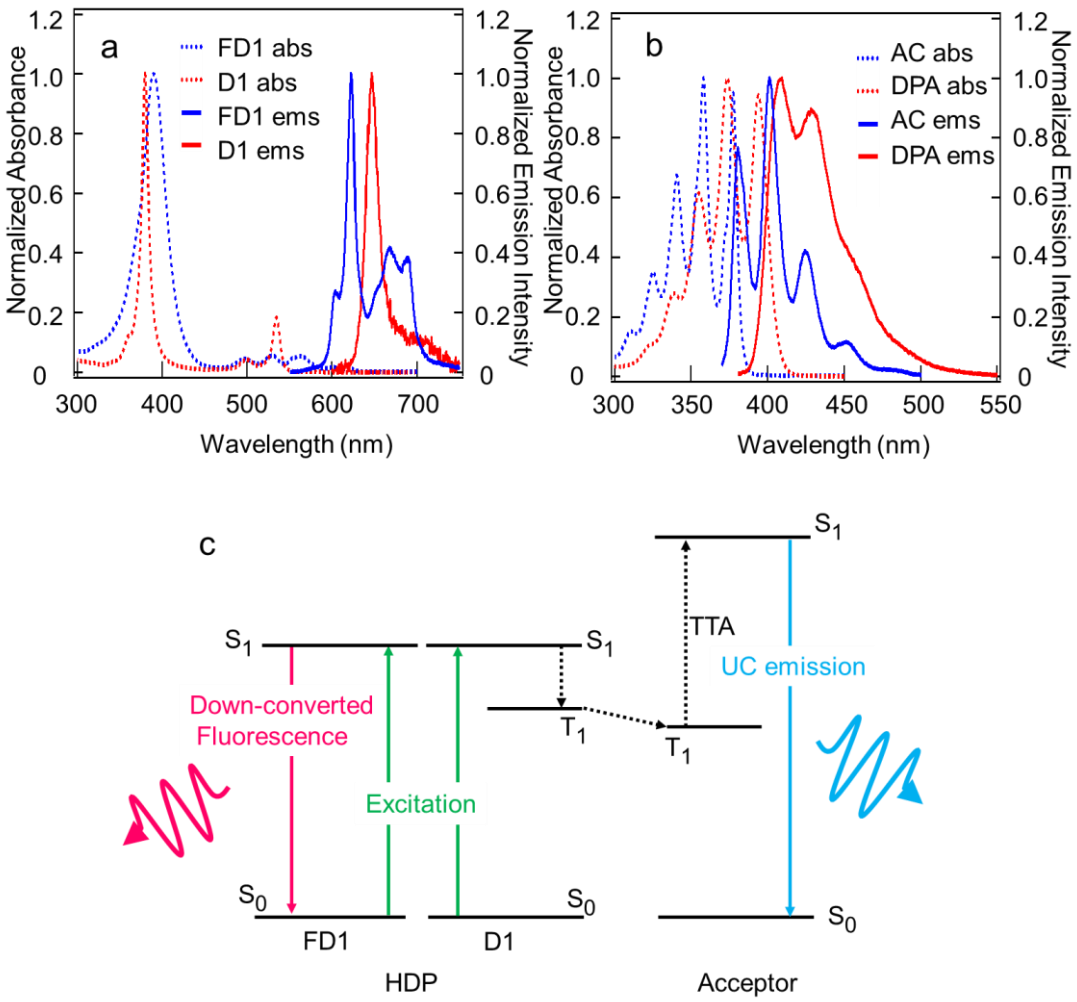

Figure 2-7. (a) Absorption and emission spectra of D1 and FD1 in THF. (b) Absorption and emission spectra of AC and DPA in THF. (c) Energetic diagram in the UC materials composed of HDPs and acceptor molecules. Reprinted from ref. [28].

Microscopic images of the UC films are shown in Fig. 2-8. The light spots shown in Fig.

2-8a represent images of UC emission in the vicinity of HDPs in a polycrystalline DPA film while the light spots shown in Fig. 2-8b are the corresponding fluorescence ('down-conversion') images from the FD1 chemically attached to the HDPs. Both light spots can be observed with sufficient signal-to-noise ratio, thus confirming the practical applicability of the method for measuring triplet exciton diffusion in polycrystalline films.

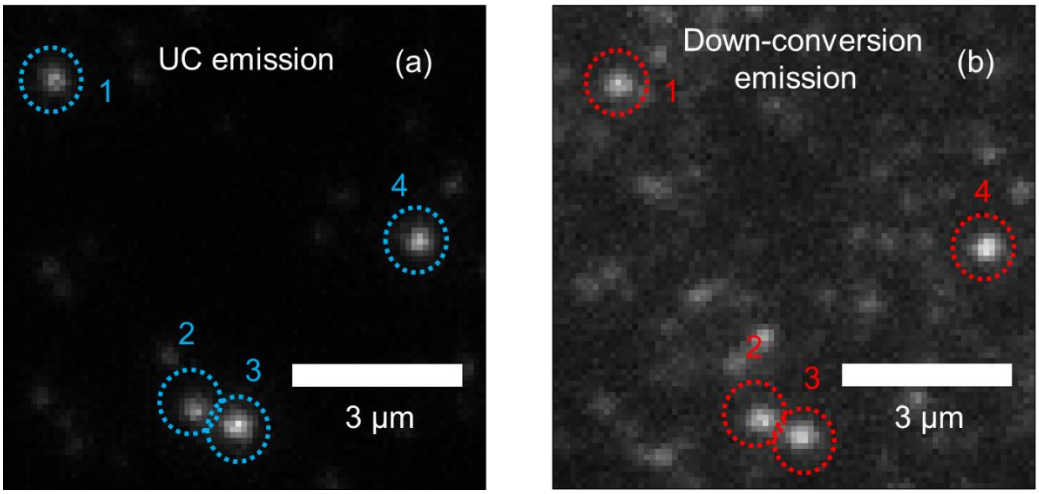

Figure 2-8. (a) Short wavelength part (UC emission) of a spectrally divided CCD microscopic image. Each spot (surrounded by blue circle) represents UC emission from DPA in the vicinity of an HDP. (b) Long wavelength part (fluorescence or 'down-conversion emission') of the spectrally divided CCD image. Each spot (surrounded by red circle) represents corresponding down-conversion emission from FD1 at the position of HDP.

2-3-2 Triplet exciton diffusion in polycrystalline AC film

Fig. 2-9a and b show detailed microscopic images of fluorescence (down-conversion emission) from FD1 chemically attached to an HDP and of UC emission from AC in the vicinity of the HDP, respectively. Fig. 2-9c shows one-dimensional intensity cross-sections of the image spots of the UC emission from AC and of the fluorescence (down-conversion emission) from FD1. The image of UC emission is obviously larger than that of fluorescence (Fig. 2-9a and b). This means that the process of triplet exciton diffusion

in the polycrystalline binary UC materials was visualized directly. It should be noted that both images shown in Fig. 2-9a and b were affected by a substantial contribution of PSF which itself is larger for longer wavelength (down-conversion emission).

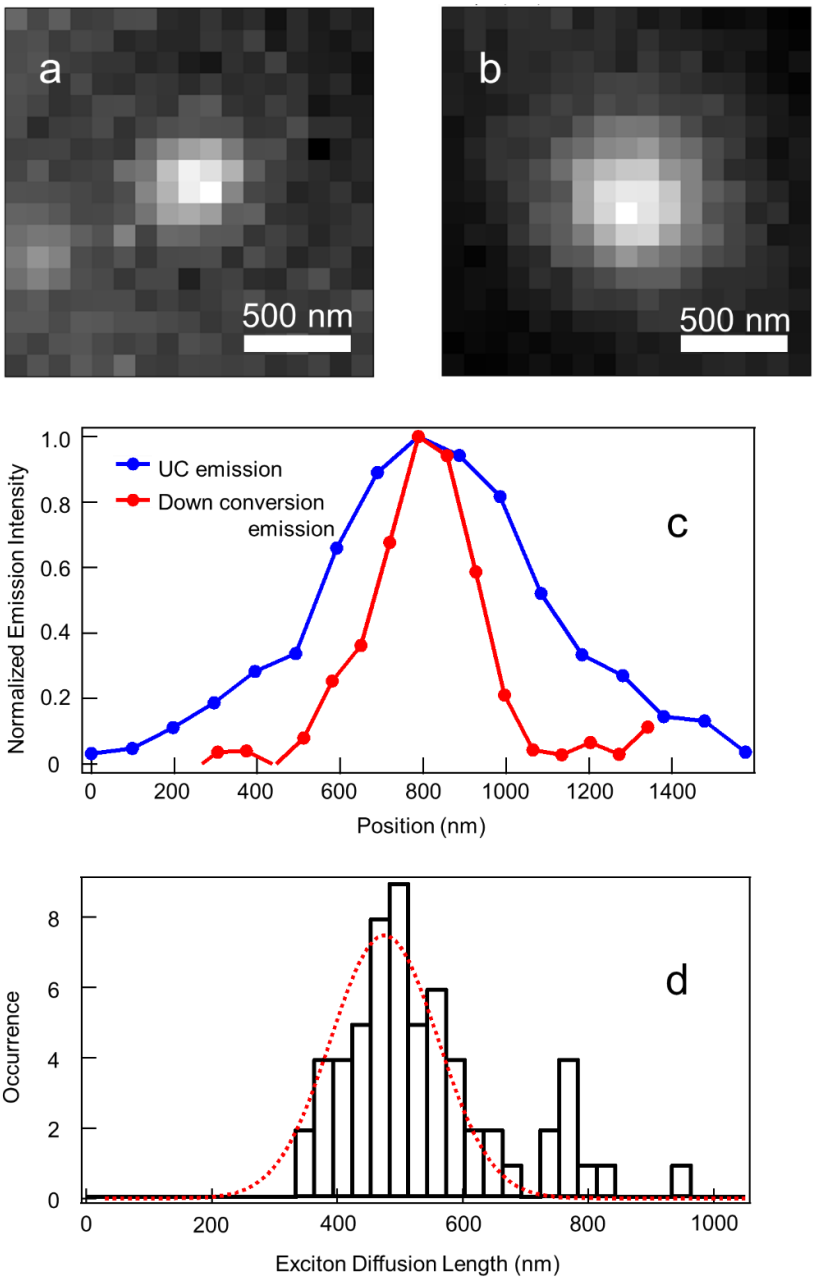

Figure 2-9. (a) CCD image of a spot of the down-conversion emission from a single HDP. (b) CCD image of a spot of the UC emission from AC at the vicinity of a single HDP. (c) One-dimensional intensity cross-sections of the spots of UC emission and down-conversion emission. Black line is fits of the UC emission cross-section to equation (2-3). (d) Histogram of L_t for AC. The red dotted line is Gaussian fits to the distribution. Reprinted from ref. [28].

Therefore, in Fig. 2-9c and in subsequent analysis, the PSF in the region of fluorescence (down-conversion emission) at 625 nm was corrected to the corresponding region of UC emission (see the appendix for the details).

In the following, we consider a theoretical background to interpret the above experimental observations. Density of triplet excitons $n_{\mathrm{t}}(\mathrm{x})$ along the direction *x* in the sample can be expressed as

$$n_{\mathrm{t}}(x) = T_0 \exp(-{}^{x}/_{L_{\mathrm{t}}}) \qquad (2\text{-}1)$$

where T_0 is a constant.[20] Since the density of singlet excitons $n_{\mathrm{s}}(\mathrm{x})$ is quadratically proportional to $n_{\mathrm{t}}(\mathrm{x})$, due to the two-photon nature of the TTA process, $n_{\mathrm{s}}(\mathrm{x})$ can be approximated using the equation (2-1) as

$$n_{\mathrm{s}}(x) \sim n_{\mathrm{t}}^2(x) \sim S_0 \exp(-{}^{2x}/_{L_{\mathrm{t}}}) \qquad (2\text{-}2)$$

where S_0 is a constant. The image of fluorescence from FD1 is determined by the resolution of the microscope (diffraction limited size) that can be approximated by a PSF because the size of an HDP is so small that its contribution to the image can be neglected. The size of the PSF is determined from the image of fluorescence from FD1. The image size of UC emission is given by a convolution of $n_{\mathrm{s}}(\mathrm{x})$ and PSF. Therefore, the UC emission intensity I_{UC} along the direction *x* can be expressed as

$$I_{\mathrm{UC}}(x) = n_{\mathrm{s}}(x) \times f_{\mathrm{PSF}}(x) \qquad (2\text{-}3)$$

where $f_{\mathrm{PSF}}(x)$ is the profile of PSF along the direction *x*. In the subsequent analysis, the two-dimensional convolution function of UC emission $I_{\mathrm{UC}}(x, y)$ was used for the fitting to the CCD images (such as Fig. 2-9b) in order to estimate L_{t} as a fitting parameter (see the appendix for the details). The UC emission spots were slightly asymmetrical due to

the anisotropic molecular packing in the acceptor crystal leading to different values of L_t along two orthogonal directions. In the analysis, an average of L_t in the two orthogonal directions was used for the comparison with conventional measurements (described later).

Fig. 2-9d shows a histogram of L_t values estimated as described above from the measurement of UC emission in the vicinity of 46 individual HDPs. For reference, histograms of L_t values along the two orthogonal directions are shown in appendix.

From the histogram shown in Fig. 2-9d, the mean value of L_t is estimated as 491 nm. Triplet exciton diffusion in AC single crystal has been measured before and the value of L_t was on the order of 10 μm.[23,24] However, in order to obtain such an ultralong L_t, highly purified and mm-sized single crystals are required to prevent the triplet excitons from quenching at defects or surfaces of the crystal. Fig. 2-10 shows an image of the UC material film used here by scanning electron microscopy (SEM). The image shows polycrystalline AC film composed of micrometer-size flakes of AC and of the HDPs. In this context, the estimated value of L_t of 491 nm, which is on the order of the AC grain size, can be considered reasonable.

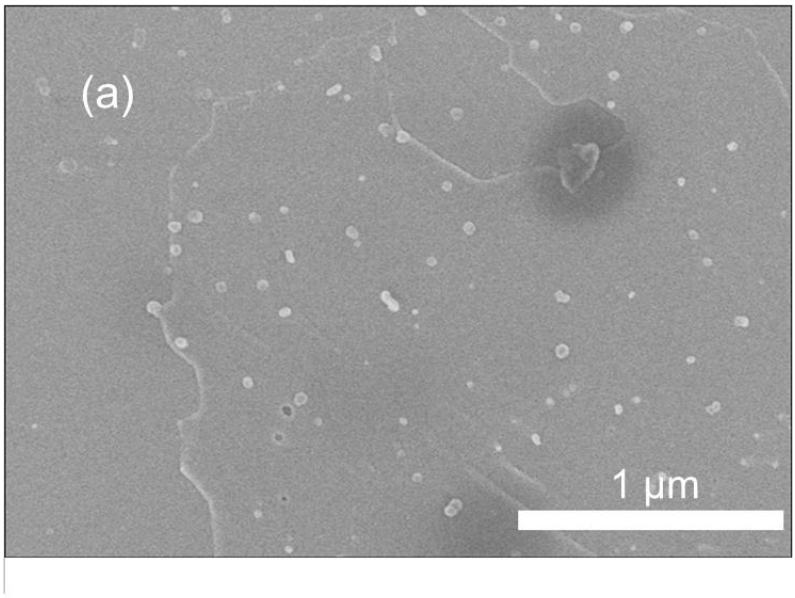

Figure 2-10. SEM image of AC crystalline film. Reprinted from ref. [28].

2-3-3 Triplet exciton diffusion in polycrystalline DPA film

DPA is the standard acceptor molecule for obtaining efficient UC emission.[1,5,7,16,25] Thus, the measurement and understanding of triplet exciton diffusion in DPA is important to improve the characteristics of UC materials. Fig. 2-11a and b show images of fluorescence (down-conversion emission) from FD1 chemically attached to an HDP and of UC emission from DPA in the vicinity of the HDPs, respectively. Fig. 2-11c shows one-dimensional intensity cross-sections of the spots of UC emission from DPA and of the fluorescence (down-conversion emission). Compared with the result of polycrystalline AC film, the image of UC emission from polycrystalline DPA film is only slightly enlarged (Fig. 2-11c). This means that the triplet exciton diffusion in DPA is not as efficient compared with AC. The histogram of L_t in polycrystalline DPA film was constructed by analyzing data from 37 individual HDP spots (Fig. 2-11d). From Fig. 2-11d, the mean value of L_t was 172 nm.

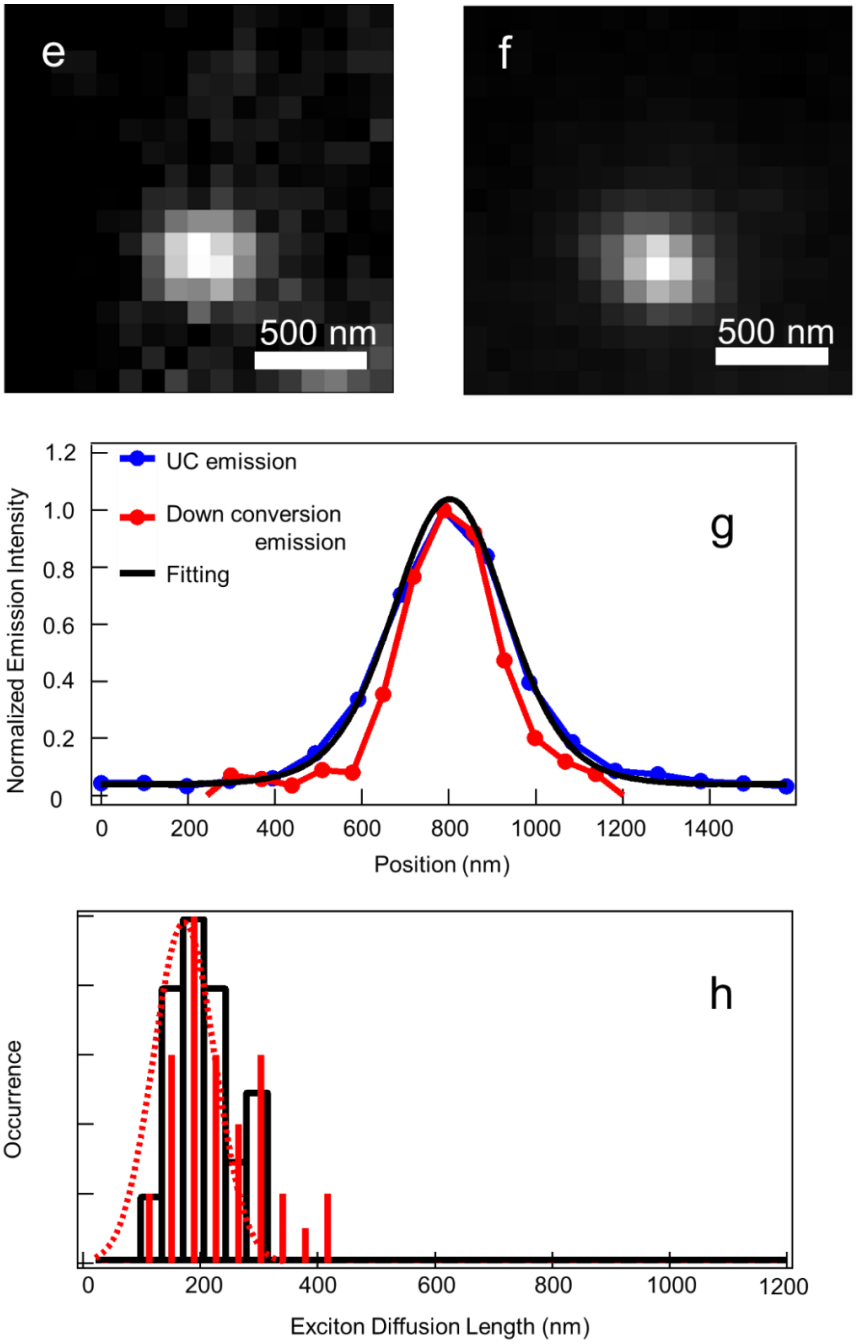

Figure 2-11. (a) CCD image of a spot of the down-conversion emission from a single HDP. (b) CCD image of a spot of the UC emission from DPA at the vicinity of a single HDP. (c) One-dimensional intensity cross-sections of the spots of UC emission and down-conversion emission. Black line is fits of the UC emission cross-section to equation (2-3). (d) Histogram of L_t for DPA. The red dotted line is Gaussian fits to the distribution. The red solid lines represent a histogram of crystal grain sizes of DPA as analyzed SEM image of the films. Reprinted from ref. [28].

The mean L_t in DPA is shorter than that in AC. The difference of L_t between DPA and AC can be attributed to the differences of their microscopic structures. The difference in the crystal structure of DPA and AC causes a difference in the molecular orbital overlap in triplet excited state. Since triplet exciton diffusion occurs via Dexter-type energy transfer, molecular orbital overlap related to S_0-T_1 transition is required for efficient triplet exciton diffusion. Fig. 2-12 shows the molecular orbital in T_1 of DPA and AC, respectively.

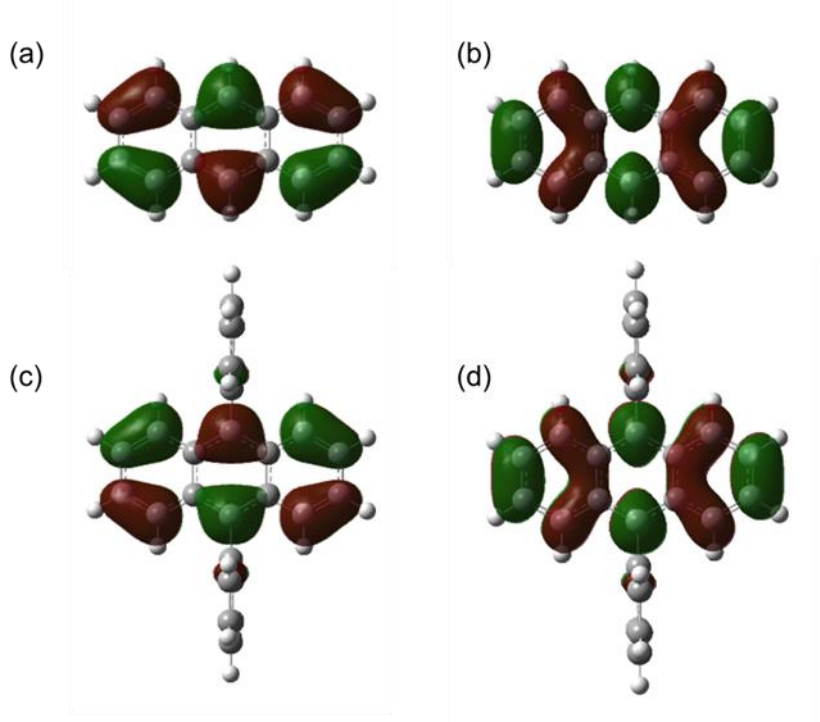

Figure 2-12. (a, c) LUMO of (a) AC and (c) DPA. (b, d) HOMO of (b) AC and (d) DPA. Calculation were performed using density functional theory (Gaussian 09, B3LYP functional, 6-31G(d,p) basis set) using conformation optimized at T_1. Reprinted from ref. [28].

The molecular orbitals of both AC and DPA are localized on the anthracene part (Fig. 2-12). However, the twisted structure of phenyl group in DPA prevents DPA molecules from optimal crystalline packing. Thus, compared to the AC, the molecular orbital overlap in DPA crystals is considered inefficient due to the presence of twisted phenyl group. This

microscopic structural difference is one of the origins of the different values of L_t.

Macroscopically, the crystal size can be also the origin of the different value of L_t. The value of L_t is never larger than the crystal grain size since triplet excitons would be quenched (likely by oxygen) at the surface of the crystal. As seen in the SEM image of the polycrystalline AC film (Fig. 2-10), the crystal flakes size in AC films is on the order of a few micrometers, and the estimated L_t in AC film is on the order or smaller than this crystal size. On the other hand, in the case of polycrystalline DPA film, the crystal grain size of DPA is on the other of a few hundreds of nanometers as shown in the corresponding SEM image (Fig. 2-13). The crystal size of DPA is analyzed and shown as an overlaid size histogram in Fig. 2-11d. The mean crystal size of DPA estimated from the peak of the histogram is 213 nm. This value is well comparable with the mean value of L_t of 172 nm in the DPA film, which means that the triplet exciton diffusion is limited by the crystal grain size of DPA. We would like to note that the observed L_t in polycrystalline DPA film is smaller than the diffraction limited size of a confocal excitation. This situation points to the advantage of our method which uses the point-like source (HDP) of the triplet excitons for an accurate measurement.

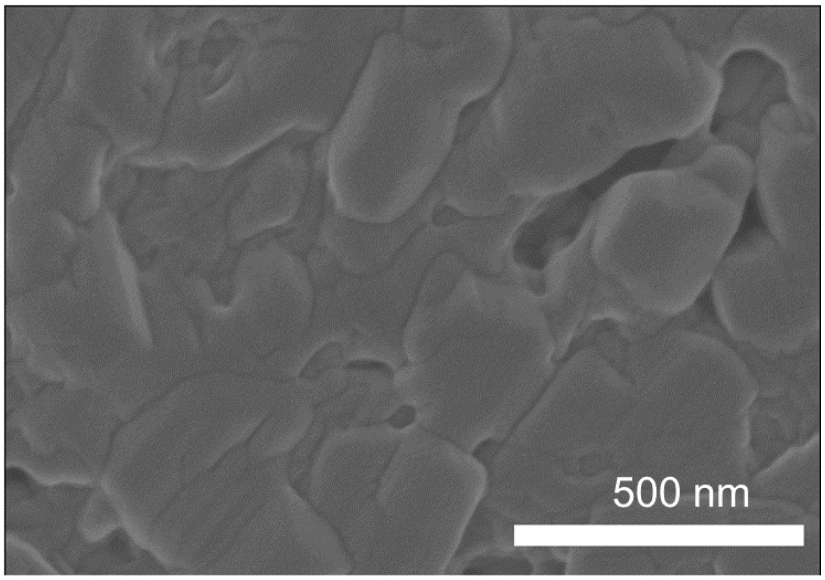

Figure 2-13. SEM image of DPA crystalline film. Reprinted from ref. [28].

2-3-3 Comparing the value of L_t measured by proposed method with that measured by a conventional indirect method

In this section, L_t in polycrystalline AC film and polycrystalline DPA films were measured for comparison by a conventional indirect method. In the conventional method, L_t can be determined by the following equation for I_{th}

$$I_{th} = \frac{1}{\Phi_{et}\alpha 8\pi a D_a \tau_a^2} \qquad (2\text{-}4)$$

where a is an interaction distance of a triplet pair of the acceptor molecules, D_a is a diffusion coefficient of the triplet exciton of the acceptor molecules and τ_a is a triplet lifetime of the acceptor molecules.[14] Considering that L_t is determined from D_a and τ_a as shown in equation (1-3), L_t can be extracted from equation (2-4). The value of I_{th}, and consequently the value of L_t, can be determined by measuring the dependence of UC emission intensity on the excitation intensity. In this measurement, the use of HDPs was not suitable because fast photobleaching of the HDPs did not enable an application of a

sufficient range of excitation intensities. Instead, binary UC crystals in which donor molecules were dispersed into polycrystalline AC or DPA film were prepared. In order to estimate the L_t in this conventional method, Φ_{et} was assumed as 1 because donor molecules were surrounded by acceptor molecules and efficient energy transfer from donor molecules to acceptor molecules was expected. On the other hand, α can be expressed as follows

$$\alpha = \varepsilon_d c \ln 10 \qquad (2\text{-}5)$$

where ε_d is the molar extinction coefficient of donor molecules and c is the concentration of donor molecules. For the estimation of α, c was calculated assuming that the density of the acceptor molecules was 1.25 g cm^{-3}. The value of a was taken from ref. [14]. L_t can be estimated by measuring I_{th} and τ_a, and using the equation (2-4) and equation (1-3).

For the estimation of τ_a, the decay time of UC emission τ_{UC} was measured. The relationship between τ_a and τ_{UC} can be expressed as follows[26]

$$\tau_a = 2\tau_{UC}. \qquad (2\text{-}6)$$

Fig. 2-14 shows temporal intensity decays of UC emission from polycrystalline AC and DPA films. The decays were multi-exponential due to the presence of inhomogeneities in the UC binary crystals. Three-exponential fitting was used to determine the value of τ_{UC}. As a result of the fitting, the average τ_{UC} of AC and DPA was calculated as 7.4×10^{-5} s and 1.8×10^{-4} s, respectively. We would like to note that only the longest component of the decay is often used to estimate L_t in literature.[27] However, here we used the average τ_{UC} because the use of only the longest component can lead to shorter L_t and can cause underestimation of the triplet diffusion (see the appendix for the details).

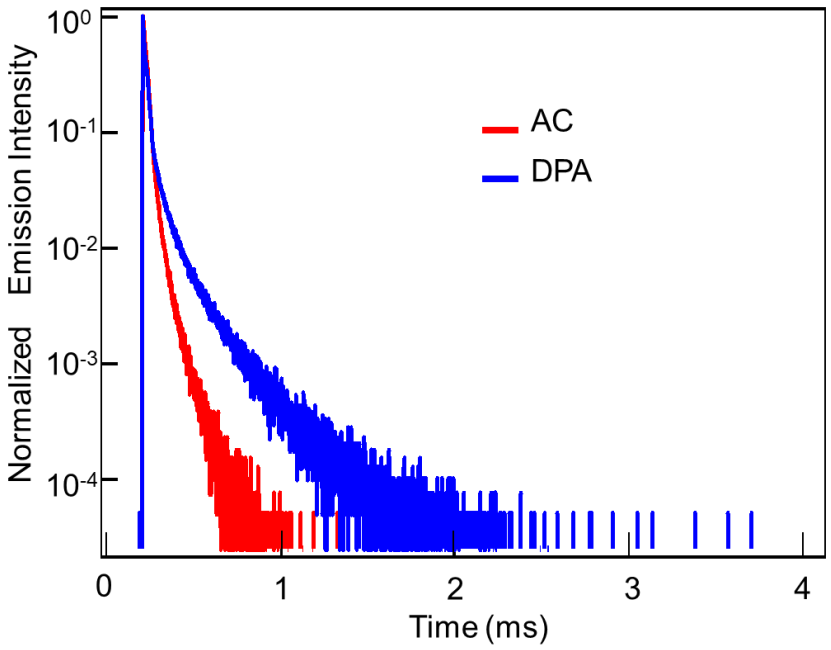

Figure 2-14. Decay of UC emission under pulsed excitation at 532 nm. Reprinted from ref. [28].

Further, for the estimation of I_{th}, the dependence of UC emission intensity on excitation intensity was measured (Fig. 2-15). As shown in the log-log plot in Fig. 2-15, the slope of UC emission intensity is 2 at lower excitation intensity and changes to 1 at higher excitation intensity. In the region of lower excitation intensity, since the TTA process is a second-order reaction, the dependence of UC emission intensity on excitation intensity is quadratic. However, as the excitation intensity becomes stronger, the population of triplet excitons also increases. As a result, a newly generated triplet exciton can interact with a nearby existing triplet exciton, leading to a change of the value of the slope from 2 to 1. The I_{th} is determined from the intersection of these two slopes (Fig. 2-15). The I_{th} values of polycrystalline AC film and of polycrystalline DPA film were 5.5×10^{1} mW cm^{-2} and 4.4×10^{3} mW cm^{-2}, respectively. As mentioned above, molecular orbital overlap of AC is more efficient, resulting in the lower value of the estimated I_{th}.

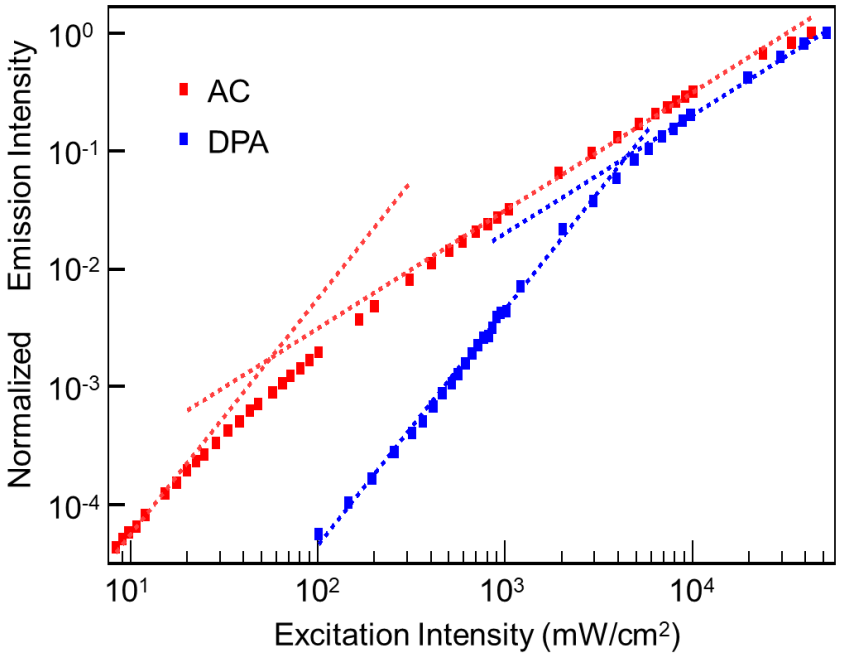

Figure 2-15. Dependence of UC emission intensity on excitation intensity. Reprinted from ref. [28].

Using the calculated and estimated parameters in the equation (2-4) and equation (1-3), L_t of AC and DPA can be estimated as 50 nm and 4.9 nm, respectively.

Compared with L_t measured by the direct microscopic method, the values of L_t estimated from the conventional method are about an order of magnitude smaller. The possible origin of the different values of L_t measured by two methods is a nonuniform distribution of D1 in the acceptor films. The theory of the conventional method is based on a uniform molecular distribution of the donor molecules. However, it possible that D1 is actually segregated from acceptor and forms aggregates in the film. The triplet energy levels of aggregates can be lower than those of isolated donor molecules. If so, triplet energy transfer from such aggregates of D1 to acceptor molecules would be less efficient, which would mean that aggregates of D1 cannot contribute to the UC emission. The presence of aggregates in binary UC crystals can be confirmed by measuring the absorption spectrum

of the crystals using an optical microscope (Fig. 2-16). As shown in Fig. 2-16, the absorption spectrum of D1 in the UC crystal was red-shifted compared with that in THF solution (Fig. 2-7a), which indicates the presence of aggregates. When the value of c is calculated, only D1 in dispersed isolated state (not aggregates of D1) is considered. Thus, the value of c was overestimated because we assumed that the D1 were uniformly dispersed and there were no aggregates. The overestimation of c, *i.e.* the overestimation of α, leads to underestimation of L_t because L_t is inversely proportional to α as seen in equation (2-4). In order to measure L_t by the conventional method accurately, it is necessary to measure an accurate value of α. To obtain accurate α, the accurate length of an optical path is required. However, the accurate measurement of the length of an optical pass in polycrystalline films is somewhat difficult. These experimental difficulties associated with the conventional method again point out the suitability and advantages of the direct microscopic method for measuring L_t in polycrystalline UC materials.

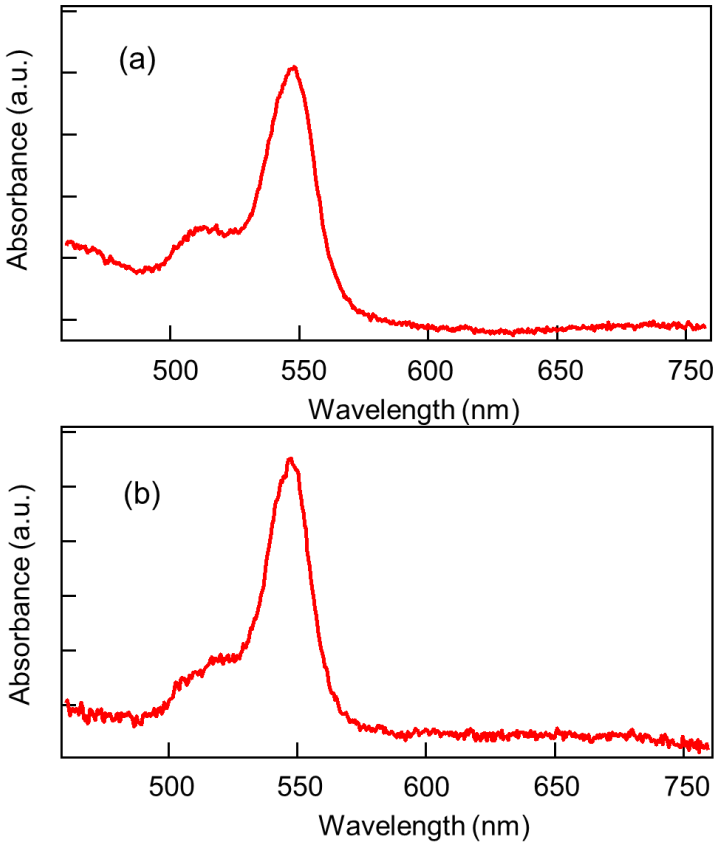

Figure 2-16. Absorption spectrum of D1 in polycrystalline film of (a) AC and (b) DPA. Reprinted from ref. [28].

2-4 Summary

In this chapter, visualization of triplet exciton diffusion in polycrystalline upconversion materials was discussed and demonstrated. The key concept of the proposed method is the use of a point-like excitation source of triplet excitons in the form of dye-functionalized inorganic nanoparticles. The use of the nanoparticles leads to a generation of high concentration of triplet excitons in a nanoscale-confined spot, the size of which is smaller than the diffraction limit of light. As a result, triplet exciton diffusion in polycrystalline materials can be visualized without the effect of excitation scattering. In addition, the proposed method is free of artefacts such as inhomogeneous distribution (or

aggregation) of donor molecules that can be an obstacle in indirect conventional methods. The direct visualization method that was proposed and demonstrated here is an accurate and reliable method for nanoscale characterization of crystalline UC materials.

Chapter 2 Appendix

Two-dimensional convolution function for image fitting.

In the CCD camera images such as Fig.2-9b and Fig. 2-11b, the intensity distribution $I_{\mathrm{UC}}(x)$ is a convolution of $n_{\mathrm{s}}(x)$ and PSF, as shown in the equation (2-3). Assuming that the $f_{\mathrm{PSF}}(x)$ can be approximated by a Gaussian profile with σ_{PSF}^2 its variance, and using the equation (2-3) and (2-2), $I_{\mathrm{UC}}(x)$ can be expressed as

$$I_{\mathrm{UC}}(x) = \exp\left({}^{2x}/_{L_{\mathrm{t}}}\right) \times \mathrm{erfc}\left(\frac{{}^{2\sigma_{\mathrm{PSF}}^2}/_{L_{\mathrm{t}}}+x}{\sqrt{2}\sigma_{\mathrm{PSF}}}\right) + \exp({}^{-2x}/_{L_{\mathrm{t}}}) \times \mathrm{erfc}\left(\frac{{}^{2\sigma_{\mathrm{PSF}}^2}/_{L_{\mathrm{t}}}-x}{\sqrt{2}\sigma_{\mathrm{PSF}}}\right), \quad \text{(A2-1)}$$

where erfc is the complementary error function.

In order to estimate L_{t}, a two-dimensional convolution function $I_{\mathrm{UC}}(x,y)$ was used for the UC image fitting. $I_{\mathrm{UC}}(x,y)$ can be expressed as

$$I_{\mathrm{UC}}(x,y) = \left[\exp\left({}^{2x}/_{L_{\mathrm{tx}}}\right) \times \mathrm{erfc}\left(\frac{{}^{2\sigma_{\mathrm{PSF}}^2}/_{L_{\mathrm{tx}}}+x}{\sqrt{2}\sigma_{\mathrm{PSF}}}\right) + \exp({}^{-2x}/_{L_{\mathrm{tx}}}) \times \mathrm{erfc}\left(\frac{{}^{2\sigma_{\mathrm{PSF}}^2}/_{L_{\mathrm{tx}}}-x}{\sqrt{2}\sigma_{\mathrm{PSF}}}\right)\right] \times$$
$$\left[\exp\left({}^{2y}/_{L_{\mathrm{ty}}}\right) \times \mathrm{erfc}\left(\frac{{}^{2\sigma_{\mathrm{PSF}}^2}/_{L_{\mathrm{ty}}}+y}{\sqrt{2}\sigma_{\mathrm{PSF}}}\right) + \exp({}^{-2y}/_{L_{\mathrm{ty}}}) \times \mathrm{erfc}\left(\frac{{}^{2\sigma_{\mathrm{PSF}}^2}/_{L_{\mathrm{ty}}}-y}{\sqrt{2}\sigma_{\mathrm{PSF}}}\right)\right], \quad \text{(A2-2)}$$

where L_{tx} and L_{ty} are the triplet exciton diffusion lengths along the direction *x* and *y*, respectively. The values

of ${\sigma_{\mathrm{PSF}}}^2$ are obtained from 2D Gaussian fitting of the fluorescence images of the FD1 attached to the HDP (Fig. 2-9a and Fig. 2-11a). Although the fluorescence image spots shown in Fig. 2-9a and Fig. 2-11a are expressed by a a convolution of the microscopic PSF with the HDP physical size (30 nm), the size of HDP is much smaller than PSF. Therefore, the HDP physical size can be neglected and the size of fluorescence image

spots can be approximated as the PSF. From the fluorescence image spots fitting, the variance of the PSF at the peak emission wavelength of FD1 $\sigma_{\mathrm{PSF}}^{\mathrm{D}}$ can be obtained. The size of the microscopic PSF is directly related to the wavelength of excitation light λ via:

$$\epsilon = 0.61 \times \frac{\lambda}{NA}, \qquad \text{(A2-3)}$$

where NA is the numerical aperture of the objective lens. This means that the value of $\sigma_{\mathrm{PSF}}^{\mathrm{D}}$ obtained from the fluorescence (down-conversion emission) fitting cannot be used as σ_{PSF} in the equation (A2-2) because the spectral region of the UC emission and of fluorescence are different. Considering the equation (A2-3), the following relationship between $\sigma_{\mathrm{PSF}}^{\mathrm{D}}$ and σ_{PSF} was used to correct for the different wavelengths

$$\sigma_{\mathrm{PSF}} = \frac{\lambda_{\mathrm{UC}}}{\lambda_{\mathrm{D}}} \sigma_{\mathrm{PSF}}^{\mathrm{D}}, \qquad \text{(A2-4)}$$

where λ_{UC} is the UC emission peak wavelength and λ_{D} is the FD1 fluorescence peak wavelength. These values were determined from the Fig. A2-2. For the AC acceptor, λ_{UC} and λ_{D} were 438 nm and 625 nm, respectively, for the DPA acceptor these values were 444 nm and 626 nm, respectively.

Analysis of the lifetime measurements

Analysis of the UC emission decay shown Fig. 2-13 was done with multi-exponential fitting resulting in average τ_{UC} of 7.4×10^{-5} s and 1.8×10^{-4} s for the AC and DPA, respectively. With average values of τ_{UC}, the L_{t} in polycrystalline AC film and DPA film were calculated as 50 nm and 4.9 nm, respectively. However, in literature the longest decay time component is often used to estimate the L_{t}. The longest decay time components estimated from the multi-exponential fitting were 8.3×10^{-5} s and 2.2×10^{-4} s for the AC and DPA, respectively. With the longest decay time component of τ_{UC},

the L_t of AC and DPA were calculated as 47 nm and 4.4 nm, respectively. Although these values were slightly shorter than those estimated using the average τ_{UC}, the order of the L_t is well comparable.

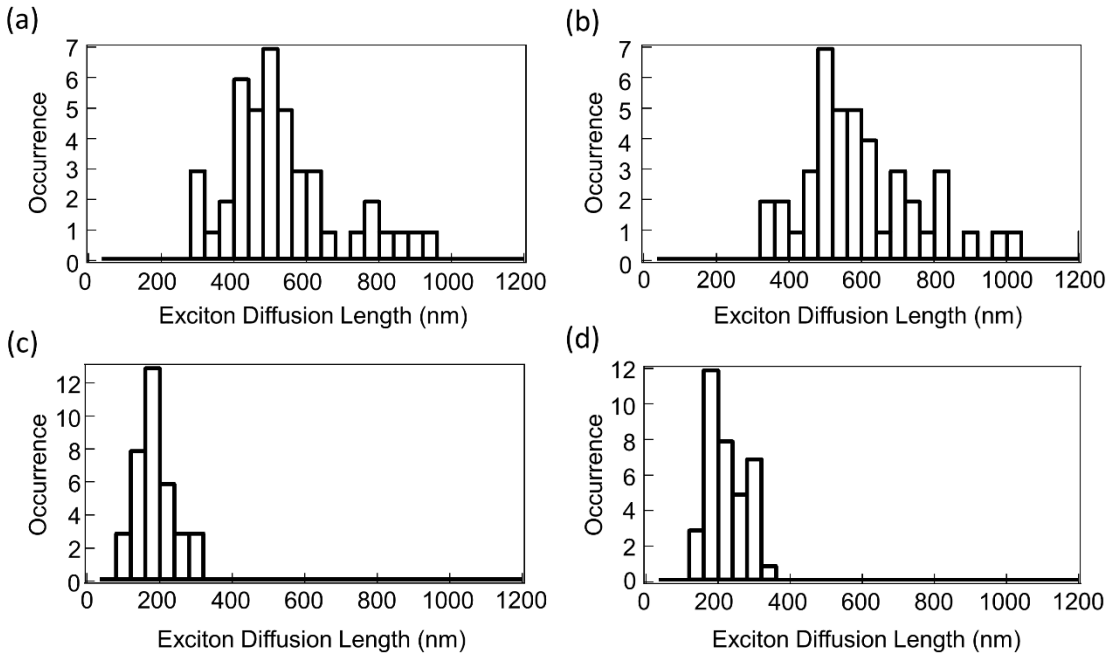

Figure A2-1. Histograms of L_t along two orthogonal axis for AC (a,b) and DPA (c,d). Histograms in (a) or (c) represent smaller values. Histograms in (b) or (d) represent larger values. Reprinted from ref. [28].

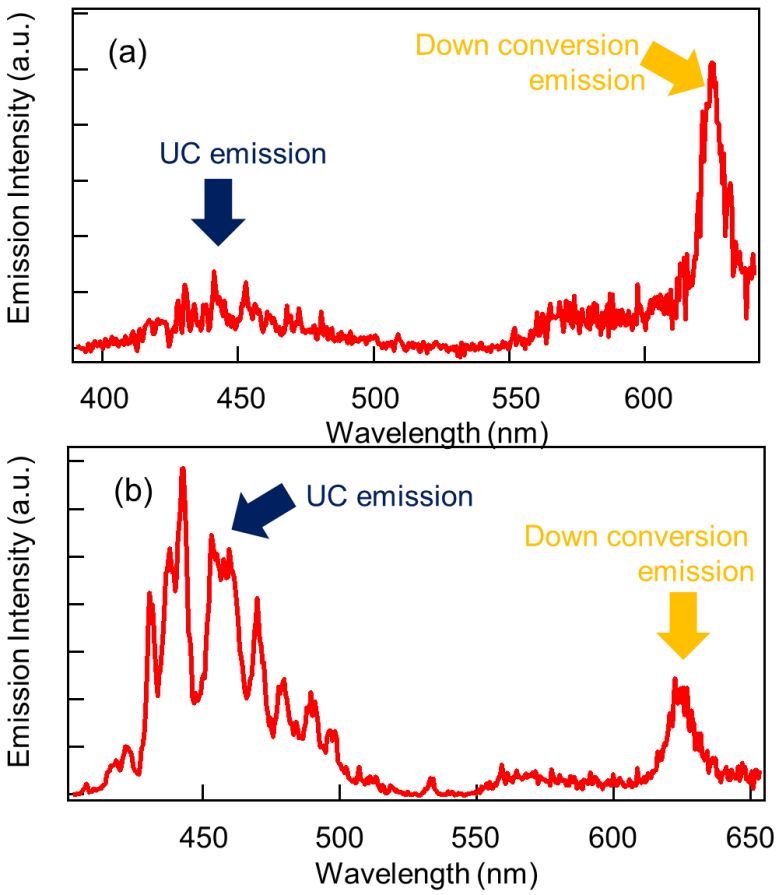

Figure A2-2. Emission spectrum of (a) AC at the point of a single HDP and (b) DPA at the point of a single HDP. In this experiment, image splitter was not used. Reprinted from ref. [28].

Chapter 2 References

1. T. N. Singh-Rachford, F. N. Castellano, *Coord. Chem. Rev.* **2010**, *254*, 2560.
2. W. Zou, C. Visser, J. A. Maduro, M. S. Pshenichnikov, J. C. Hummelen, *Nat. Photonics* **2012**, *6*, 560.
3. S. Baluschev, K. Katta, Y. Avlasevicha, K. Landfester, *Mater. Horiz.* **2016**, *3*, 478.
4. F. Wang, Y. Han, C. S. Lim, Y. Lu, J. Wang, J. Xu, H. Chen, C. Zhang, M. Hong, X. Liu, *Nature* **2010**, *463*, 1061.
5. S. Baluschev, T. Miteva, V. Yakutkin, G. Nelles, A. Yasuda, G. Wegner, *Phys. Rev. Lett.* **2006**, *97*, 143903.
6. Y. Murakami, Chem. Phys. Lett. **2011**, *516*, 56.
7. P. Duan, N. Yanai, H. Nagatomi, N. Kimizuka, *J. Am. Chem. Soc.* **2015**, *137*, 1887.
8. Y. Murakami, Y. Himuro, T. Ito, R. Morita, K. Niimi, N. Kiyoyanagi, *J. Phys. Chem. B* **2016**, *120*, 748.
9. V. Jankus, E. W. Snedden, D. W. Bright, L. V. Whittle, J. A. G. Williams, A. Monkman, *Adv. Funct. Mater.* **2013**, *23*, 384.
10. M. Wu, D. N. Congreve, M. W. B. Wilson, J. Jean, N. Geva, M. Welborn, T. Van Voorhis, V. Bulovic, M. G. Bawendi, M. A. Baldo, *Nat. Photonics* **2015**, *10*, 31.
11. Y. Y. Cheng, B. Fückel, R. W. MacQueen, T. Khoury, R. G. C. R. Clady, T. F. Schulze, N. J. Ekins Daukes, M. J. Crossley, B. Stannowski, K. Lips, T. W. Schmidt, *Energy Environ. Sci.* **2012**, *5*, 6953.
12. Z. Zhang, W. Wang, W. Yin, M. Shang, L. Wang, S. Sun, *Appl. Catal. B*, **2010**, *101*, 68.
13. F. Wang, D. Banerjee, Y. Liu, X. Chen, X. Liu, *Analyst* **2010**, *135*, 1839.
14. A. Monguzzi, J. Mezyk, F. Scotognella, R. Tubino, F. Meinardi, *Phys. Rev. B*:

Condens. *Matter*, **2008**, *78*,195112.

15. N. Yanai, N. Kimizuka, *Chem*. *Commun*. **2016**, *52*, 5354.
16. K. Kamada, Y. Sakagami, T. Mizokuro, Y. Fujiwara, K. Kobayashi, K. Narushima, S. Hirata, M. Vacha, *Mater*. *Horiz*. **2017**, *4*, 83.
17. J. Jortner, S. Choi, J. L. Katz, S. A. Rice, *Phys*. *Rev*. *Lett*. **1963**, *11*, 323.
18. G. M. Akselrod, P. B. Deotare, N. J. Thompson, J. Lee, W. A. Tisdale, M. A. Baldo, V. M. Menon, V. Bulović, *Nat*. *Commun*. **2014**, *5*, 3646.
19. Y. Wan, Z. Guo, T. Zhu, S. Yan, J. Johnson, L. Huang, *Nat*. *Chem*. **2015**, *7*, 785.
20. P. Irkhin, I. Biaggio, *Phys*. *Rev*. *Lett*. **2011**, *107*, 017402.
21. A. K. Bansal, W. Holzer, A. Penzkofer, T. Tsuboi, *Chem*. *Phys*. **2006**, *330*, 118.
22. D. Eastwood, M. Gouterman, *Mol*. *Spectrosc*. **1970**, *35*, 359.
23. P. Avakian, R. E. Merrifield, *Phys*. *Rev*. *Lett*. **1964**, *13*, 541.
24. P. Avakian, R. E. Merrifield, *Phys*. *Rev*. **1966**, *148*, 862.
25. R. R. Islangulov, D. V. Kozlov, F. N. Castellano, *Chem*. *Commun*. **2005**, *1*, 3776.
26. Y. Murakami, H. Kikuchi, A. Kawai, *J*. *Phys*. *Chem*. *B* **2013**, *117*, 5180.
27. P. Duan, D. Asthana, T. Nakashima, T. Kawai, N. Yanai, N. Kimizuka, *Faraday Discuss*. **2017**, *196*, 305.
28. K. Narushima, S. Hirata, M. Vacha, *Nanoscale* **2017**, *9*. 10653.

Chapter 3: Triplet Exciton Diffusion in Conjugated Polymer Nanofibers

3-1 Introduction

3-1-1 Exciton diffusion in conjugated polymers

Conjugated polymers are expected to be potentially useful for application for opto-electronic devices such as organic solar cells or OLEDs due to their prominent photophysical properties.[1-5] With the aim of applying conjugated polymers to next-generation devices, extensive studies have been reported so far. As mentioned in chapter 1, one of the most important factors that determines the characteristics of opto-electronic devices is triplet exciton diffusion. For example, in the case of organic solar cells, generated singlet or triplet excitons diffuse into the interface region between the acceptor and donor materials and undergo charge separation.[6] Thus, long singlet or triplet exciton diffusion length is preferred for excitons to reach the interfaces. However, singlet exciton diffusion in conjugated polymer films is generally on the order of 10 nm due to short singlet lifetime, randomly oriented polymer chain and energetic disorder.[6] This short singlet diffusion length prevents singlet excitons from reaching the interfaces. Consequently, the formation of bulk hetero-junction has been widely used to shorten the distance between donor and acceptor materials.[4] When longer exciton diffusion length is realized, the efficiency of solar cells can be improved.

As a solution to improve the efficiency, singlet exciton diffusion in oriented conjugated polymers has been proposed. Compared with randomly oriented conjugated polymer films, long singlet exciton diffusion length is expected due to its orientation. For example,

Vogelsang *et al*. studied singlet energy transport in highly ordered single conjugated polymer aggregate prepared by solvent vapor annealing[7]. In such a highly ordered conjugated polymer aggregates, the maximum value of singlet exciton diffusion length is 70 nm. This value is much longer than that in films, thus, long singlet exciton transport can be realized by orienting the polymer chains. In addition, recently, ultralong singlet exciton diffusion length has been realized by forming nanofibers.[8,9] One of the best ways to orient conjugated polymer chains and enhance exciton diffusion length is the use of nanofibers. Haedler *et al*. fabricated supramolecular (non-polymer) nanofibers and revealed that singlet exciton diffusion length in such supramolecular nanofiber was up to 4.4 μm.[8] This extreme diffusion length was due to the induced molecular orientation which lead to formation of H-aggregates and coherent exciton transport (Fig. 3-1). In the case of conjugated polymers nanofibers, Jin *et al*. prepared nanofibers by self-assembly method and singlet exciton diffusion length was > 200 nm due to the induced interchain π-π stacking induced by the formation of the nanofibers.[9] This estimated value is comparable with aromatic single crystals, which means that long singlet exciton diffusion length in conjugated polymers can be realized by formation of nanofibers. Therefore, the above results show nanofibers have strong potential as well-ordered conjugated polymer materials.

The use of triplet excitons is also considered as an effective solution to improve exciton diffusion length. As mentioned in chapter 1, the value of L_t has no theoretical limitation and ultralong L_t on the order of tens of micrometers can be realized due to the long τ_t.[10,11] For instance, L_t in Poly[(9,9-di-*n*-octylfluorenyl-2,7-diyl)-*alt*-(benzo[2,1,3]thiadiazol-4,8-diyl)] (F8BT) is 180 nm while singlet exciton diffusion length in the same material is only 8 nm.[6,12,13] Therefore, utilization of triplet exciton is efficient strategy for obtaining

long energy migration.

As described above, the use of nanofibers and triplet excitons are useful in order to enhance exciton diffusion length. Hence, the combination of triplet excitons and nanofibers is also considered as useful strategy for improving exciton diffusion length. However, triplet exciton diffusion in conjugated polymer nanofibers has not been measured so far and understanding of the behavior of triplet excitons in nanofibers is necessary in order to realize highly efficient opto-electronic devices.

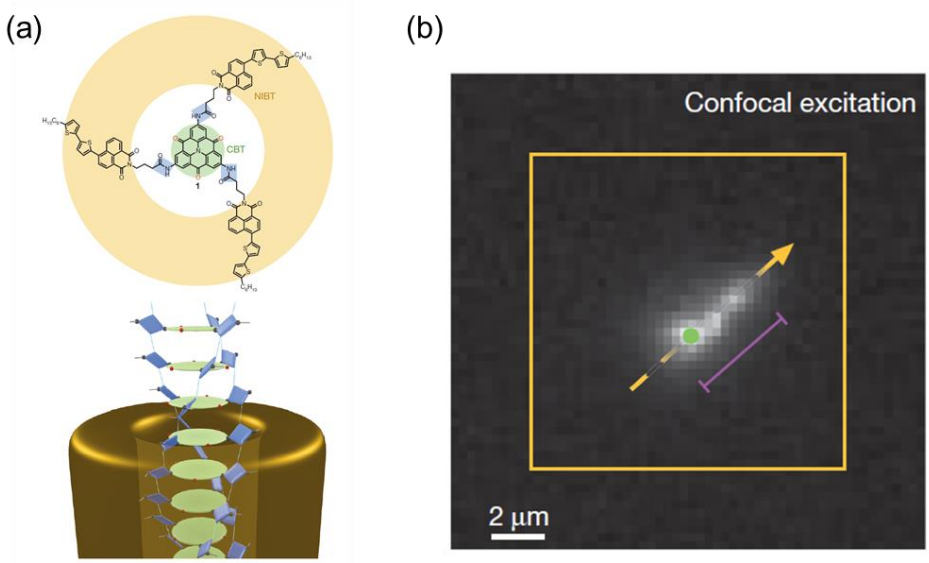

Figure 3-1. (a) Structure of the nanofiber used in ref. [8] (reprinted from ref. [8] with permission). (b) Emission image of the nanofiber with confocal excitation. The green spot represents the position of the confocal excitation. The emission can be observed from the opposite edge of the excitation, indicating that ultralong exciton diffusion occurs. Reprinted from ref. [8] with permission.

3-1-2 Fabrication of conjugated polymer nanofibers

One of the methods to fabricate polymer nanofibers is electrospinning. The concept of electrospinning is shown in Fig. 3-2a. High voltage is applied into polymer solution and

this charged polymer solution is sprayed onto a substrate connected to an electrode. Then, as the solution flow becomes fine, electrostatic repulsion becomes stronger leading to formation of further stretched solution flow and volatilization of solvent on the substrate. As a result, nanofibers are fabricated on the substrates.

A variety of conjugated polymer nanofibers can be fabricated by electrospinning.[14,15] The photoluminescence of these conjugated polymer is strongly dependent on polarization. Kuo *et al*. fabricated nanofibers blended with poly (methyl methacrylate) and the poly{[9,9-di(3,30-N,N0-trimethylammonium) propylfluorenyl-2,7-diyl]-alt-(9,9-dioctylfluorenyl-2,7-diyl)} diiodide salt and reported polarized photoluminescence from nanofibers (Fig. 3-2b).[14] This implies that main chains of conjugated polymer are well oriented along the nanofibers direction. Therefore, the electrospinning method is suitable for fabrication of well oriented conjugated polymer nanofibers.

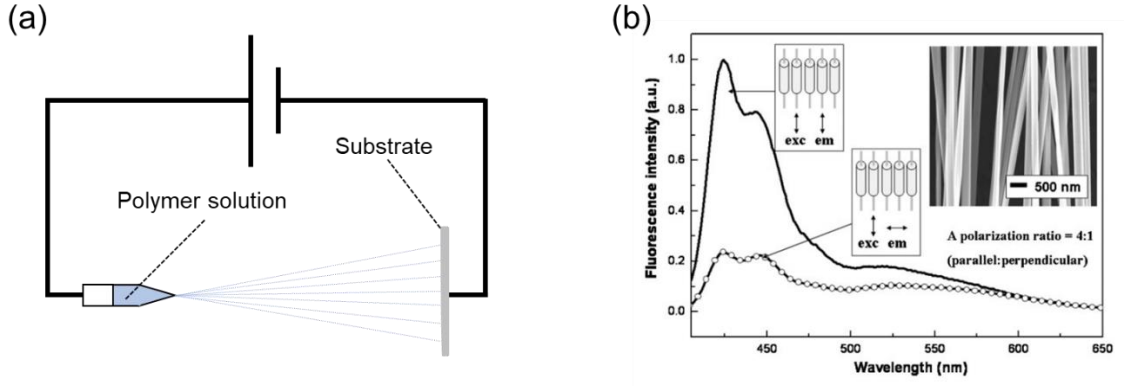

Figure 3-2. (a) Schematic illustration of electrospinning technique. (b) Linear dichroism of emission from fabricated conjugated polymer nanofibers reported in ref. [14]. Strong emission can be observed when the polarization of detected emission is parallel to the direction of conjugated polymer nanofibers. Reprinted from ref. [14] with permission.

3-1-3 Purpose

Improvement of L_t is important to realize efficient opto-electronic devices and triplet exciton diffusion in conjugated polymer nanofibers is expected to be one of the best solutions. However, triplet exciton diffusion in oriented conjugated polymers has not been measured so far. Therefore, it is necessary to study the effect of polymer chain orientation on the extent of L_t in the nanofibers. In this chapter, triplet exciton diffusion in conjugated polymer nanofibers is reported.

3-2 Experimental

3-2-1 Method for measurement L_t and sample selection

In the present experiment, L_t in conjugated polymer nanofibers were measured by measuring the threshold of UC emission. Since other methods such as method 1-6 described in chapter 1 require device configurations, precise layer thickness or sufficiently high photostability to ensure pump photoexcitation, these methods are difficult to apply into nanofibers. The method 7 (direct visualization) is possibly difficult since L_t in conjugated polymers which has been measured so far is often shorter than diffraction limited size leading to the difficulty in extracting L_t by optical microscope. On the other hand, measuring UC threshold is straightforward because such measurement is associated with no difficulties in preparing the samples and this method can be used to measure L_t shorter than the diffraction limited size. The efficiency of ISC in metal-free conjugated polymers is generally not high and triplet sensitizer is required to populate triplet excitons of the conjugated polymers. Therefore, a small amount of triplet sensitizer was dispersed in conjugated nanofibers to populate triplet excitons in this experiment.

There are a few reports related to TTA-based UC materials composed of conjugated

polymers.[16,17] Jankus *et al*. reported one such examples of TTA-based UC materials composed of polyphenylene vinylene copolymer (super yellow) and palladium (*meso* - tetraphenyl-tetrabenzoporphyrin) (PdTPBP).[16] Therefore, in this experiment, super yellow and PdTPBP were selected as conjugated polymer emitter and sensitizer, respectively. The chemical structures of super yellow and PdTPBP are shown in Fig. 3-3.

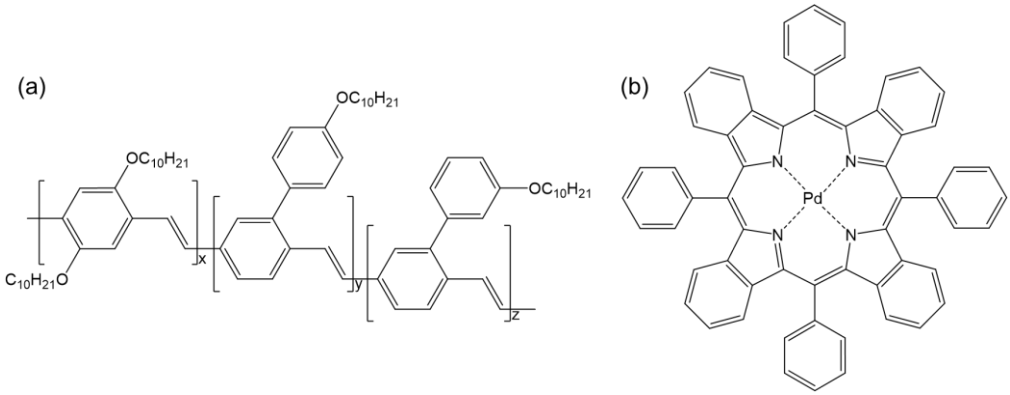

Figure 3-3. Chemical structures of (a) super yellow and (b) PdTPBP.

3-2-2 Sample preparation

In this experiment, nanofibers of super yellow (Sigma-Aldrich) doped with 4 wt% of PdTPBP (Chemodex) were fabricated by electrospinning. As a reference, spin-coated films of the same super yellow polymer doped with 4 wt% PdTPBP were prepared as non-oriented sample.

For fabrication of nanofibers, super yellow was dissolved in chloroform solution at the concentration of 0.05 wt%. PdTPBP was also dispersed in chloroform solution and this solution was mixed into prepared super yellow solution to obtain 4 wt% PdTPBP mass to mass ratio in fabricated nanofibers. Then, super yellow solution doped with PdTPBP was

filled into the syringe. The diameter of the needle of syringe was 0.31 mm and the flow rate of super yellow solution was 0.3 ml/h. The distance between the tip of the syringe and cleaned glass substrate was 15 cm. The applied voltage to the syringe and the glass substrate was +15 kV and -1 kV, respectively. The glass substrate was sprayed for about 30 s. On the other hand, for preparation of spin-coated film, super yellow was dissolved in toluene solution at the concentration of 0.2 wt%. After that, PdTPBP was also dispersed in toluene solution and this solution was mixed into super yellow solution to get 4 wt% PdTPBP mass to mass ratio. Then, this solution was spin-coated on the cleaned glass substrate (30s, 3000 rpm).

Absorption spectra and emission spectra in toluene solution were measured using a standard UV-visible/NIR spectrophotometer (V-760, Jasco) and a real-time multichannel spectrometer (PMA-12 C10027-01, Hamamatsu Photonics), respectively.

The UC threshold was measured with an inverted fluorescence microscope (IX 71, Olympus). The excitation was a continuous wave laser (ASITALASER) at 635 nm. The UC emission from super yellow was collected by an oil immersion lens (×100 UPLSAPO, N.A. 1.3, Olympus) with dichroic mirror (600nm, 25.2 x 35.6mm, Dichroic Shortpass Filter, Edmund Optics). This collected UC emission was filtered by short pass filter (FES0600 Short Pass Filter, 600 nm cut off, Thorlabs) and imaged by an electron-multiplying (EM) CCD camera (iXon, Andor Technology).

3-2-3 Quantum chemical calculations

Quantum chemical calculations for transfer integral were performed using Amsterdam density functional (ADF2018) package. Transfer integral of electron transfer (hole transfer) $t_{et(ht)}$ was calculated using Hybrid-B3LYP functional and TZP Slater-type all-

electron basis sets.

3-3 Result and discussion

Fig. 3-4 shows the absorption and emission spectra of super yellow and PdTPBP in toluene solution. PdTPBP can be excited at 635 nm followed by efficient ISC. The triplet energy of PdTPBP is transferred to super yellow leading to generation of triplet excitons. After triplet exciton diffusion and TTA of super yellow, up-converted photons should be observed from 500-600 nm. As seen in Fig. 3-5, the UC emission from super yellow in THF solution excited at 635 nm was observed as expected.

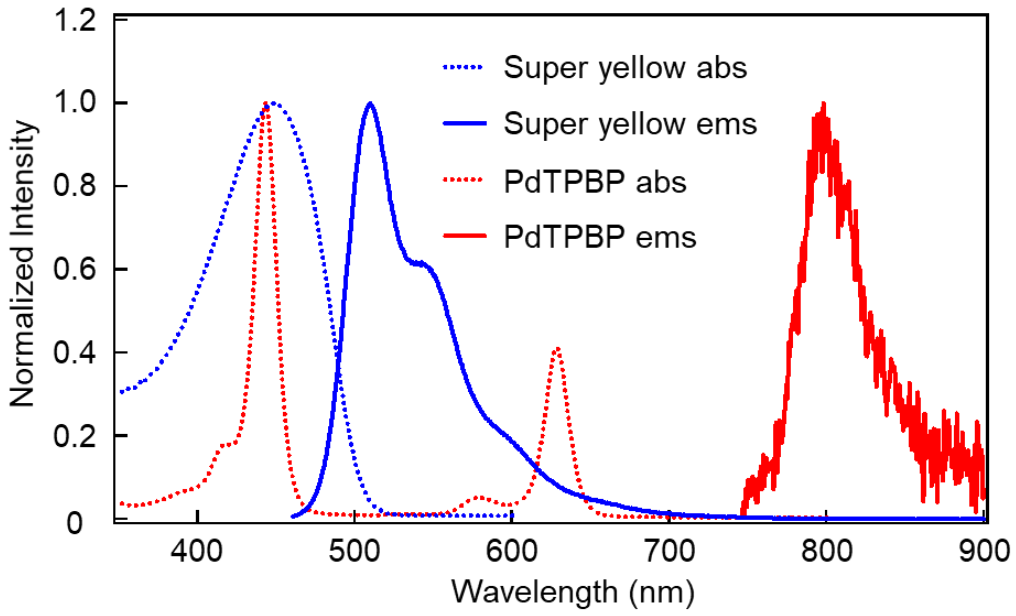

Figure 3-4. Absorption and emission spectra of super yellow and PdTPBP in toluene.

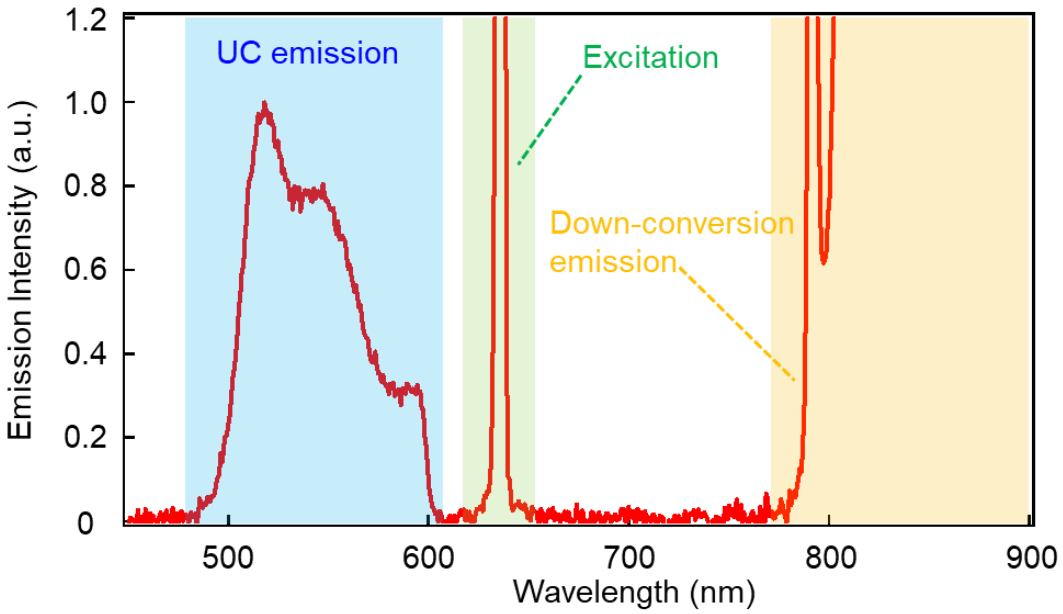

Figure 3-5. UC emission from super yellow in toluene excited at 635 nm.

3-3-1 Characteristics of the fabricated nanofibers

Fig. 3-6 shows SEM image of the fabricated fibers. The samples contain not only fibers but also larger aggregated structures. This indicates that super yellow is somewhat likely to form aggregates under the present condition. In the following experiments, the amount of sample deposited on a microscopic substrate was reduced in order to obtain isolated and well spatially separated nanofibers that could be measured individually using an optical microscope.

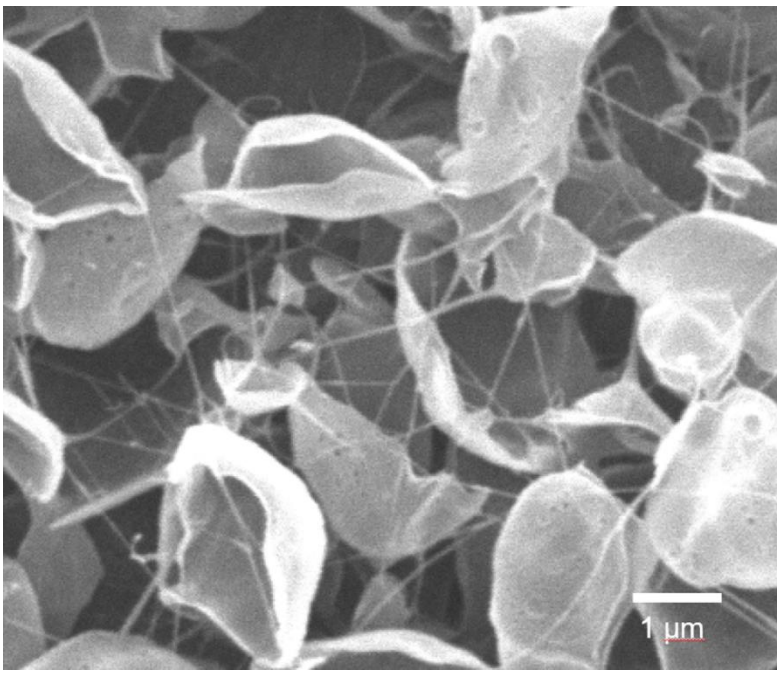

Figure 3-6. SEM image of a sample fabricated by electrospinning.

Fig. 3-7 shows fluorescence images of fabricated super yellow fibers. As shown in Fig. 3-7, super yellow fibers can be confirmed in the image. However, aggregates of super yellow were also observed (Fig. 3-7). In this experiment, we measured and analyzed only the regions of well-formed fibers in order to avoid the contribution of aggregates. Thus, we discuss photophysical properties of only the fiber regions in the following section. Fig. 3-8 shows atomic force microscope (AFM) images of fibers. In the AFM images, the width and height of the nanofibers are estimated about 100 nm and 10 nm, respectively, confirming that super yellow fibers are on nanoscale order (nanofibers).

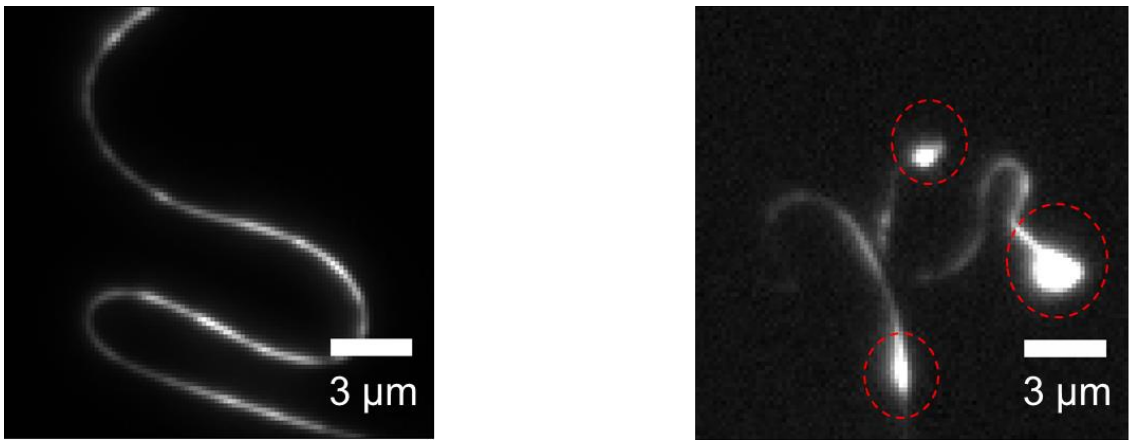

Figure 3-7. Fluorescence image of the fabricated nanofibers. The strong fluorescent spots (surrounded by red circles) were sometimes observed, indicating the formation of aggregates.

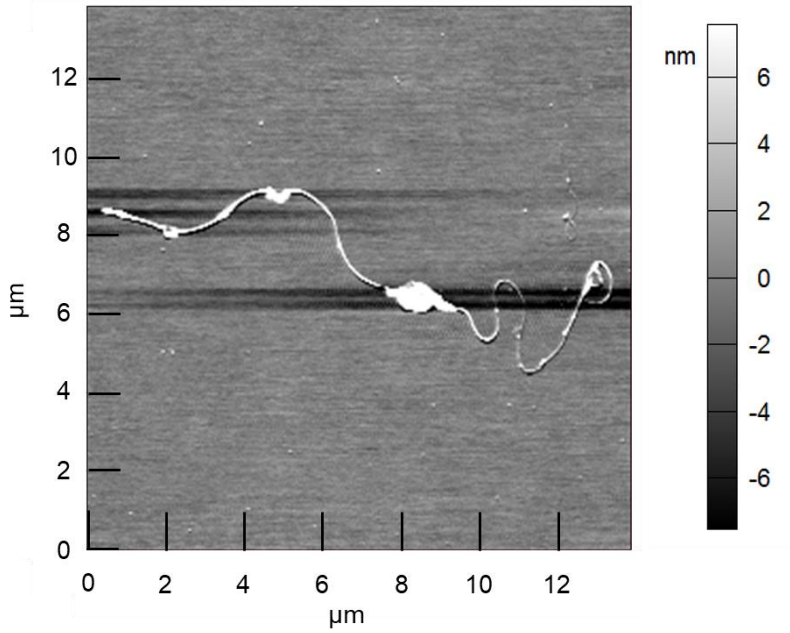

Figure 3-8. AFM image of a single conjugated polymer nanofiber.

In order to estimate the degree of orientation in nanofibers, linear dichroism of absorption was measured. In this measurement, excitation light was circulated polarized and a polarizer was put between the fluorescence microscope and the wave plate. In such configuration, samples can be excited by linearly polarized light. As the polarizer is

rotated, the direction of linearly polarized excitation light is changed and linear dichroism of absorption monitored in fluorescence can be measured. In the case of spin-coated film, the fluorescence intensity is not affected by rotation of polarizer because polymer chains in film are not oriented and isotropic (Fig. 3-9). On the other hand, as the polarizer on the excitation side was rotated, the fluorescence intensity from the nanofibers is modulated (Fig. 3-10). This modulation obviously results from anisotropic absorption due to orientation of super yellow polymer chains in the nanofibers. The maximum to minimum ratio of fluorescence intensity is about 10, which means polymer chains are highly oriented in the nanofibers (Fig. 3-10).

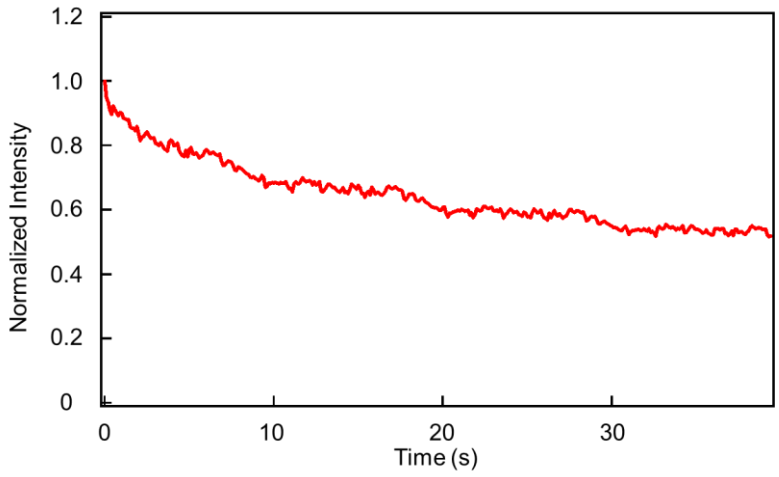

Figure 3-9. Dependence of emission intensity from spin-coated film on the excitation polarization. The polarizer used in this experiment rotated once in about 10 s.

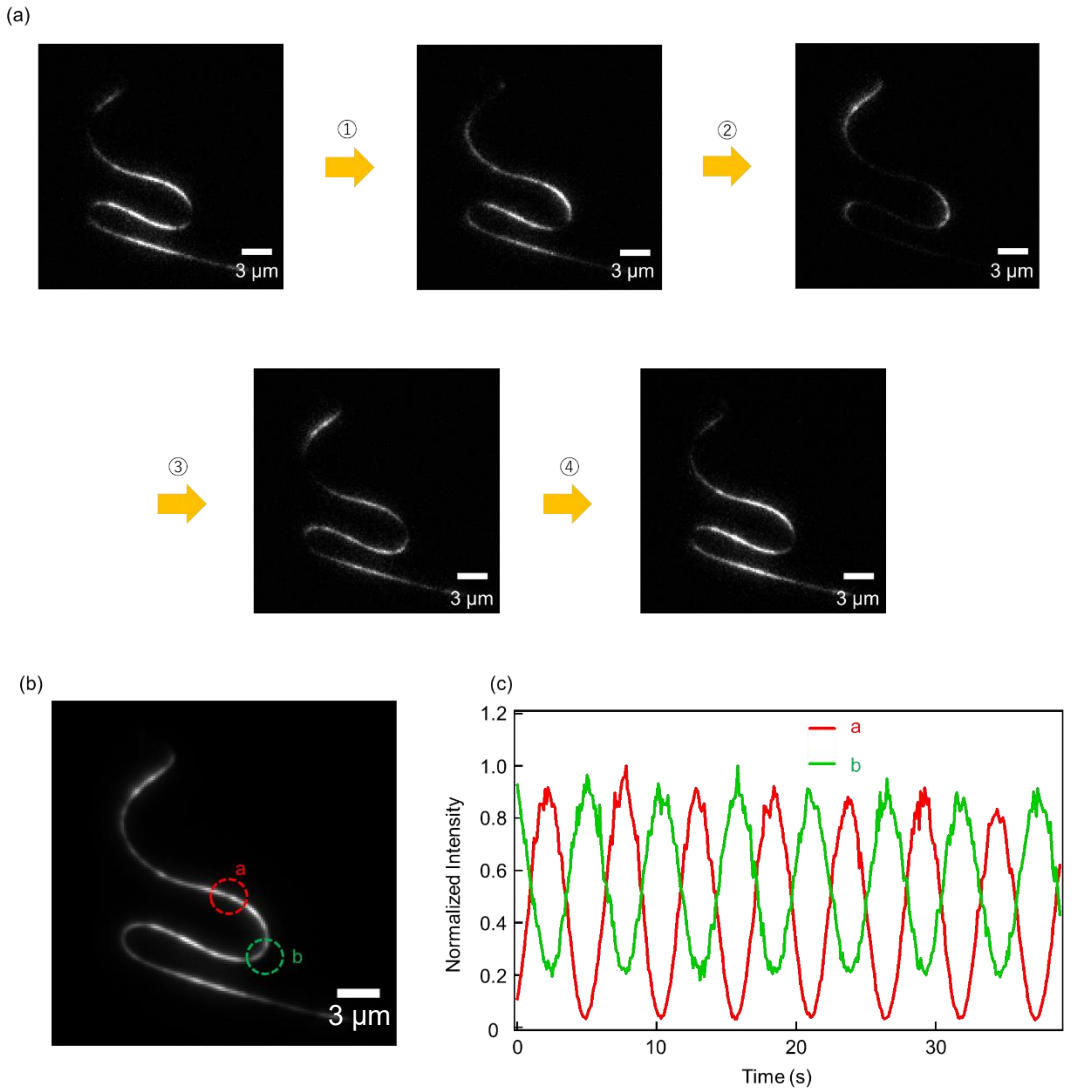

Figure 3-10. (a) Fluorescence images of a single nanofiber during one rotation of the polarizer. As the polarizer is rotated, the fluorescence image was modulated. (b) Two spots used for time tracing measurement. (c) Time tracing of fluorescent intensity at the spots indicated in (b). The polarizer used in this experiment was rotated once in about 10 s.

3-3-2 Estimation of triplet exciton diffusion in nanofibers

In order to estimate triplet exciton diffusion length in the nanofibers, the dependence of UC emission intensity on excitation intensity was measured and the value of UC threshold was evaluated. The intensity of UC emission from a single spot on a nanofiber was measured and analyzed using a fluorescence microscope. Fig. 3-11a and b shows the

dependence of UC emission intensity on excitation intensity in spin-coated film and in single nanofiber, respectively. As mentioned in chapter 2, the UC threshold is determined from the intersection of two linear fits. The estimated threshold of spin-coated film and single nanofiber were 1.1×10^4 mWcm^{-2} and 3.6×10^3 mWcm^{-2}, respectively. The evaluated UC threshold is determined by many parameters, such as Φ_{et}, α, a, τ_t and D_t as seen in equation (2-4). In this experiment, we assumed that all parameters except for D_t are same in the two prepared samples (nanofibers and spin-coated film). This assumption is considered appropriate since such parameters are independent on morphology of the conjugated polymer chains. Thus, the difference of the value of UC threshold implies the difference of D_t indirectly. The value of UC threshold in single super yellow nanofiber is 3.2 times lower than that in spin-coated film. This means D_t in single nanofiber is 3.2 times larger than that in spin-coated film since D_t is inversely proportional to UC threshold, as shown in equation (2-4).

Next, L_t in nanofibers are estimated. Rand *et al*. reported L_t in film of super yellow by measuring photocurrent in the device composed of super yellow and the estimated L_t in film was 9 nm.[18] Thus, in the present case, L_t of prepared spin-coated film is also considered as 9 nm. Consequently, considering that D_t in super yellow nanofibers is 3.2 times larger than that in films and that L_t is proportional to the square root of D_t, L_t in nanofibers can be estimated as 16 nm. Our result implies that the extended L_t can be obtained with the use of conjugated polymer nanofibers. This means conjugated polymer nanofibers are potential organic molecular materials for opt-electronic devices.

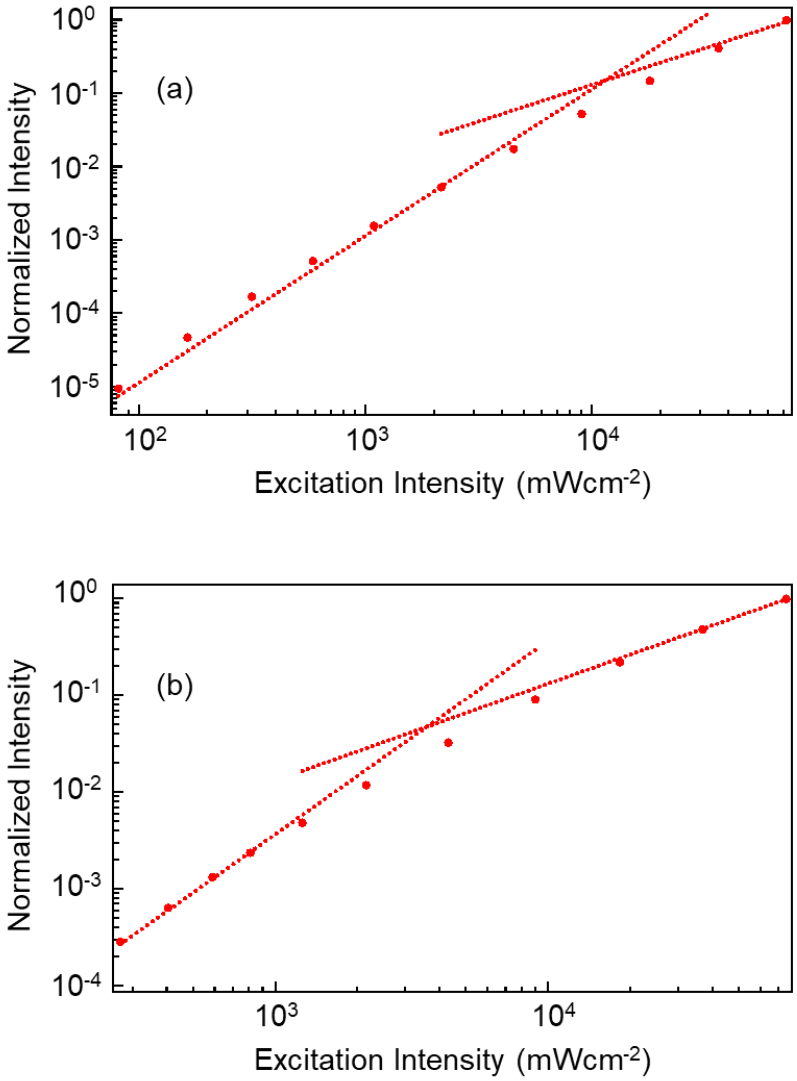

Figure 3-11. Dependence of UC emission intensity on excitation intensity of (a) spin-coated film and (b) a single nanofiber.

In order to discuss the different obtained values of L_t, quantum chemical calculations were performed. Triplet exciton diffusion that is based on Dexter-type energy transfer requires molecular orbital overlap. The degree of the overlap is related to a transfer integral, which was calculated here for model systems. As the simplest model that describes the conformational motifs of a conjugated polymer chain (super yellow) oriented in a nanofiber or dispersed randomly in a spin-coated film we used trans type or

cis type configuration of the conjugated bond between two monomer units. In an extended state (such as in the nanofiber), neighboring segments in the conjugated polymer chain are straight (connected in a trans-like type configuration). On the other hand, in the case of spin-coated film, the conjugated polymer chains are oriented randomly, which implies the presence of both cis and trans type configurations. Here, for the sake of simple qualitative explanation, only phenyl segments in the super yellow structure were used for the calculation. After structure optimization in cis type or trans type configuration, orbital overlaps related to triplet energy transfer (namely, overlaps between HOMO and HOMO, and between LUMO and LUMO) were calculated. The calculated transfer integrals of the cis type configuration were $t_{\mathrm{ht}} = 37.8\ \mathrm{meV}$ and $t_{\mathrm{et}} = 7.8\ \mathrm{meV}$, respectively and those of the trans type configuration were $t_{\mathrm{ht}} = 0.5\ \mathrm{meV}$ and $t_{\mathrm{et}} = 34.7\ \mathrm{meV}$, respectively. This result shows that the degree of molecular orbital overlap and the resulting transfer integral are not dramatically different between the cis and trans type configurations. Therefore, the measured extent of the triplet diffusion length L_t is not determined by the molecular-level structure (and the resulting molecular orbital overlap) of the conjugated polymer chains.

The origin of the extended value of L_t in the nanofiber could be the decreased dimensionality of the 1D fiber structure. In the case of the nanofiber, triplet excitons are likely to diffuse along the polymer main chain (in 1D direction) which itself is oriented along the orientation of the nanofiber. On the other hand, in the case of spin-coated film, triplet excitons can diffuse three-dimensionally along the randomly orientated polymer chains. Therefore, the dimensionality is one of the advantages of the nanofiber structure leading to the extended value of L_t even though the difference of molecular orbital overlap between the nanofiber and the spin-coated film is not significant.

3-4 Summary

In this chapter, triplet exciton diffusion in oriented conjugated polymer nanofibers was discussed. Super yellow nanofibers were successfully fabricated by electrospinning and the orientation of conjugated polymers was confirmed from the measurement of linear dichroism. While direct microscopic visualization of the triplet exciton diffusion was not possible due to generally short diffusion lengths in conjugated polymers, the observed excitation intensity threshold I_{th} for upconversion emission in the nanofibers was significantly lower than that in a reference spin-coated film, implying that triplet exciton diffusion in the nanofiber was enhanced. Analyzing and comparing the value of I_{th} in the nanofiber and in the spin-coated film, the triplet diffusion length L_t in the super yellow nanofiber was determined as 16 nm. This study thus points to potential advantages in the use of conjugated polymer nanofibers in TTA-based upconversion devices and possibly in other opto-electronic applications.

Chapter 3 References

1. T. Nakamura, D. K. Sharma, S. Hirata, M. Vacha, *J. Phys. Chem. C*. **2018**, *122*, 8137.
2. D. Neher, *Macromol. Rapid Commun*. **2001**, *22*, 1365.
3. U. Scherf, E. J. W. List, *Adv. Mater*. **2002**, *14*, 477.
4. G. Yu, J. Gao, J. C. Hummelen, F. Wudl, A. J. Heeger, *Science* **1995**, *270*, 1789.
5. Y. Honmou, S. Hirata, H. Komiyama, J. Hiyoshi, S. Kawauchi, T. Iyoda, M. Vacha, *Nat. Commun*. **2014**, *5*, 4666.
6. Y. Tamai, H. Ohkita, H. Benten, S. Ito, *J. Phys, Chem. Lett*. **2015**, *6*, 3147.
7. J. Vogelsang, T. Adachi, J. Brazard, D. A. V. Bout, P. F. Barbara, *Nat. Mater*. **2011**, *10*, 942.
8. A. T. Haedler, K. Kreger, A. Issac, B. Wittmann, M. Kivala, N. Hammer, J. Köhler, H. W. Schmidt, R. Hildner, *Nature* **2015**, *523*, 196.
9. X.-H. Jin, M. B. Price, J. R. Finnegan, C. E. Boott, J. M. Richter, A. Rao, S. M. Menke, R. H. Friend, G. R. Whittell, I. Manners, *Science* **2018**, *360*, 897.
10. O. V. Mikhnenko, P. W. M. Blom, T.-Q. Nguyen, *Energy Environ. Sci.* **2015**, *8*, 1867.
11. P. Avakian, R. E. Merrifield, *Phys. Rev*. **1966**, *148*, 862.
12. B. H. Wallikewitz, D. Kabra, S. Gélinas, R. H. Friend, *Phys. Rev. B*: *Condens. Matter Mater. Phys*. **2012**, *85*, 045209.
13. O. V. Mikhnenko, M. Kuik, J. Lin, N. van der Kaap, T.-Q. Nguyen, P. W. M. Blom, *Adv. Mater*. **2014**, *26*, 1912.
14. C.-C. Kuo, C.-T. Wang, W.-C. Chen, *Macromol. Mater. Eng*. **2008**, *293*, 999.
15. A. P. Roque, L. A. Mercante, V. P. Scagion, J. E. Oliveira, L. H. C. Mattoso, L. D. Boni, C. R. Mendonca, D. S. Correa, *J. Polym. Sci. Part B: Polym. Phys*. **2014**, *52*, 1388.

16. V. Jankus, E. W. Snedden, D. W. Bright, L. V. Whittle, J. A. G. Williams, A. Monkman, *Adv*. *Funct*. *Mater*. **2013**, *23*, 384.
17. P. E. Keivanidis, S. Baluschev, T. Miteva, G. Nelles, U. Scherf, A. Yasuda, G. Wegner, *Adv*. *Mater*. **2003**, *15*, 2095.
18. B. P. Rand, S. Schols, D. Cheyns, H. Gommans, C. Girotto, J. Genoe, P. Heremans, J. Poortmans, *Org*. *Electron*. **2009**, *10*, 1015.

Chapter 4: Suppressed Triplet Exciton Diffusion as a Possible Factor for the Appearance of Persistent Room Temperature Phosphorescence

4-1 Introduction

4-1-1 Persistent room temperature phosphorescence

Understanding and controlling triplet excited state is crucial for improving the device performance of OLEDs,[1,2] for photodynamic therapy,[3] bioimaging,[4] and for TTA-based UC materials.[5] For instance, the recent great progress in the development of OLEDs can be especially attributed to the development of efficient room temperature phosphorescence (RTP) from heavy-metal complexes.[6] Unlike the efficient RTP from such complexes that is enhanced by the heavy-atom effect, the triplet radiative rate k_p of metal-free conjugated molecules is generally very small[7]. In addition, at room temperature (RT) under ambient conditions, the triplet nonradiative depopulation rate due to intramolecular vibrational relaxation k_{nr} and the triplet quenching rate due to the interaction with ambient surroundings k_q are much larger than the value of k_p. Therefore, the RTP from metal-free conjugated molecules in ambient surroundings had been considered difficult to observe for long time. However, in the past a few years, the RTP from metal-free aromatic molecules in ambient surroundings has been realized by suppressing k_{nr}+ k_q in organic molecular materials such as host-guest systems, carbon nanodots and heavy atom-free aromatic crystals.[8-14] Further, in some of these materials, ultralong-lived RTP (or persistent RTP) was reported.[10-14] The lifetime τ_t of such RTP is

on the order of a few seconds due to intrinsically very small k_p and due to simultaneous suppression of k_{nr}+ k_q. This means persistent RTP can be observed easily by a naked eye after ceasing the photoirradiation, as shown in Fig. 4-1. Such materials can be potentially applied in bioimaging, optical sensing and security because persistent RTP is independent of autofluorescence of the sample and can be experimentally measured with low-cost detectors due to the ultralong-lived nature of the RTP.[15-19]

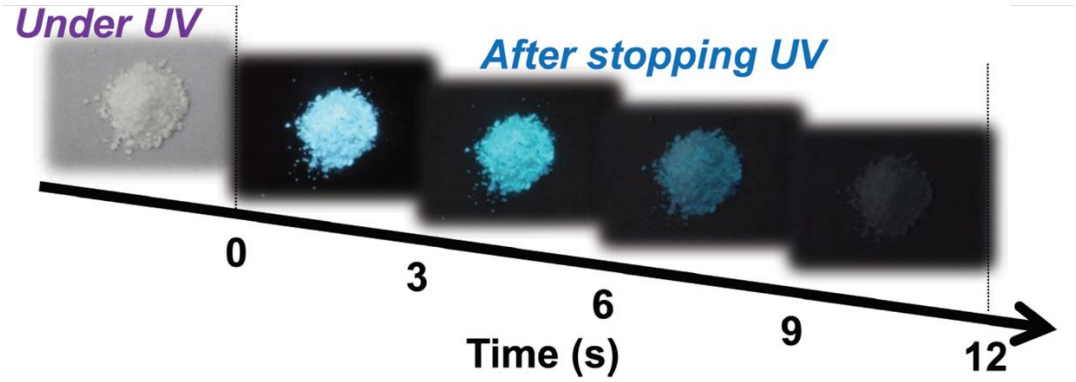

Figure 4-1. Persistent RTP reported in ref. [10]. After stopping photoexcitation, bright persistent RTP can be observed. Reprinted from ref. [10] with permission.

4-1-2 Current issues

In order to obtain efficient persistent RTP from heavy atom-free conjugated molecules, efficient ISC and suppressed k_{nr}+k_q are very important. It is known that efficient ISC in heavy atom-free conjugated molecules can be realized by molecular design based on symmetry rules or the El-Sayed rule.[20-22] On the other hand, the theory of suppression of k_{nr}+k_q is not sufficient and not completed. Hence, the elucidation of the suppression of k_{nr}+k_q is crucial for understanding the mechanism of the appearance of persistent RTP. However, the experimental separation of k_{nr}+k_q into k_{nr} and k_q is somewhat complicated,

resulting in the difficulty in analysis of suppressed k_{nr} and k_q.[25] In the case of host-guest systems, the separation of $k_{nr}(RT)+k_q(RT)$ can be realized by using very rigid host material with high T_1 energy.[10] In such host-guest materials, the thermally activated energy transfer from guest molecules to host matrix and the deactivation via quenching by oxygen are suppressed, resulting in the suppression of $k_{nr}+k_q$ and consequently the appearance of efficient persistent RTP. Very recently, it was revealed that the value of k_{nr} in such very rigid host materials was intrinsically comparable with that of k_p.[22] Therefore, the mechanism of the appearance of persistent RTP (the theory of suppression of $k_{nr}+k_q$) in host-guest systems is becoming clear.

On the order hand, in the case of persistent RTP from molecular aggregated states such as heavy atom-free conjugated molecular crystals, charge transfer (CT) characteristics have been considered important for persistent RTP because the CT kind of molecules are expected to induce strong and rigid intermolecular interactions in the crystals.[13,18,23,24] That said, some heavy atom-free conjugated molecular crystals without CT characteristics still show persistent RTP.[26,27] Hence, the molecular design for the persistent RTP from crystalline state has been somewhat phenomenological so far, and the mechanism of the appearance of persistent RTP from such crystalline state is not yet fully known. Particularly, the discussion of the origin of the suppression of $k_{nr}+k_q$ in crystalline state has not gone beyond the understanding that it is caused by the induced rigidity of the crystalline state. Therefore, unraveling of the mechanism of suppressed $k_{nr}+k_q$ is crucial and new photophysical approaches are required for obtaining persistent RTP from crystalline state. Now, for the following discussion, it should be noted that k_q is a rate of a process that results in complete triplet quenching at the defect sites inside the crystal or at the surface of the crystal. This means that k_q does not include triplet energy migration

from one site to neighboring one if the triplet energy is not quenched in the crystal as a result. Focusing on the k_q in aromatic crystals, triplet exciton diffusion is one of the factors that determine the value of k_q.[25] Triplet excitons with long L_t can reach defect sites in the crystal or at the crystal surface, followed by the triplet quenching, leading to a large value of k_q. Triplet excitons with short L_t do not reach the defect sites or the surface leading to small values of k_q. However, L_t in aromatic crystals showing persistent RTP has not been measured or considered so far, in spite of its possible large contribution to k_q. Therefore, the consideration of the relationship between L_t and k_q in such crystals is crucially important for deeper understanding of the mechanism of persistent RTP.

4-1-3 Purpose

The mechanism of the appearance of persistent RTP from crystalline materials has not been understood because the information of the suppressed $k_{nr}+k_q$ is lacking. In this chapter, the value of k_{nr} and k_q were measured. Further, the value of L_t was measured and its relationship to k_q was discussed.

4-2 Experimental

4-2-1 Sample preparation

In this experiment, two kinds of aromatic crystals, with and without persistent RTP, were prepared. 2-carbazolyl-4,6-dichloro-1,3,5-triazine (CzDClT) was used as aromatic crystals with persistent RTP while rubrene was used as reference crystal without persistent RTP. The chemical structures are shown in Fig. 4-2. CzDClT was synthesized as previously reported in ref. 13 and purified by recrystallization. Rubrene single crystals were grown by physical vapor transport under reduced pressure (ca. 10 Pa). Rubrene

powder (Tokyo Chemical Industry CO., LTD.) was sublimated in three-zone furnace. The temperature of the sublimation and deposition parts were set as 195ºC, 160ºC and 145ºC, respectively. The flow rate of nitrogen was 45 mL/min.

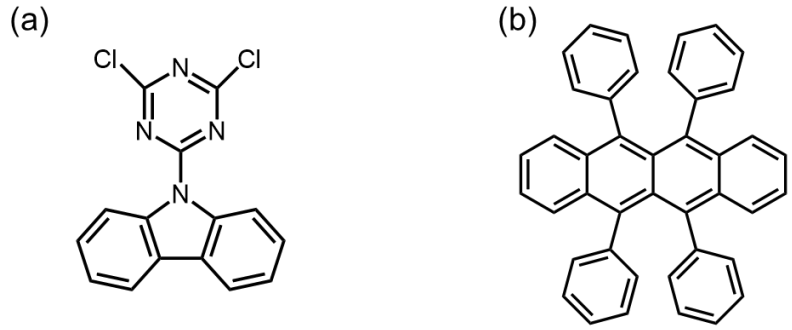

Figure 4-2. Chemical structures of (a) CzDClT and (b) rubrene.

4-2-2 Measurement methods

Emission spectra and $\tau_t(T)$ of CzDClT were measured with a photonic multichannel analyzer (PMA-12, Hamamatsu Photonics) and a cryostat (Optistat DN-V, Oxford Instruments). RTP spectra of CzDClT were measured by detecting the emission spectrum soon after ceasing photoexcitation. The quantum efficiency of fluorescence at RT Φ_f and the quantum efficiency of phosphorescence at RT Φ_p were determined using an absolute luminescence quantum yield measurement system (C9920-02G, Hamamatsu Photonics). X-ray measurement of CzDClT single crystal was performed using a Bruker SMART APEX II ULTRA/CCD diffractometer.

In this experiment, triplet exciton diffusion was visualized using an inverted fluorescence microscope (IX 71, Olympus). In the case of CzDClT single crystal, the excitation light was provided by a 360 nm cw laser (UV-FN-360, 100 mW, CNI). Emission from CzDClT single crystal was collected by an oil immersion lens (UplanFLN 100×, N. A. 1.3, Olympus) using a dichroic mirror (Dichro375) and a long pass filter

(LP377, Edmund) and detected using an electron-multiplying CCD camera (iXon, Andor Technology). In the case of rubrene single crystal, the excitation light was provided by a 442 nm cw laser (IK4301R-D, KIMMON KOHA), and the same optical setup was used except for using different dichroic mirror (Dichro488, Semrock) and long pass filter (LP515).

4-2-3 Quantum chemical calculations

Quantum chemical calculations for electron transfer rate or hole transfer rate were performed in order to understand the relationship between the estimated L_t and k_q. The calculations for electron transfer rate (hole transfer rate) at RT $k_{et(ht)}$ were performed using Amsterdam density functional (ADF2018) package. Transfer integral of electron transfer (hole transfer) $t_{et(ht)}$ was calculated using Hybrid-B3LYP functional and TZP Slater-type all-electron basis sets. Configuration of neutral monomer and radical anion (radical cation) of the monomer were optimized using Hybrid-B3LYP functional and TZP basis sets to determine the reorganization energy of electron transfer (hole transfer) $\lambda_{et(ht)}$.

4-3 Result and discussion

Fig. 4-3a and b show emission spectra and phosphorescence decay of CzDClT crystals, respectively. At room temperature under ambient conditions, the value of τ_t was 0.61 s.

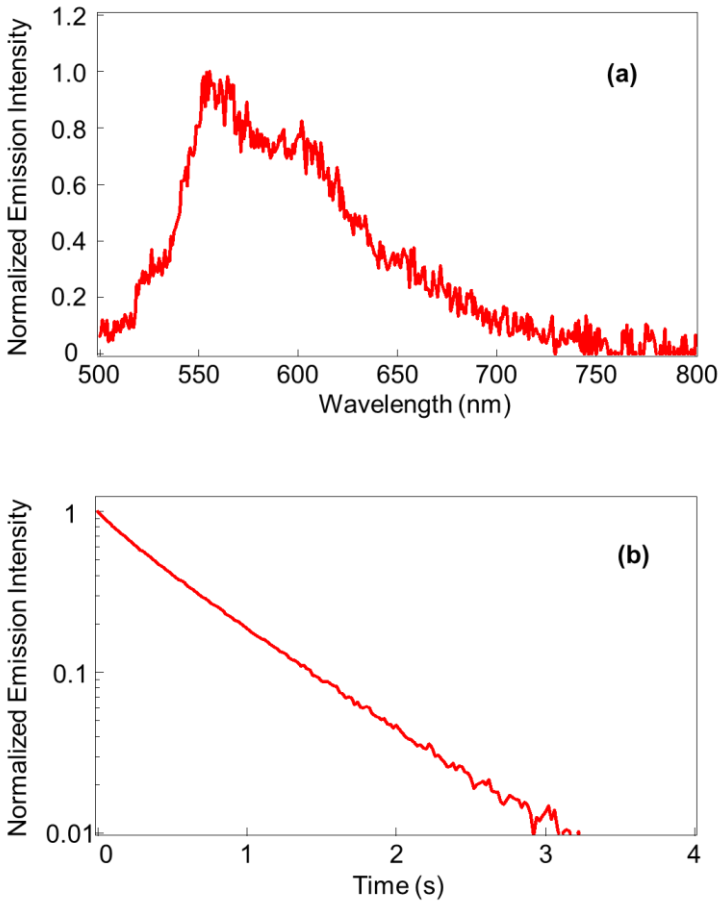

Figure 4-3. (a) Spectrum of persistent RTP from CzDClT crystal. (b) Decay of persistent RTP from CzDClT crystal. Reprinted from ref. [39].

4-3-1 Estimation of the value of k_{nr} and k_q

In order to estimate the value of k_{nr} and k_q, the separation of k_{nr}+k_q was carried out by measuring temperature dependence of $k_{nr}(T)$+$k_q(T)$. This separation enabled the estimation of the individual values of k_{nr} and k_q. To determine the temperature dependence of $k_{nr}(T)$+$k_q(T)$, temperature dependence of $\tau_t(T)$, quantum efficiency of ISC at RT Φ_{isc}, Φ_f and Φ_p are required. Generally, the measurement of Φ_{isc} in crystalline materials is difficult. Therefore, Φ_{isc} was approximated as $\Phi_{isc} \sim 1\text{-}\Phi_f$. This approximation is valid when conjugated a molecule has a rigid planar structure and its S_1 excitation energy is

above 2.7 eV without conical intersections.[7] In the case of CzDClT, this approximation can be used in crystalline state although it is not appropriate in solution due to the twisted molecular structure (see the appendix for the details). Using the value of measured Φ_p and calculated Φ_{isc}, the value of k_p was determined as 5.1×10^{-2} s^{-1}. Then, temperature dependence of $k_{nr}(T)+k_q(T)$ was estimated by subtracting the calculated k_p from the reciprocal of $\tau_t(T)$ (Fig. 4-4). As shown in Fig. 4-4, temperature dependence of $k_{nr}(T)+k_q(T)$ has an Arrhenius-like character and can be fitted with a sum of two exponential functions. Such behavior has been reported before for host-guest systems.[10] In the previous reports, the value of $k_{nr}(T)$ was dominant at lower temperature. On the other hand, as temperature increases, the value of $k_q(T)$ starts dominating due to a temperature dependent triplet energy transfer from guest molecules to host molecules. In the case of CzDClT crystals, we assumed that $k_{nr}(T)+k_q(T)$ can be separated into $k_{nr}(T)$ and $k_q(T)$ in the same manner as in ref. 10, and estimated $k_{nr}(T)$ at RT and k_q at RT as 1.2×10^{0} s^{-1} and 3.9×10^{-1} s^{-1}, respectively. The estimated value of k_q is very small in the CzDClT crystal, leading to the appearance of persistent RTP.

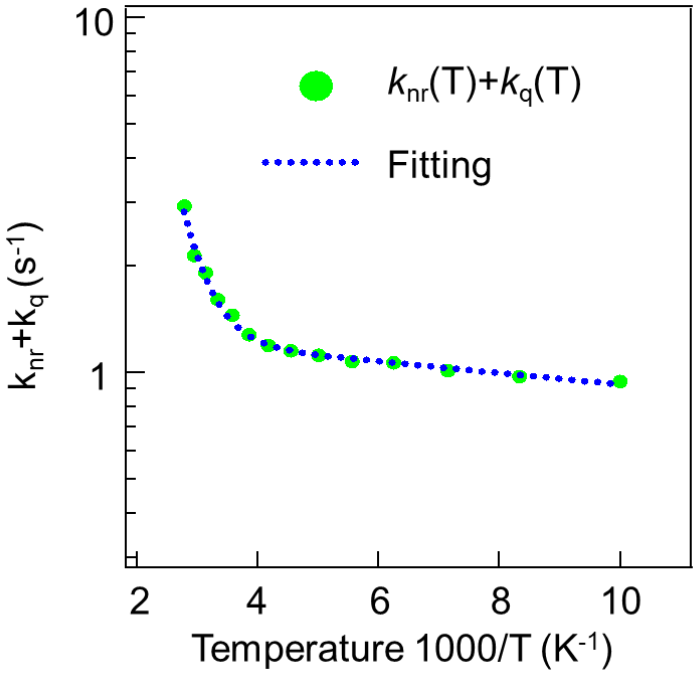

Figure 4-4. Temperature dependence of $k_{nr}(T)+k_q(T)$. Reprinted from ref. [39].

4-3-2 Measurement of triplet exciton diffusion

From the measurement of the temperature dependence of $k_{nr}(T)+k_q(T)$, the very small value of $k_q(T)$ at RT was extracted. This suppressed $k_q(T)$ at RT is responsible for the persistent RTP in the CzDClT crystal. Therefore, understanding the origin of the suppressed k_q is very important for obtaining efficient persistent RTP from crystalline state. However, deeper understanding or further discussion of k_q cannot be obtained from the temperature dependence alone. The factors that determine the value of k_q are the crystal size, the concentration of defect sites, the concentration of oxygen and L_t. In this experiment, L_t in CzDClT single crystal was measured as a primary determining factor of k_q because the other factors determining k_q are largely dependent on the value of L_t if L_t is long enough. Hence, the measurement of L_t is considered crucial for elucidation of suppressed k_q. For estimation of the value of L_t, triplet exciton diffusion was visualized

with epi-fluorescence microscope. As explained in chapter 1, the visualization of triplet exciton diffusion is based on the spatial spread of emission. In the following, the photophysical processes used for the visualization of triplet exciton diffusion in the crystals used in this experiment are explained (Fig. 4-5). In the case of CzDClT single crystal, photoexcitation (at 360 nm) is focused on the surface of the crystal. The excited singlet excitons are converted to triplet excitons via ISC, and the generated triplet excitons diffuse in the crystal. Eventually, photons of persistent RTP are emitted in the vicinity of the excitation spot (Fig. 4-5a). In a phosphorescence microscopic image, the size of persistent RTP directly reflects the triplet diffusion length L_t. On the other hand, the triplet lifetime τ_t of rubrene single crystal was 100 μs,[28] leading to no detectable persistent RTP. In addition, the triplet exciton diffusion in rubrene single crystal has been measured and visualized before.[29] Therefore, rubrene single crystal can be used as a reference sample of a molecular crystal without persistent RTP. Triplet exciton diffusion in a rubrene single crystal was measured using the same optical setup (with excitation at 442 nm). The generated singlet excitons of rubrene are immediately converted into triplet excitons via efficient singlet fission (SF).[29] After SF, triplet excitons diffuse in the crystal, followed by TTA and subsequent delayed fluorescence (Fig. 4-5b). The photons of delayed fluorescence are emitted in the vicinity of the excitation, and the microscopic size of the emission image reflects the extent of the triplet exciton diffusion. Analyzing the microscopic images of the emission and of the focused excitation, the value of L_t can be estimated (see the appendix for the details).

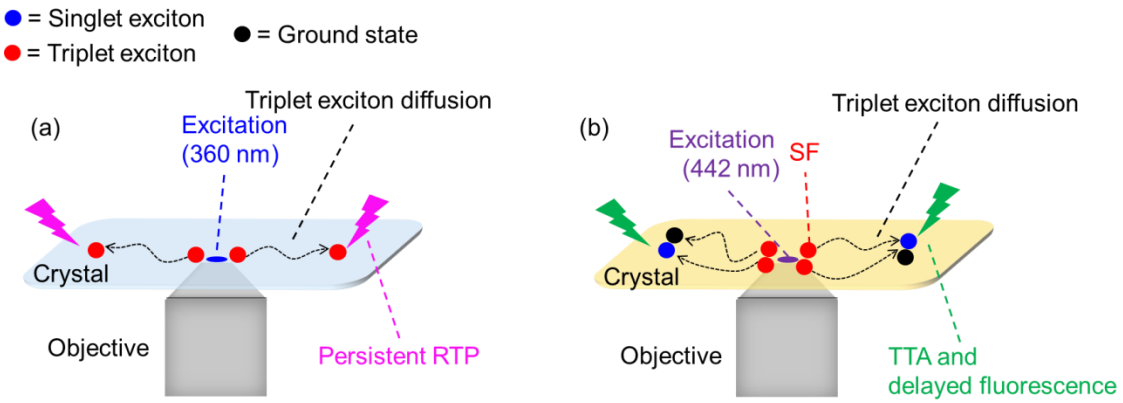

Figure 4-5. Illustration of the detection scheme for visualization of triplet exciton diffusion via (a) persistent RTP and (b) TTA-induced delayed fluorescence. Reprinted from ref. [39].

The crystal structures of rubrene (taken from ref. [30]) and that of CzDClT (measured by X-ray analysis) are shown in Fig. 4-6. The lattice parameters of rubrene are a = 26.86 A, b = 7.193 A, c = 14.433 A and those of CzDClT are a = 20.283 A, b = 8.0648 A, c = 15.995 A. As seen from these parameters and the Fig. 4-6, both crystal structures show efficient molecular packing in the direction of the crystal b axis. Since Dexter-type energy transfer requires molecular orbital overlap, triplet exciton diffusion along b axis should be efficient in both crystals.

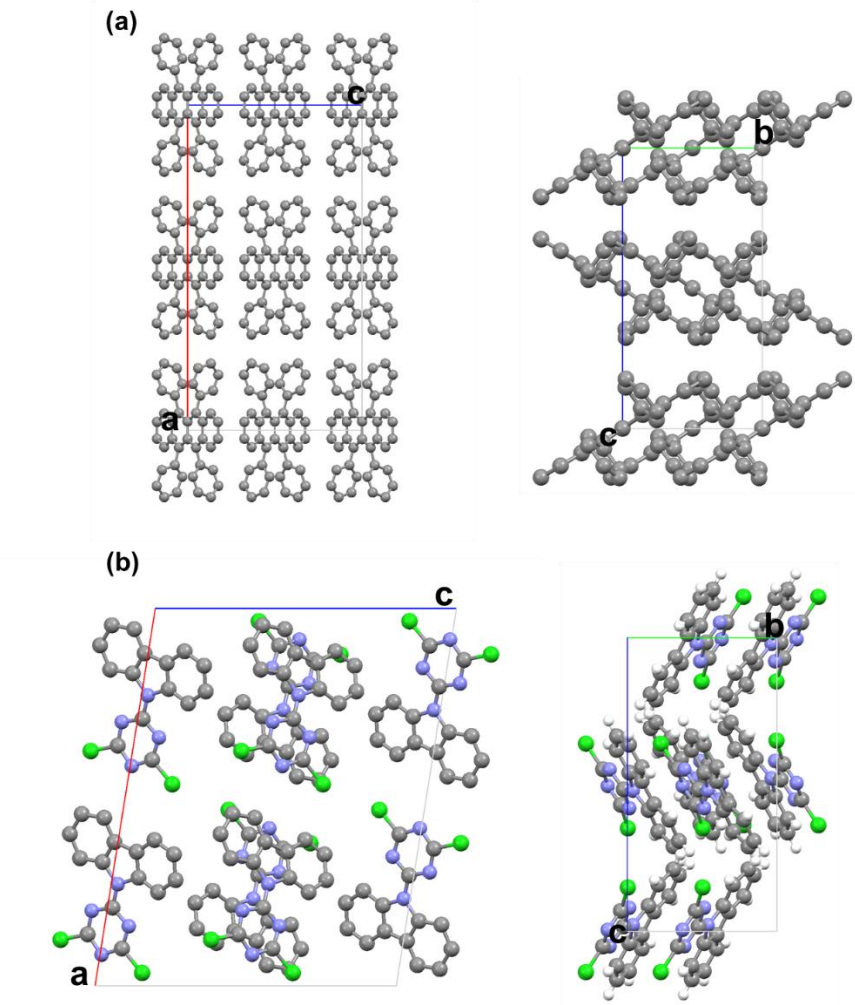

Figure 4-6. Crystal structure of (a) rubrene as reported in ref. [30] and (b) CzDClT. Reprinted from ref. [39].

Fig. 4-7a and b show microscopic images of delayed fluorescence from rubrene single crystal and of the corresponding focused laser excitation, respectively. Fig. 4-7c shows one-dimensional intensity cross-sections of the two images along the *b* crystallographic axis. Compared with the excitation spot, anisotropically extended delayed fluorescence image can be observed in the Fig. 4-7a. The anisotropy reflects the fact that triplet excitons diffuse mainly along the *b* crystallographic axis as expected, and as also reported previously (e.g., in ref. [29]). In the same manner as explained in the chapter 2, the one-

dimensional fluorescence intensity cross-section along the b crystallographic axis $I_{\mathrm{r}}(x)$ can be expressed as,

$$I_{\mathrm{r}}(x) = n_{\mathrm{s}}(x) \times f_{\mathrm{PSF}}(x). \qquad (4\text{-}1)$$

Considering that the delayed fluorescence from rubrene single crystal occurs via TTA, $n_{\mathrm{s}}(x)$ can be expressed as the square of the $n_{\mathrm{t}}(x)$ as explained in the chapter 2. Therefore, by using the equation (4-1) and the equation (2-2), and assuming that the focused laser excitation profile can be approximated by a Gaussian function, the value of L_{t} in rubrene single crystal can be estimated by fitting to the one-dimensional intensity cross-section of the delayed fluorescence. In this study, only the tale of the fluorescence profile was fitted using equation (4-1) because the part of the profile at the position of the excitation (x=0) reflects not only the delayed fluorescence but also strong prompt fluorescence (Fig. 4-7c). As a result of the fitting, L_{t} is calculated as 3.4 μm. This value of L_{t} is comparable with that obtained previously by this method and other techniques[29].

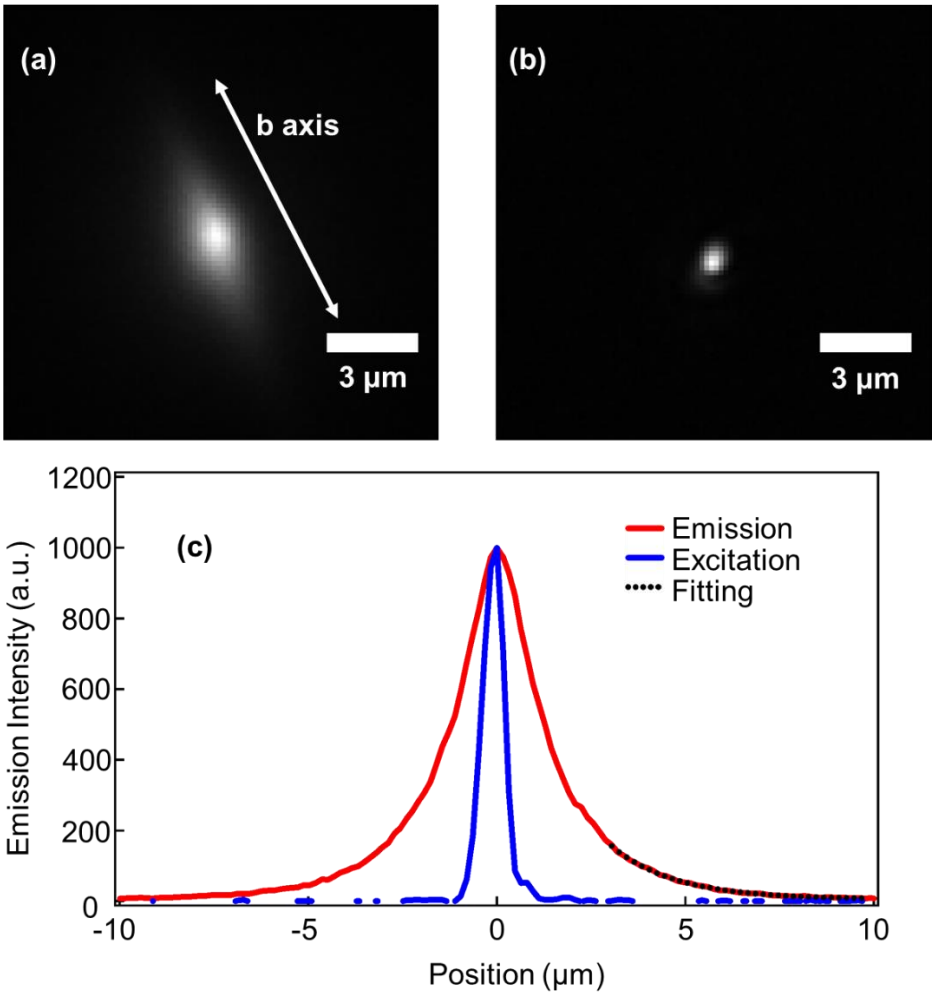

Figure 4-7. (a) Microscopic image of delayed fluorescence from rubrene single crystal. The arrow indicates the direction of the crystallographic *b* axis. (b) Image of excitation profile focused on the rubrene single crystal. (c) One-dimensional intensity cross-sections of (a) and (b) along the crystallographic *b* axis. The dotted line represents fit of the delayed fluorescent cross-section to equation (4-1). Reprinted from ref. [39].

In the case of CzDClT single crystal, the microscopic image of persistent RTP detected 0.1 s after ceasing excitation is shown in Fig. 4-8a and the corresponding excitation image is shown in Fig. 4-8b. Fig. 4-8c shows one-dimensional intensity cross-section of the two images along the *b* crystallographic axis. The one-dimensional intensity cross-section of persistent RTP along the *b* crystallographic axis $I_c(x)$ can be expressed as,

$$I_c(x) = n_t(x) \times f_{PSF}(x) \qquad (4\text{-}2)$$

Fitting of the one-dimensional intensity cross-section of persistent RTP using the equation (4-2) and the equation (2-1) gives the value of L_t of 0.42 μm.

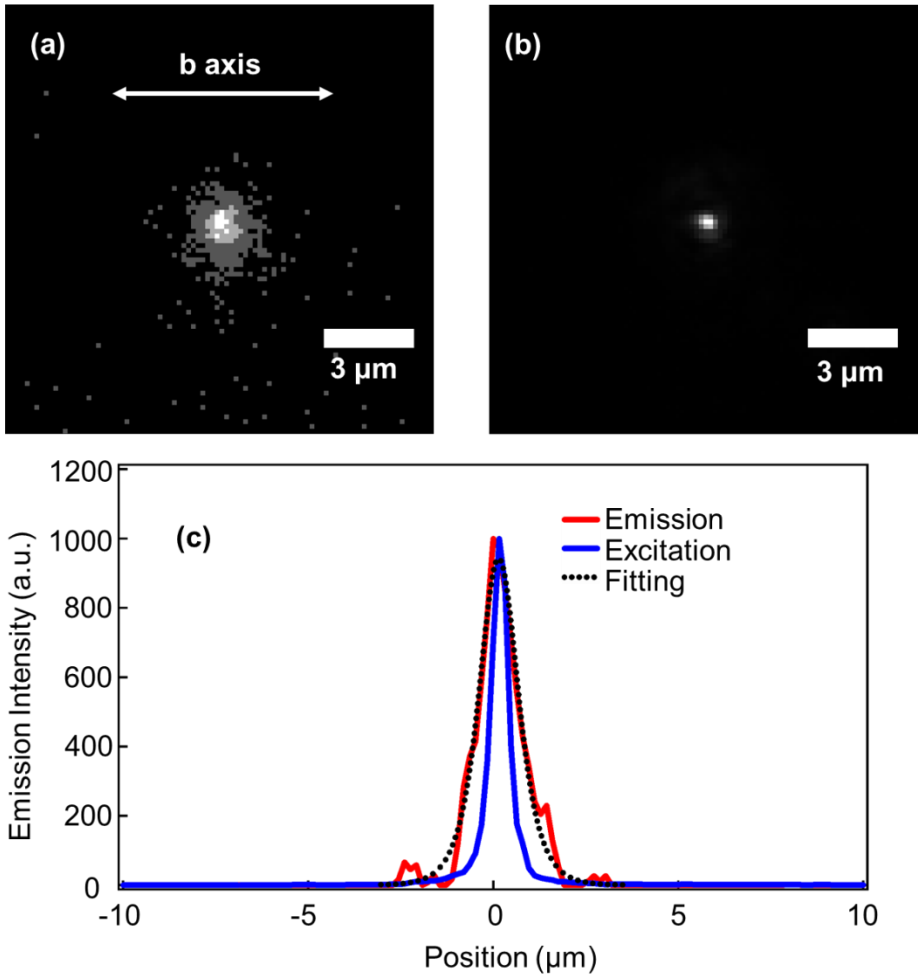

Figure 4-8. (a) Microscopic image of persistent RTP from CzDClT single crystal. The arrow indicates the direction of the crystallographic *b* axis. (b) Image of excitation profile focused on the CzDClT single crystal. (c) One-dimensional intensity cross-sections of (a) and (b) along the crystallographic *b* axis. The dotted line represents fit of the cross-section of persistent RTP to equation (4-2). Reprinted from ref. [39].

Generally, in the case of materials showing persistent RTP, the phosphorescence intensity (the population of triplet excitons) is gradually saturated as the excitation intensity increases.[31] Fig. 4-9 shows dependence of phosphorescence intensity of CzDClT single

crystal on excitation intensity. As seen in the Fig. 4-9, the intensity of persistent RTP is starts saturating for the excitation intensity values above 0.01 mW cm^{-2}. Such saturation of intensity of persistent RTP can lead to an overestimation of the value of L_t because the emission profile in the microscopic image at the position of the excitation (x~0) is broadened due to the saturation effect (Fig. 4-10). Therefore, the excitation intensity should be as low as possible when triplet exciton diffusion in materials with persistent RTP is visualized. In this experiment, the minimum mean excitation intensity that is detectable by the present optical setup was 0. 61 mW cm^{-2}. This value is still much stronger than the threshold of saturation (0.01 mW cm^{-2}). Thus, the measured value of L_t of 0.42 μm has to be considered as an upper limit of the experimentally determined diffusion length. Even as such, the value of L_t in the CzDClT single crystal is still an order of magnitude smaller than that in the rubrene single crystal.

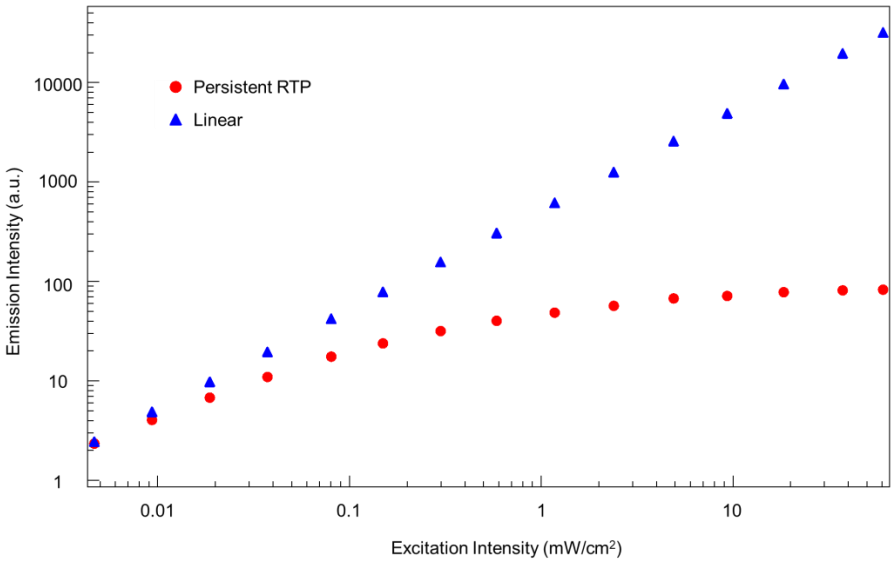

Figure 4-9. Dependence of intensity of persistent RTP on excitation intensity (red circle). Blue triangles represent a linear asymptotic line. Reprinted from ref. [39].

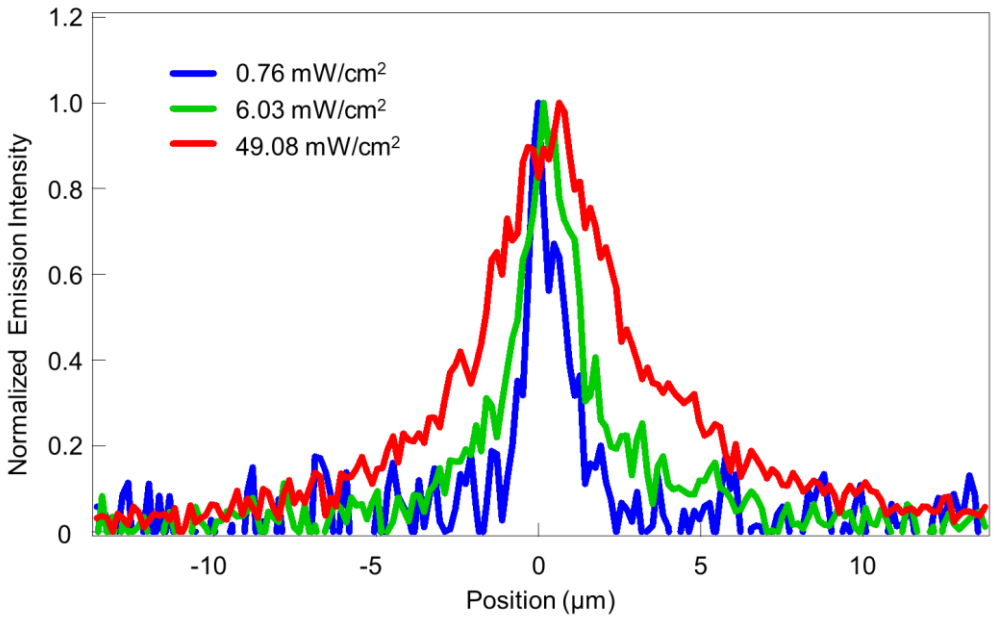

Figure 4-10. One dimensional cross-section of the intensity of persistent RTP from CzDClT single crystal. The excitation intensity of blue, green and red line is 0.76 mW/cm^2, 6.03 mW/cm^2 and 49.08 mW/cm^2, respectively. Reprinted from ref. [39].

To understand the origin of the small value of L_t in the CzDClT single crystal, triplet exciton diffusion coefficients D_t of CzDClT and rubrene were calculated. Generally, as shown in equation (1-3), D_t can be calculated using the measured values of L_t and τ_t. The values of D_t of rubrene and of CzDClT were calculated as 1.1×10^{-3} cm^{2}s^{-1} and 3.0×10^{-9} cm^{2}s^{-1}, respectively. The calculation shows that the value of D_t of CzDClT is several orders of magnitude smaller than that of rubrene. Comparison with other heavy atom-free aromatic crystals also shows that the value of D_t of CzDClT is much smaller than those in such crystals (e.g., ref in [32]). This very small value of D_t in CzDClT is considered responsible for the short L_t.

To further understand the small D_t of CzDClT, quantum chemical calculations were performed. Considering that triplet exciton diffusion is based on Dexter-type energy transfer which itself can be considered as double electron transfer (simultaneous electron

and hole transfer), D_t can be approximated as,

$$D_t \propto k_{et} \times k_{ht} \qquad (4\text{-}3)$$

where the k_{et} and k_{ht} are the electron and hole transfer rates, respectively.[33] In the frame of the Marcus electron transfer theory, the $k_{et}(T)$ and $k_{ht}(T)$ can be expressed as,

$$k_{et(ht)}(T) = \frac{t^2_{et(ht)}}{\hbar}\sqrt{\frac{\pi}{\lambda_{et(ht)}k_B T}}\exp(\frac{-\lambda_{et(ht)}}{4k_B T}) \qquad (4\text{-}4)$$

where T is temperature, k_B is Boltzmann constant and $\hbar$ is Planck's constant. In order to calculate the values of $\lambda_{et(ht)}$, molecular structures optimized using Hybrid-B3LYP and TZP as exchange-correlation functionals with a Slater-type all-electron basis were used, respectively.

As shown in Fig.4-6, triplet excitons in both crystals are incline to diffuse along the *b* crystallographic axis. Therefore, in the present calculations, molecular dimers chosen along the *b* crystallographic axis in both crystals were used as basic energy transfer units for the calculation of $k_{et(ht)}$. The dimer in rubrene along the *b* axis is called dimer R. In the case of CzDClT, there are two kinds of slightly different dimers along the *b* crystallographic axis, and these are denoted as dimer 1 and dimer 2 (see the appendix for the details). The calculated values of $t_{et(ht)}$, $\lambda_{et(ht)}$, $k_{et(ht)}$ and $k_{et} \times k_{ht}$ of the dimer R, the dimer 1 and the dimer 2 are shown in Table 4-1. For rubrene, the calculated value of $k_{et} \times k_{ht}$ of the dimer R is 7.0×10^{26} s^{-2}. For CzDClT, the values for the dimer 1 and dimer 2 are 2.0×10^{22} s^{-2} and 7.0×10^{22} s^{-2}, respectively. It should be noted that other calculation results show that the values of $k_{et} \times k_{ht}$ of the dimer 1 and dimer 2 are much larger than those of other possible dimers in the CzDClT crystal (see the appendix for the details). This implies that triplet exciton diffusion along the *b* crystallographic axis is more efficient compared to the diffusion along the *a* or *c* crystallographic axes. The value

of $k_{\mathrm{et}} \times k_{\mathrm{ht}}$ of the dimer 1 is smaller than that of the dimer 2, which means that the transfer rate of the dimer 1 is a limiting factor for the triplet exciton diffusion along the *b* crystallographic axis. Therefore, in the following discussion, only the dimer 1 is considered as a primary dimer in the CzDClT crystal. Comparing CzDClT with rubrene, the value of $k_{\mathrm{et}} \times k_{\mathrm{ht}}$ of the dimer 1 is 4 orders of magnitude smaller than that of the dimer R. This large difference is responsible for the large difference in the values of D_{t} between two crystals.

	t_{ht} (meV)	t_{et} (meV)	λ_{ht} (meV)	λ_{et} (meV)	k_{ht} (s^{-1})	k_{et} (s^{-1})	$k_{\mathrm{ht}} \times k_{\mathrm{et}}$ (s^{-2})	D_{t} ($cm^2 s^{-1}$)
Dimer R	95.15	-47.13	166.5	220.4	7.43×10^{13}	9.40×10^{12}	7.0×10^{26}	1.1×10^{-3}
Dimer 1	3.48	79.25	395.1	420.0	7.10×10^{9}	2.80×10^{12}	2.0×10^{22}	3.0×10^{-9}
Dimer 2	14.38	35.87			1.21×10^{11}	5.75×10^{11}	7.0×10^{22}	

Table 4-1. Calculated parameters of transfer integral, reorganization energy, transfer rate, $k_{\mathrm{et}} \times k_{\mathrm{ht}}$ and diffusion coefficient.

The origin of the calculated small value of $k_{\mathrm{et}} \times k_{\mathrm{ht}}$ of the dimer 1 can be attributed to the very small value of t_{ht} of this dimer. As shown in Table 4-1 and as mentioned above, the calculated value of t_{ht} is 4 orders of magnitude smaller than that of dimer R while the value of t_{et} of the dimer 1 is comparable with that of the dimer R. The different values of t_{ht} between the dimer 1 and the dimer R can be traced to different overlap of molecular orbitals related to the T_1-S_0 transition. Fig. 4-11 shows HOMO and LUMO orbitals of rubrene and of CzDClT, respectively. As seen in the Fig. 4-11, both HOMO and LUMO orbitals of rubrene are localized on the tetracene unit. Therefore, such molecular orbitals in face-to-face molecular packing in the dimer R lead to large orbital overlaps between HOMO and HOMO (as well as between LUMO and LUMO), resulting

in the large values of t_{et}, t_{ht} (k_{et}, k_{ht}) and consequently in large values of D_{t} (Fig. 4-12a). On the other hand, the HOMO orbital of CzDClT is localized on the carbazole unit while its LUMO orbital is delocalized over the molecule (Fig. 4-11), which means that the CzDClT molecule has CT characteristic. Considering the electron transfer in the dimer 1, molecular orbital overlap between LUMO and LUMO is large due to the delocalization of LUMO, resulting in the large value of t_{et} (and k_{et}). This value is comparable with t_{et} (and t_{ht}) of rubrene. On the other hand, for the hole transfer in the dimer 1, the localization of the HOMO orbital on the carbazole unit, together with the molecular packing in the dimer in which the two monomers face opposite sides, cause small molecular orbital overlap between the HOMO orbitals. This small HOMO – HOMO overlap leads to the very small value of t_{ht} (and k_{ht}), and this very small value of t_{ht} in the dimer 1 is responsible for the small value of D_{t} of CzDClT (Fig. 4-12b).

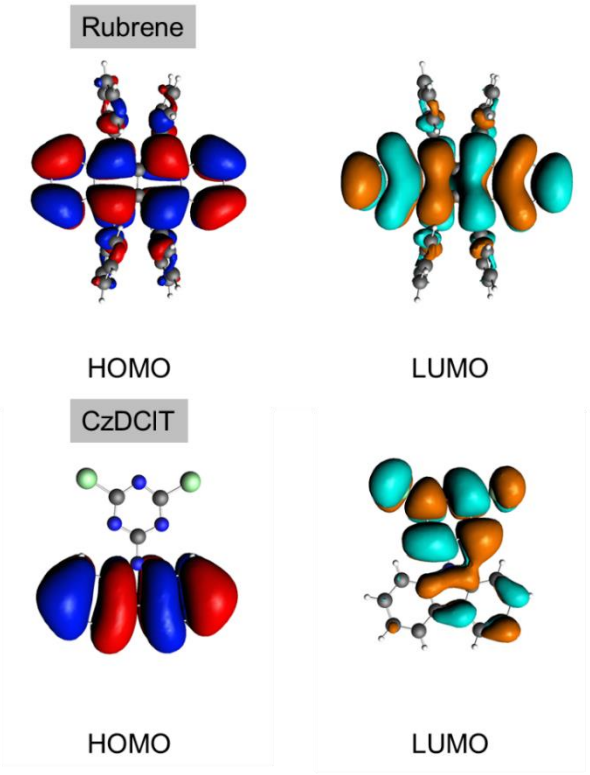

Figure 4-11. Molecular orbitals related to T_1-S_0 transition of rubrene (top) and CzDClT (bottom). Reprinted from ref. [39].

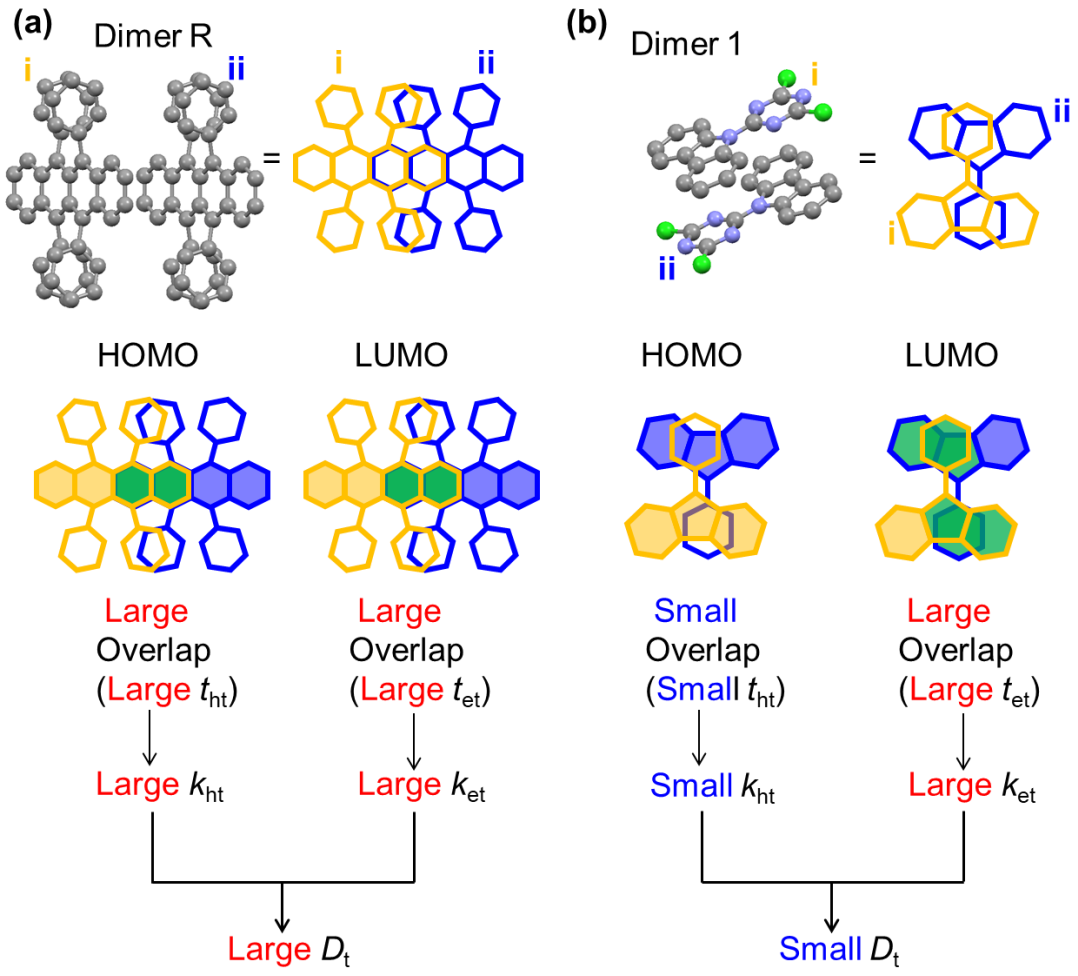

Figure 4-12. (a,b) Top: Illustration of molecular dimers along the crystallographic *b* axis : dimer R in rubrene a) and dimer 1 in CzDClT b). The two molecules in the dimers are denoted as I and ii. Bottom: Schematic illustration of molecular orbital overlaps and the explanation of the relationship between the orbital overlaps and D_t for rubrene a) and CzDClT b). Molecular orbitals of molecules i and ii are shaped in orange and blue, and the orbital overlaps are shaped in green. Reprinted from ref. [39].

4-4 Summary

In this chapter, triplet exciton diffusion in CzDClT single crystal was discussed. The measured values of exciton diffusion length L_t and diffusion coefficient D_t were < 0.42 μm and < 3.0×10^{-9} cm^2 s^{-1}, respectively. D_t in CzDClT was found much smaller than in other conventional aromatic crystals. Small molecular orbital overlap between HOMO and HOMO leads to such a small value, in spite of favorable molecular stacking along the *b* crystallographic axis. This small value of D_t is responsible for the short L_t.

Short L_t is crucial for the appearance of persistent RTP. Suppressed triplet exciton diffusion prevents triplet excitons from reaching defect sites inside or on the surface of the crystal leading, to the decrease of the quenching rate k_q. As a result, triplet lifetime is increased and persistent RTP can be obtained in spite of intrinsically very small value of phosphorescence rate k_p. So far, the discussion of the mechanism of persistent RTP in crystalline materials in literature has focused on the molecular packing and molecular conformation that might lead to the induced rigidity. Here, a mechanism contributing to the persistent RTP is unraveled by visualization of triplet exciton diffusion. Molecular packing with small orbital overlap is found to be preferable for persistent RTP, pointing to a strategy for molecular design of persistent RTP in molecular solids.

In addition to persistent RTP, suppressed triplet exciton diffusion is also considered crucial for TTA-based UC materials and TADF-based electroluminescence materials. In the case of TTA UC materials, as explained in Chapter 2, long L_t is necessary to obtain lower I_{th} for use of weak continuous light such as sunlight. However, on the other hand, too long L_t can decrease the efficiency of UC emission.[34] In the field of TADF-based electroluminescence materials, minimizing the quenching effect caused by triplet exciton diffusion is considered important for high efficiency.[35-38] Therefore, new insights on the

role of suppressed triplet exciton diffusion in organic molecular materials will be important for UC materials as well as TADF-based electroluminescence materials. Furthermore, the cooperative analysis of visualization of triplet exciton diffusion and quantum chemical calculation will be necessary for various opto-electronic devices.

Chapter 4 Appendix

1. Calculation of Φ_{isc} of CzDClT crystal

Intersystem crossing efficiency Φ_{isc} of the CzDClT crystal was calculated as $\Phi_{isc} \sim 1 - \Phi_f = 95$ %. As mentioned in the section 4-3-1, this approximation can be used when a conjugated molecule has a rigid planar structure and, furthemore, its S_1 excitation energy is above 2.7 eV without conical intersections.[7] In the case of CzDClT in solution, the singlet excited state lifetime is 0.2 ns (Fig. A4-2). This short singlet lifetime is attributed to the largely twisted molecular structure in the optimized S_1 (Fig. A4-3). In addition, there is no signal of transient absorption due to very fast deactivation of S_1, which means that very low value of Φ_{isc} is very low (Fig. A4-2). On the other hand, quantum chemical calculations using the crystalline structure of CzDClT were also performed. The optimized structures of S_0 as well as S_1 are coplanar and, furthermore, the optimized S_1 has large energy (Fig. A4-4). Therefore, in the case of crystalline state, Φ_{isc} of CzDClT can be approximated as $\Phi_{isc} \sim 1 - \Phi_f$.

2. Density of triplet excitons excited by focused Gaussian laser beam

Assuming that excitation is irradiated only at the position $x = 0$, rate equation of triplet exciton population can be expressed as

$$\frac{dn_{t0}(x)}{dt} = G - kn_{t0}(x) + D_t \frac{dn_{t0}^2(x)}{dx^2} \qquad \text{(A4-1)}$$

where $n_{t0}(x)$ is one-dimensional spatial density of triplet excitons, G is the excitation source and k is reciprocal number of lifetime of triplet excitons. $n_{t0}(x)$ can be expressed as a solution in steady state as

$$n_{t0}(x) = N_{t0}\exp(-x/L_t) \quad (x > 0)$$

$$n_{t0}(x) = N_{t0}\exp(x/L_t) \quad (x < 0) \qquad \text{(A4-2)}$$

where N_{t0} is a constant. Real one-dimensional density of triplet excitons $n_t(x)$ that is measured under the present experimental conditions (using focused Gaussian laser beam) can be considered as a convolution function with $f_{exc}(x)$ as

$$n_t(x) = N_{t0}\exp(-x/L_t) * f_{exc}(x) \quad (x > 0)$$

$$n_t(x) = N_{t0}\exp(x/L_t) * f_{exc}(x) \quad (x < 0) \qquad \text{(A4-3)}$$

In the following, $f_{exc}(x)$ is approximated by a Gaussian function.

3. Convolution function for delayed fluorescence image fitting to extract L_t of rubrene

As mentioned in Chapter 2, in the CCD camera images, $I_r(x)$ can be expressed as a convolution of $n_s(x)$ with $f_{psf}(x)$ as shown in equation (4-1). Thus, assuming that $f_{psf}(x)$ has a Gaussian profile, $I_r(x)$ can be expressed using equation (2-2), equation (4-1) and equation (A4-3) as

$$I_r(x) = \exp\left({}^{2x}/_{L_t}\right) \times \mathrm{erfc}\left(\frac{{}^{2\sigma^2}/_{L_t}+x}{\sqrt{2}\sigma^2}\right) + \exp({}^{-2x}/_{L_t}) \times \mathrm{erfc}\left(\frac{{}^{2\sigma^2}/_{L_t}-x}{\sqrt{2}\sigma^2}\right) \qquad \text{(A4-4)}$$

where σ^2 is the variance of $f_{exc}(x) * f_{psf}(x)$ expressed as

$$\sigma^2 = \sigma_{exc}^2 + \sigma_{psf}^2 \qquad \text{(A4-5)}$$

Here, σ_{exc}^2 and σ_{psf}^2 are the variances of $f_{exc}(x)$ and $f_{psf}(x)$, respectively. The value of σ_{exc}^2 was obtained from Gaussian fitting of the one-dimensional cross section in Fig. 4-7b. The σ_{psf}^2 is calculated using equation (A2-3).

The value of λ was taken as the singlet energy of rubrene at 532 nm.

4. Convolution function for phosphorescence image fitting to extract L_T of CzDClT

In the case of CzDClT single crystal, the image of persistent RTP as shown in Fig. 4-8a was obtained after ceasing the excitation because the fluorescence signal would overwhelm the weak persistent RTP. Although such experimental condition is not strictly a steady state, it was assumed that $n_t(x)$ can be still expressed using the equation (A4-3) because the ultralong-lived triplet excitons are deactivated very slowly. By using the equation (A4-3) and equation (4-2), $I_c(x)$ can be expressed as

$$I_c(x) = \exp(x/L_t) \times \mathrm{erfc}\left(\frac{\sigma^2/L_t + x}{\sqrt{2}\sigma^2}\right) + \exp(-x/L_t) \times \mathrm{erfc}\left(\frac{\sigma^2/L_t - x}{\sqrt{2}\sigma^2}\right) \quad \text{(A4-6)}$$

Here, the value of σ_{exc}^2 was obtained from Gaussian fitting of the one-dimensional cross section in Fig. 4-8b. The σ_{psf}^2 was calculated using the equation (A2-3) and λ is obtained from the peak of phosphorescence spectrum at 550 nm, as shown Fig. 4-3.

5. The effect of TTA on broadening of the RTP emission profile

TTA and persistent RTP are two concurring processes. TTA quenches triplet excitons via nonradiative process, and a decrease of the intensity of persistent RTP can be caused by TTA. It should be further noted that, as explained in Chapter 2, TTA is a bimolecular process that will have increasing effect at high excitation intensities. Therefore, TTA results in a saturation effect of RTP intensity upon increasing excitation intensity (Fig. A4-9). Here, the excitation is considered as focused Gaussian laser beam and the mean excitation intensity was set to 0.61 mW/cm^2. Under such irradiation, the contribution of TTA is strongest at the center of the excitation profile. Consequently, at the center of the profile, diffusion length is shortened (due to the quenching by TTA) and simultaneously the intensity of persistent RTP (of the density of triplet excitons) is saturated (Fig. 4-10).

On the other hand, at the tail of the profile of persistent RTP, excitation intensity is less than 0.61 mW/cm^2 and the RTP intensity of this part is less saturated when compared with that at the center. The stronger saturation at the center leads to an apparent broadening of the RTP emission profile (after normalization of the emission profiles, Figure 4-10). As a result, these two cooperative effects can generally lead to overestimation of triplet exciton diffusion because the profile of persistent RTP is broadened due to the saturated intensity of persistent RTP. Therefore, under such conditions, the profile of persistent RTP should be fitted at the tail because the density of triplet excitons at the tail is reduced and the quenching rate of TTA is smaller. However, the overall profile of the persistent RTP of CzDClT is very sharp, probably due to the intrinsically very short triplet exciton diffusion length in the CzDClT single crystal, and it is difficult to fit the emission profile of CzDClT only at the tail. Here, we fitted the whole region of the emission profile, which may have resulted in the possibility of an overestimation of the measured value of triplet exciton diffusion length. The value of triplet exciton diffusion length and diffusion coefficient estimated in this experiment should thus be considered upper limits of the actual values. However, such an experimental limitation does not affect the new insight of the role of suppressed triplet exciton diffusion in CzDClT crystals.

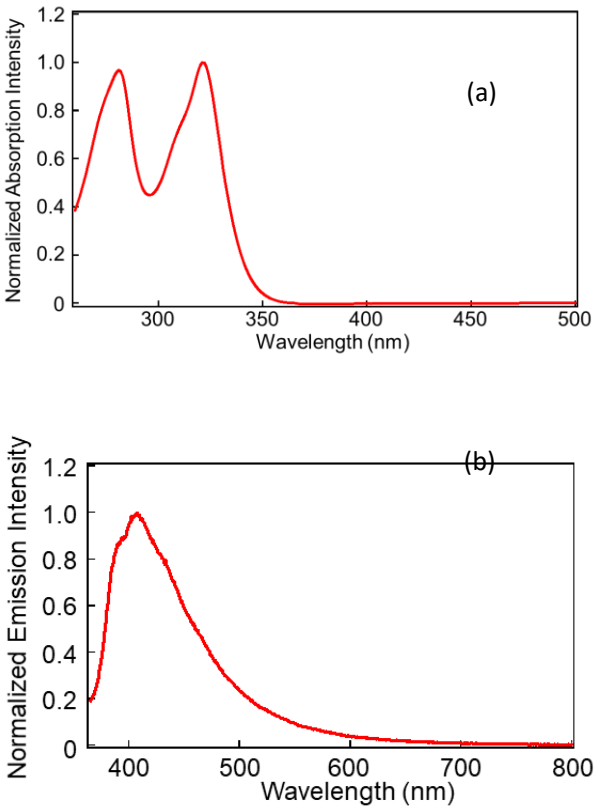

Figure A4-1. (a) Absorption spectrum of CzDClT in THF. (b) Fluorescence spectrum of CzDClT crystal. Reprinted from ref. [39].

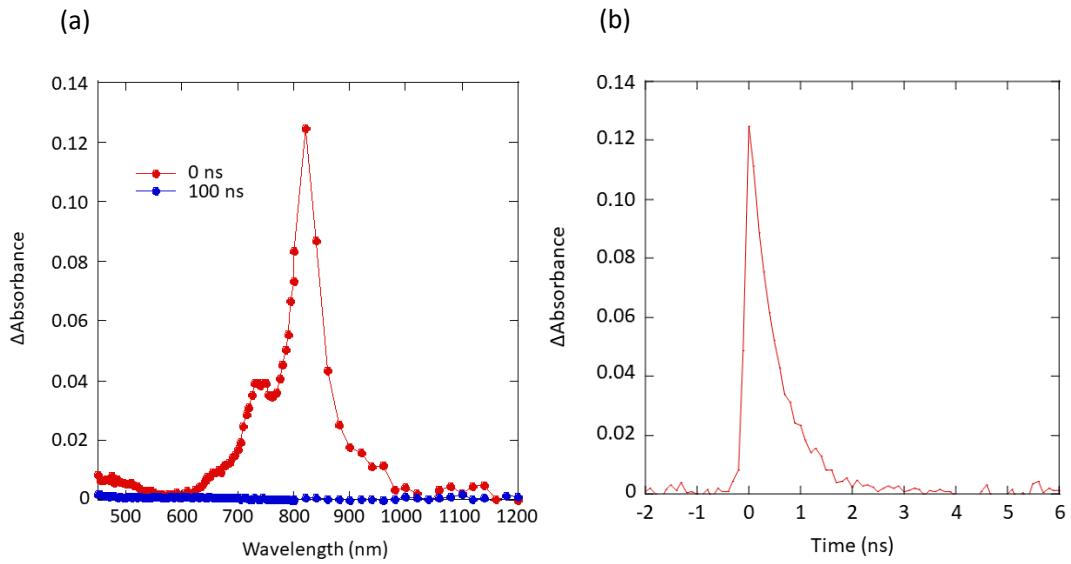

Figure A4-2. (a) Transient absorption spectra after 0 ns and 100 ns. Pulsed excitation at 355 nm with width of 25 ps was used. (b) Decay of transient absorption at 820 nm. Reprinted from ref. [39].

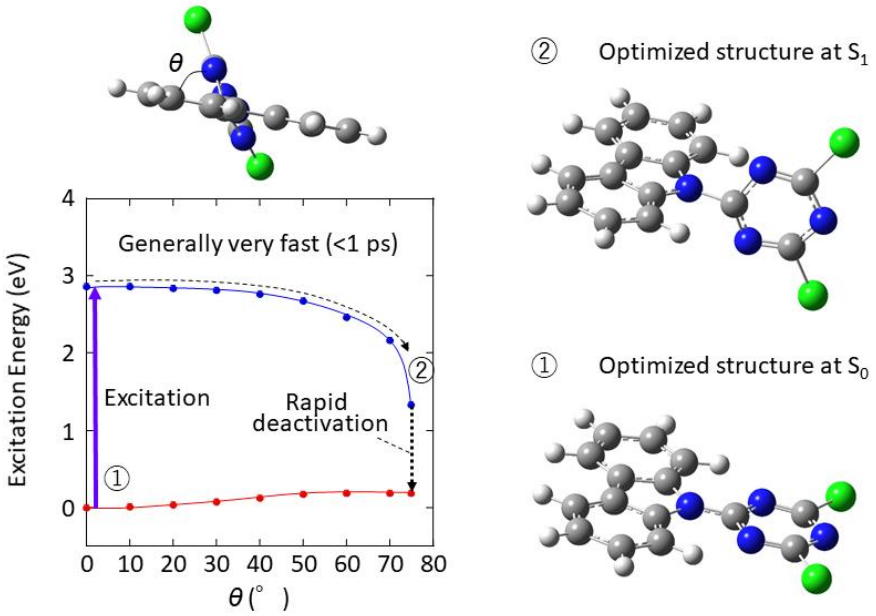

Figure A4-3. Energy change of S_0 and S_1 depending on the angle between triazine and carbazole (θ) of CzDClT by TD-DFT (Gaussian 09/B3LYP/6-31G(d)). For the S_0 curve (red), after the molecular conformation was optimized at S_0, only θ was changed in the optimized structure. Then, S_0 energies were calculated for the structures at each θ. For the S_1 curve (blue), after the molecular conformation was optimized with taking vibrations into considerations at S_1, only θ was changed in the optimized structure. Then, S_1 energies were calculated for the structures at each θ. Reprinted from ref. [39].

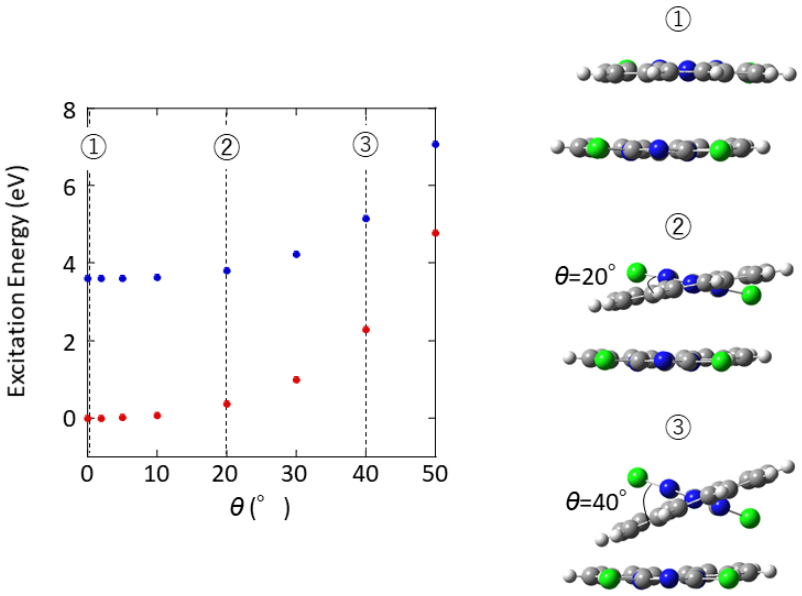

Figure A4-4. Potential energy surface of S_0 (red) and S_1 (blue) of dimer 1 of CzDClT. For one molecule in the conformation of the dimer, which is extracted from crystalline structure, the angle between carbazole and triazine (θ) of CzDClT was changed. Then, S_0 and S_1 energies were calculated for the structures at each θ using time dependent density functional theory (Gaussian09/B3LYP/6-31G(d)). Reprinted from ref. [39].

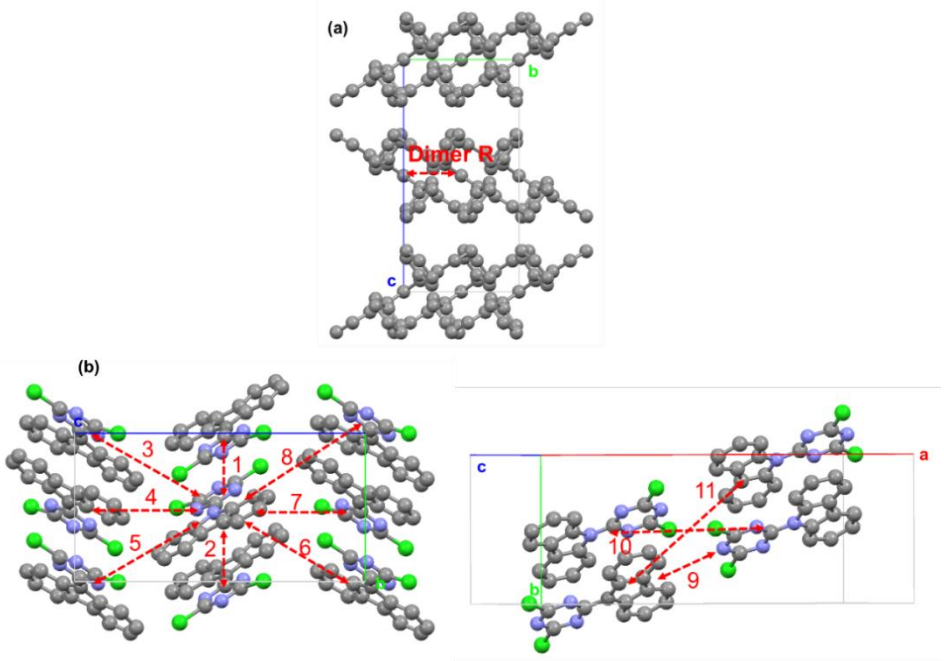

Figure A4-5. Definition of dimer of rubrene (a) and CzDClT (b). Reprinted from ref. [39].

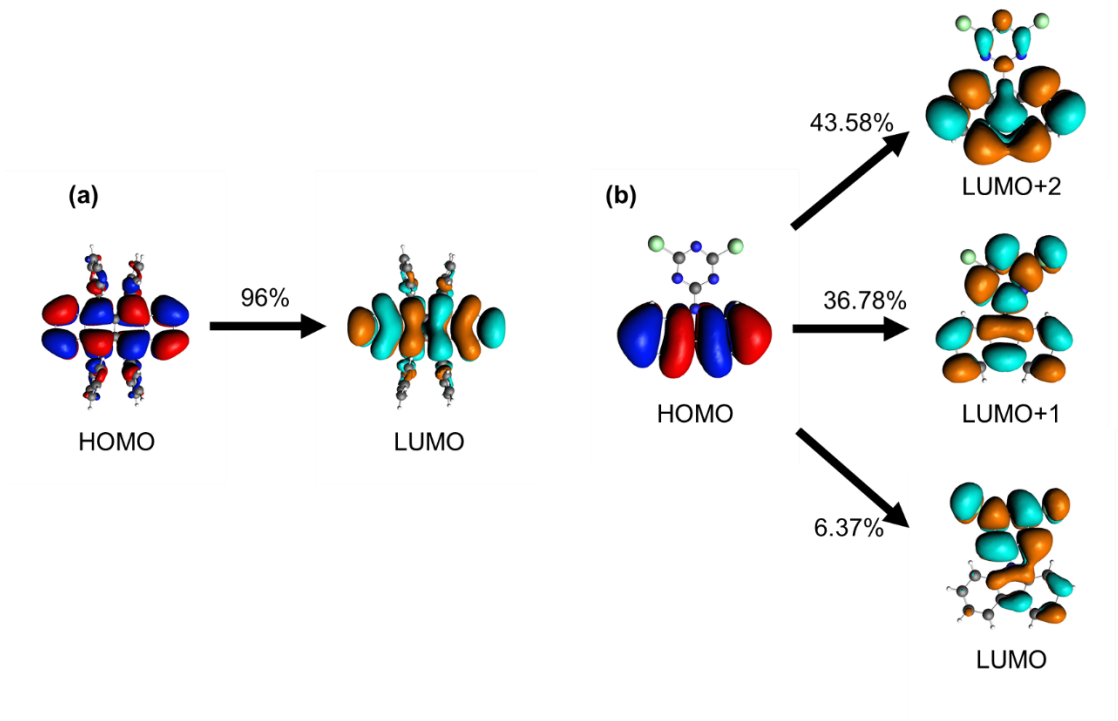

Figure A4-6. Weight factor related the transition from S_0 to T_1 of rubrene (a) and CzDClT (b). Reprinted from ref. [39].

Table A4-1. Calculated parameters of transfer integral, reorganization energy, transfer rate, $k_{et}(RT)k_{ht}(RT)$ and diffusion coefficient.

	t_{ht} (meV)	t_{et} (meV)	λ_{ht} (meV)	λ_{et} (meV)	k_{ht} (s^{-1})	k_{et} (s^{-1})	$k_{ht} \times k_{et}$ (s^{-2})	D_t ($cm^2 s^{-1}$)
Dimer 1	3.48	79.25			7.10×10^{9}	2.80×10^{12}	2.0×10^{22}	3.0×10^{-9}
Dimer 2	14.38	35.87			1.21×10^{11}	5.75×10^{11}	7.0×10^{22}	
Dimer 3	26.41	-0.30			4.07×10^{11}	3.95×10^{7}	1.6×10^{19}	
Dimer 4	11.24	1.89			7.37×10^{10}	1.59×10^{9}	1.2×10^{20}	
Dimer 5	26.45	-0.33			4.09×10^{11}	4.73×10^{7}	1.9×10^{19}	
Dimer 6	0.10	-0.23	395.1	420.0	5.88×10^{6}	2.37×10^{7}	1.4×10^{14}	
Dimer 7	11.19	1.88			7.32×10^{10}	1.57×10^{9}	1.2×10^{20}	
Dimer 8	0.11	-0.22			7.06×10^{6}	2.15×10^{7}	1.6×10^{14}	
Dimer 9	-0.10	-2.56			6.19×10^{6}	2.93×10^{9}	1.8×10^{16}	
Dimer 10	0.00	-8.12			0.00	2.94×10^{10}	0	
Dimer 11	0.69	-0.08			2.78×10^{8}	2.65×10^{6}	7.6×10^{14}	
Rubrene	95.15	-47.13	166.5	220.4	7.43×10^{13}	9.40×10^{12}	7.0×10^{26}	1.1×10^{-3}

Chapter 4 References

1. M. A. Baldo, D. O'brien, Y. You, A. Shoustikov, S. Sibley, M. E. Thompson, S. R. Forrest, *Nature* **1998**, *395*, 151.
2. M. A. Baldo, S. Lamansky, P. E. Burrows, M. E. Thompson, S. R. Forrest, *Appl. Phys. Lett.* **1999**, *75*, 4.
3. D. E. J. G. J. Dolmans, D. Fukumura, R. K. Jain, *Nat. Rev. Cancer* **2003**, *3*, 380.
4. S. Zhang, M. Hosaka, T. Yoshihara, K. Negishi, Y. Iida, S. Tobita, T. Takeuchi, *Cancer Res.* **2010**, *70*, 4490.
5. T. N. Singh-Rachford, F. N. Castellano, *Coord. Chem. Rev.* **2010**, *254*, 2560.
6. S. Reineke, *Nat. Mater.* **2015**, *14*, 459.
7. J. N. Turro, *Modern Molecular Photochemistry*, University Science Books, Sausalito, California, **1991**.
8. W. Z. Yuan, X. Y. Shen, H. Zhao, J. W. Y. Lam, L. Tang, P. Lu, C. Wang, Y. Liu, Z. Wang, Q. Zheng, J. Z. Sun, Y. Ma, B. Z. Tang, *J. Phys. Chem. C* **2010**, *114*, 6090.
9. O. Bolton, K. Lee, H. J. Kim, K. Y. Lin, J. Kim, *Nat. Chem.* **2011**, *3*, 205.
10. S. Hirata, K. Totani, J. Zhang, T. Yamashita, H. Kaji, S. R. Marder, T. Watanabe, C. Adachi, *Adv. Funct. Mater.* **2013**, *23*, 3386.
11. Y. Deng, D. Zhao, X. Chen, F. Wang, H. Song, D. Shen, *Chem. Commun.* **2013**, *49*, 5751.
12. X. Zhang, T. Xie, M. Cui, L. Yang, X. Sun, J. Jiang, G. Zhang, *ACS Appl. Mater. Interfaces* **2014**, *6*, 2279.
13. Z. An, C. Zheng, Y. Tao, R. Chen, H. Shi, T. Chen, Z. Wang, H. Li, R. Deng, X. Liu, W. Huang, *Nat. Mater.* **2015**, *14*, 685.
14. L. Bian, H. Shi, X. Wang, K. Ling, H. Ma, M. Li, Z. Cheng, C. Ma, S. Cai, Q. Wu,

N. Gan, X. Xu, Z. An, W. Huang, *J. Am. Chem. Soc.* **2018**, *140*, 10734.

15. A. S. Mathew, C. A. DeRosa, J. N. Demas, C. L. Fraser, *Anal. Methods* **2016**, *8*, 3109.
16. X. Zhen, Y. Tao, Z. An, P. Chen, C. Xu, R. Chen, W. Huang, K. Pu, *Adv. Mater.* **2017**, *29*, 1606665.
17. S. M. A. Fateminia, Z. Mao, S. Xu, Z. Yang, Z. Chi, B. Liu, *Angew. Chem. Int. Edit.* **2017**, *56*, 12160.
18. J. Yang, X. Zhen, B. Wang, X. Gao, Z. Ren, J. Wang, Y. Xie, J. Li, Q. Peng, K. Pu, Z. Li, *Nat. Commun.* **2018**, *9*, 840.
19. P. Long, Y. Feng, C. Cao, Y. Li, J. Han, S. Li, C. Peng, Z. Li, W. Feng, *Adv. Funct. Mater.* **2018**, *28*, 1800791.
20. M. A. El-Sayed, *J. Chem. Phys.* **1963**, *38*, 2834.
21. S. Hirata, M. Vacha, *J. Phys. Chem. Lett.* **2017**, *8*, 3683.
22. S. Hirata, *J. Phys. Chem. Lett.* **2018**, *9*, 4251.
23. Y. Gong, G. Chen, Q. Peng, W. Z. Yuan, Y. Xie, S. Li, Y. Zhang, B. Z. Tang, *Adv. Mater.* **2015**, *27*, 6195.
24. Y. Xie, Y. Ge, Q. Peng, C. Li, Q. Li, Z. Li, *Adv. Mater.* **2017**, *29*, 1606829.
25. S. Hirata, *J. Mater. Chem. C* **2018**, *6*, 11785.
26. D. B. Clapp, *J. Am. Chem. Soc.* **1939**, *61*, 523.
27. S. Pan, Z. Chen, X. Zheng, D. Wu, G. Chen, J. Xu, H. Feng, Z. Qian, *J. Phys. Chem. Lett.* **2018**, *9*, 3939.
28. A. Ryasnyanskiy, I. Biaggio, *Phys. Rev. B* **2011**, *84*, 193203.
29. P. Irkhin, I. Biaggio, *Phys. Rev. Lett.* **2011**, *107*, 017402.
30. O. D. Jurchescu, A. Meetsma, T. T. M. Palstra, *Acta Crystallogr., Sect. B: Struct. Sci.* **2006**, *62*, 330.

31. S. Hirata, M. Vacha, *Adv. Opt. Mater.* **2016**, *4*, 297.

32. O. V. Mikhnenko, P. W. M. Blom, T.-Q. Nguyen, *Energy Environ. Sci.* **2015**, *8*, 1867.

33. G. L. Closs, M. D. Johnson, J. R. Miller, P. Piotrowiak, *J. Am. Chem. Soc.* **1989**, *111*, 3751.

34. S. Raišys, K. Kazlauskas, S. Juršėnas, Y. C. Simon, *ACS Appl. Mater. Interfaces* **2016**, *8*, 15732.

35. Q. Zhang, D. Tsang, H. Kuwabara, Y. Hatae, B. Li, T. Takahashi, S. Y. Lee, T. Yasuda, C. Adachi, *Adv. Mater.* **2015**, *27*, 2096.

36. W. L. Tsai, M. H. Huang, W. K. Lee, Y. J. Hsu, K. C. Pan, Y. H. Huang, H. C. Ting, M. Sarma, Y. Y. Ho, H. C. Hu, C. C. Chen, M. T. Lee, K. T. Wong, C. C. Wu, *Chem. Commun.* **2015**, *51*, 13662.

37. R. Furue, T. Nishimoto, I. S. Park, J. Lee, T. Yasuda, *Angew. Chem., Int. Ed.* **2016**, *55*, 7171.

38. H. Liu, J. Zeng, J. Guo, H. Nie, Z. Zhao, B. Z. Tang, *Angew. Chem., Int. Ed.* **2018**, *57*, 9290.

39. K. Narushima, Y. Kiyota, T. Mori, S. Hirata, M. Vacha, *Adv. Mater.* **2019**, DOI: 10.1002/adma.201807268.

Chapter 5: Conclusion and Outlook

5-1 General conclusion

The main study focus in this thesis is triplet exciton diffusion in organic molecular materials. Triplet exciton diffusion is an important factor for not only improving the performance of opto-electronic devices but also for determining fundamental photophysical properties of materials. This thesis provided new information of triplet exciton diffusion in next-generation organic molecular materials.

In Chapter 1, overall background related to triplet exciton diffusion was explained. The study of triplet exciton diffusion in molecular crystals has long and rich history dating back to the 1960's, and here the major previous works were summarized, including the introduction of methods for the measurement of triplet exciton diffusion. Considering the recent rapid development of organic molecular materials and the prospect of molecular opto-electronic devices, it was emphasized that the development of novel measurement methods, as well as further understanding of triplet exciton diffusion are necessary.

TTA-based UC binary crystals composed of donor molecules and acceptor molecules were discussed in Chapter 2. In order to overcome the difficulty in measuring triplet exciton diffusion in polycrystalline films, the method of visualizing triplet exciton diffusion on the basis of functionalized inorganic nanoparticles was introduced. The use of such hybrid donor nanoparticles leads to nanoscale confinement of the generation of triplet excitons. Such confinement which is an order of magnitude smaller than the diffraction limit of light enables visualization of triplet exciton diffusion in polycrystalline films without the effect of excitation scattering. It also enables to uncover the effects of

crystal anisotropy for grain sized smaller that the diffraction limit. Compared with conventional indirect methods, the values of the triplet exciton diffusion length L_t measured by method introduced in this thesis can be considered reliable and accurate.

The objective of the study in Chapter 3 was the study of triplet exciton diffusion in conjugated polymer nanofibers. Due to their ease of processing and their semiconducting properties, conjugated polymers are considered promising materials for a range of opto-electronic device applications. Among them, the use of poly(phenylene vinylene) based conjugated polymer for triplet-triplet annihilation photon upconversion has been demonstrated before. However, the amorphous nature of the conjugated polymer films results in very short diffusion lengths of both singlet and triplet excitons, which in the case of TTA-based upconversion leads to high values of the excitation threshold. To decrease the threshold values, the use of conjugated polymer nanofibers was proposed in this thesis. The potential factors contributing to the improvement are the decreased dimensionality (the 1D nature of the nanofibers) and the orientation of the conjugated polymer chains inside the nanofibers. Conjugated polymer nanofibers fabricated by electrospinning showed high degree of orientation. Measurements of the exciton diffusion length revealed that this orientation contributed to the enhanced the value of L_t in nanofibers compared with that in spin-coated film by a factor of 1.8, and to overall decrease in the threshold value by a factor of 3.2.

The relationship between triplet exciton diffusion and suppression of triplet quenching in molecular crystalline materials showing persistent RTP was discussed in Chapter 4. The rate of quenching k_q of the CzDClT crystal determined from measured temperature dependence of overall non-radiative decay rate ($k_{nr}(T)+k_q(T)$) was very small. This small value of k_q stemmed from short triplet exciton diffusion length L_t in the CzDClT crystal.

The value of L_t in a CzDClT single crystal was measured directly by visualization in a microscope, and the resulting small value of L_t was attributed to small values of diffusion coefficient D_t. The obtained D_t of CzDClT is orders of magnitude smaller than other molecular crystals without persistent RTP. Quantum chemical calculations revealed that small molecular orbital overlap between HOMO and HOMO, caused by orbital localization and crystal structure, is the cause of the small value of D_t in CzDClT. This small value of D_t (and consequently the short L_t) prevents triplet excitons from reaching defect sites in the crystal or on the crystal surface, leading to the appearance of persistent RTP (suppressed k_q).

5-2 Outlook

From the above general conclusions, we would like to stress the following outlooks for further development in the field of organic molecular materials.

1) Accurate and reliable measurements of triplet exciton diffusion in TTA-based solid-state UC materials can be performed by using the method introduced in this thesis. The extent of triplet exciton diffusion in solid-state UC materials is related to not only the value of I_{th} but also the quantum efficiency of UC emission. Therefore, the knowledge of accurate L_t will potentially lead to optimization of the characteristics of TTA-based solid-state UC materials and to further development of their performance towards practical applications.
2) The enhancement and control of the value of L_t in conjugated polymer nanofibers are potentially useful for a range of opto-electronic devices, including TTA-based UC materials and organic solar cells. The value of L_t in the conjugated polymer used in this

thesis (super yellow) is intrinsically small in the polymer neat film, leading to only nanoscale improvement of the value of L_t in the conjugated polymer nanofibers. However, ultralong triplet exciton diffusion can be potentially realized for a conjugated polymer with appropriate triplet energy levels where intrinsically large L_t can be expected. In addition, as demonstrated in this thesis, lower threshold values I_{th} can be realized by using the conjugated polymer nanofibers due to the extended L_t. This strategy could ultimately lead to the development of low-threshold amorphous-state UC materials.

3) Suppressed triplet exciton diffusion is a determining factor for the appearance of persistent RTP. Therefore, molecular design that would realize crystal structures with small molecular orbital overlap can potentially lead to important new developments in the field of persistent RTP. In addition, the concept of suppressed triplet exciton diffusion can influence properties of other organic molecular materials such as TTA-based solid-state UC materials and solid-state TADF materials.

The study performed in this thesis is of fundamental nature, and as such contributes to the basic knowledge in the fields of organic photophysics and photochemistry. However, its outcome may prove very important for the further development and optimization of the above mentioned classes of molecular materials.

List of Publications

Related to the Thesis

1. Suppressed Triplet Exciton Diffusion Due to Small Orbital Overlap as a Key Design Factor for Ultralong-Lived Room-Temperature Phosphorescence in Molecular Crystals
   K. Narushima, Y. Kiyota, T. Mori, S. Hirata, M. Vacha, *Adv*. *Mater*. **2019**, DOI: 10.1002/adma.201807268.

2. Nanoscale Triplet Exciton Diffusion via Imaging of Upconversion Emission from Single Hybrid Nanoparticles in Molecular Crystals
   K. Narushima, S. Hirata, M. Vacha, *Nanoscale* **2017**, *9*. 10653.

3. Extended Triplet Exciton Diffusion Length in Oriented Conjugated Polymer Nanofibers
   K. Narushima, F. Seino, H. Matsumoto, S. Hirata, M. Vacha, *in preparation*.

Other Publications

1. Plasmon Enhancement of Triplet Exciton Diffusion Revealed by Nanoscale Imaging of Photochemical Fluorescence Upconversion
   Ł. Bujak, **K. Narushima**, D. K. Sharma, S. Hirata, M. Vacha
   , *J. Phys*. *Chem*. *C* **2017**, *121*, 25479.

2. Efficient Triplet-Triplet Annihilation Upconversion in Binary Crystalline Solids Fabricated by Solution Casting and Operated in Air
   K. Kamada, Y. Sakagami, T. Mizokuro, Y. Fujiwara, K. Kobayashi, **K. Narushima**, S. Hirata, M. Vacha, *Mater*. *Horiz*. **2017**, *4*, 83.

3. 1-, 3-, 6-, and 8-Tetrasubstituted Asymmetric Pyrene Derivatives with Electron-Donors and -Acceptors: High Photostability and Regioisomer-Specific

Photophysical Properties
Y. Niko, S. Sasaki, **K. Narushima.** D. K. Sharma, M. Vacha, G. Konishi, *J. Org. Chem.* **2015**, *80*, 10794.

Public appearances

1. 長寿命室温りん光を生じる芳香族有機結晶の三重項励起子拡散
   成島魁至, 平田修造, バッハマーティン. 2018 年光化学討論会, 関西学院大学, 2018 年 9 月

2. [講演奨励賞受賞記念講演] 2 成分から成る分子結晶系アップコンバージョン材料の三重項励起子拡散の可視化
   成島魁至, 平田修造, バッハマーティン. 第 78 回応用物理学会秋季学術講演会, 福島国際会議場, 2017 年 9 月

3. Visualization of Triplet Exciton Diffusion in Crystalline Upconversion Materials
   K. Narushima, S. Hirata, M. Vacha, 81st Prague Meeting on Macromolecules, Prague, September, 2017

4. 単一蛍光分光計測とりん光計測によるポリフルオレンのコンフォメーションの考察
   成島魁至, 平田修造, バッハマーティン.第 66 回高分子学会年次大会, 幕張メッセ, 2017 年 5 月

5. 結晶系アップコンバージョン材料の三重項励起子拡散の可視化
   成島魁至, 平田修造, バッハマーティン. 第 64 回応用物理学会春季学術講演会, パシフィコ横浜, 2017 年 3 月

6. Direct visualization of triplet exciton diffusion in upconversion materials
   成島魁至, 平田修造, バッハマーティン. 2016 年光化学討論会, 東京大学, 2016 年 9 月

7. Nanoscale characterization of photochemical upconversion by single-particle

spectroscopy
<u>成島魁至</u>, 平田修造, バッハマーティン. 2015 年光化学討論会, 大阪市立大学, 2015 年 9 月

Achievements

1. 第 42 回応用物理学会講演奨励賞　受賞

2. 2015 年光化学討論会　最優秀ポスター賞「Journal of Photochemistry and Photobiology A: Chemistry Presentation Prize」　受賞

3. 81st Prague Meeting on Macromolecules, Prague, September, 2017, Poster award

Acknowledgements

I would like to express my deepest thanks to my supervisor Prof. **Martin Vacha** in Tokyo institute of technology for all. I also would like to truly thank Dr. **Shuzo Hirata** in the university of electro-communications for the discussion and good suggestion. Thanks to them, I was able to spend a very fulfilling five years.

I am grateful to Prof. **Takehiko Mori** and **Yasuhiro Kiyota** in Tokyo institute of technology for the helpful advices and quantum chemical calculations.

I am also grateful Dr. **Hidetoshi Matsumoto** and **Fumiyasu Seino** in Tokyo institute of technology for the helpful advices and kind gift of super yellow nanofibers.

I would like to show my appreciation to **Shun Omagari**, **Sharma Dharmendar Kumar**, **Lucaz Bujak**, **Koji Noda**, **Shoki Matsuda**, **Tatsuya Ishii**, **Keisuke Ueda**, **Hiroaki Suzuki**, **Soya Hatazaki**, **Tomonori Nakamura**, **Zhang, Chenan**, **Yasuaki Wakisaka**, **Yuma Goto**, **Tseng Tzu Wei**, **Ryosuke Otsuka**, **Ryotaro Furuya**, **Masahiro Totsuka** and **Quynh Truc Pham** in Tokyo institute of technology for spending good time.

Finally, my deepest thanks to my family **Haruna Narushima**, **Hyota Narushima** and **Yumeri Narushima** for all.